

Design and Demonstration of an Optogenetic Implant using Wireless Power Transfer



Prepared by:
Zaccary Beilinson

Prepared for:
Dr. Sampath Jayalath
Department of Electrical Engineering
University of Cape Town

Submitted to the Department of Electrical Engineering at the University of Cape Town in partial
fulfilment of the academic requirements for a Bachelor of Science degree in Mechatronic
Engineering.

October 30, 2023

Declaration

1. I know that plagiarism is wrong. Plagiarism is to use another's work and pretend that it is one's own.
2. I have used the IEEE convention for citation and referencing. Each contribution to, and quotation in, this report from the work(s) of other people has been attributed, and has been cited and referenced.
3. This report is my own work.
4. I have not allowed, and will not allow, anyone to copy my work with the intention of passing it off as their own work or part thereof.

A handwritten signature in black ink, appearing to read "John Doe".

October 30, 2023

Name Surname

Date

Acknowledgments

The completion of this project signifies the conclusion of a significant chapter in my academic journey. I am immensely grateful for the knowledge that the last four years has imparted, both in terms of academic learning and personal growth. Equally, I'm thankful for the wonderful individuals it has brought into my life, whose invaluable contributions have been instrumental in achieving this milestone.

To my supervisor, Dr. Sampath Jayalath, I want to express my sincere appreciation for granting me the opportunity to work on such an ambitious project and for providing invaluable guidance throughout its duration. Your enthusiasm for the project and your willingness to engage in extensive discussions enriched this experience and turned it into an enlightening learning opportunity.

To Nikhil, Uvir and Ethan, thank you for going out of your way to assist me with aspects of this project that otherwise would not have come to fruition without a helping hand.

To Professor Blumenthal and the Nanotechnology Lab, thank you for coming to my aid in perhaps one of the more adventurous mistakes that I have made.

And to all those in my larger academic journey that have led me to this point, each and every one of you have contributed to the possibility of this milestone.

To my friends I've picked up along the way, Julian, Jahar, Ethan and Ethan (in no particular order). I could not imagine having gone through the last four years without you. While this degree demanded immense sacrifice, it returned so much more in the way of meaningful relationships which were forged in fire. I only wish that we could spend one more traumatic late night together in NEB with some Pizza and a Control exam to study for.

To my extraordinary family, Debi, Barry and Kiara, you guys were the infrastructure upon which this success was built. Mom and Dad, thank you for enabling me to walk this path, for lighting the way when things seemed a little dark and for guiding me back on track when my course strayed. To Kiara, your armchair will remain a place of respite from the work and a place of comforting conversation.

And to my Gran, and the rest of my family that have been rooting for me all the way, we did it.

Abstract

Optogenetics is a field of neuromodulation which enables the activity of targeted neurons to be driven or inhibited by light. The use of **Near-Field Inductive Coupling (NFIC)** to power Optogenetic devices has enabled advancements in the field resulting in the development of **Implantable Medical Devices (IMDs)** capable of carrying out Optogenetic neuromodulation. This project aims to implement a **NFIC** **Wireless Power Transfer (WPT)** protocol capable of powering an Optogenetic implant. This report documents the design and simulation process used to implement the **NFIC** link as well as manufacture an **IMD** of comparable dimensions to the state-of-the-art. Furthermore, the results of a series of testing procedures exhibiting the performance of the **NFIC** link and **IMD** are presented.

The implementation of the wirelessly powered Optogenetic system comprises three main aspects: the design and simulation of the coil link using **Finite Element Analysis (FEA)** software, the design and manufacture of the receiver **Printed Circuit Board (PCB)**, and the design and implementation of the primary circuitry used to drive the **NFIC** link. A physical and simulated two-coil **NFIC** link was implemented, utilising a wire-wound planar transmitter and solenoid receiver coil. An **IMD** of dimensions 6x4mm was manufactured, containing the receiver coil, compensation network, **Impedance Matching (IM)** network, a dual-stage voltage doubler and the **Microscale Inorganic Light Emitting Diode (μ -LED)**. The primary circuitry was designed to operate with a Class E power amplifier at an operating frequency of 13.56MHz. The physical system implemented had a coupling coefficient of 0.014 enabling a **Power Transfer Efficiency (PTE)** of 6.84% which was consistent with the results obtained when simulating the system.

Contents

List of Figures	ix
Abbreviations	xi
1 Introduction	1
1.1 Background	1
1.2 Objectives	2
1.3 System Requirements	2
1.4 Project Scope	2
1.5 Project Limitations	3
1.6 Report Outline	3
2 Literature Review	4
2.1 Neuromodulation in Medicine	4
2.2 The Implementation of Optogenetics	5
2.3 An Overview of Wireless Power Transfer	6
2.3.1 Far-Field Power Transfer	6
2.3.2 Near-field Inductive Coupling Power Transfer	7
2.4 Biomedical Applications of Near-Field Inductive Coupling	8
2.4.1 Two-coil systems	8
2.4.2 Multi-coil Systems	9
2.4.3 Novel Coil Systems and Geometries	11
2.4.4 Methods of Regulating Power Transfer	13
2.5 Contemporary Implantable Devices	13
2.5.1 Form Factors	13
2.5.2 Mechanical Considerations	14
2.5.3 Bio-compatible Surface Coatings	14
2.5.4 Common Circuit Infrastructure	15
2.6 Primary Circuit Considerations	15
2.7 Summary of Implementations and Findings	16
3 Theoretical Background	17
3.1 Near-Field Inductive Coupling	17
3.1.1 Coil Properties and Coupling	18
3.1.2 Resonance	19
3.2 Compensation Networks	20
3.2.1 Compensation Capacitor Configurations	20

3.2.2	Impedance Matching	21
3.3	Power Amplifiers	22
3.4	Inductive Link Equivalent Circuit Theory	23
3.4.1	Link Impedance	24
3.4.2	Load Power	24
3.4.3	Power Transfer Efficiency	24
3.5	Rectification	25
3.6	Magnetic Field Safety	26
3.7	Summary of Theoretical Background	26
4	System Design and Simulation	27
4.1	Design Process	27
4.2	Foundational Characteristics of the System Architecture	28
4.2.1	Wireless Power Transfer Protocol Selection	28
4.2.2	Coil Link Structure	28
4.2.3	System Structure	29
4.3	Near-Field Inductive Coupling Characteristics	29
4.3.1	Inductive Link Constraints	30
4.3.2	Inductive Link Objectives	30
4.4	Near-Field Inductive Coupling Simulated Coil Design	30
4.4.1	Benchmark Design	31
4.4.2	Iterative Design Process	34
4.4.3	Accepted Link Design	35
4.5	Receiver Circuit Design	37
4.5.1	Secondary-side Compensation	37
4.5.2	Rectification Circuitry	38
4.5.3	Impedance Matching	38
4.5.4	Final Receiver Circuit	39
4.5.5	PCB Design	40
4.6	Transmitter Circuit Design	43
4.6.1	Signal Generator	44
4.6.2	Power Amplifier Characterisation	44
4.6.3	Board Requirements	44
4.6.4	Available Hardware Options	45
4.6.5	Power Amplifier Tuning	46
4.6.6	Primary-side Compensation	47
4.7	Summary of System Design and Simulation	48
5	Experiments and Results	49
5.1	Simulation Experimentation	49
5.1.1	Magnetic Field Strength	49
5.1.2	Temperature Variation	50
5.1.3	Specific Absorption Rate	50
5.1.4	Near-Field Inductive Coupling Simulation Results Analysis	51

5.1.5	Near-Field Inductive Coupling Simulation Results Discussion	51
5.2	Physical System Implementation	51
5.2.1	Coil Manufacture	52
5.2.2	Transmitter Assembly	52
5.2.3	Receiver Assembly	52
5.2.4	Test Rig Assembly	53
5.3	Practical Experimentation	53
5.3.1	Near-Field Inductive Coupling Simulation Performance Validation	53
5.3.2	Coupling Experiments	55
5.4	Optogenetic Implant Benchmarking	58
5.4.1	Voltage Doubler Performance	58
5.4.2	Illumination Characteristics	58
5.4.3	Illumination Characteristics Results Discussion	59
5.4.4	Impedance Analysis	59
5.4.5	Impedance Analysis Results	60
5.4.6	Temperature Benchmark	60
5.4.7	Temperature Benchmark Discussion	61
5.5	Wireless Power Transfer Test	61
5.5.1	Full System Experimentation	61
5.5.2	Full System Implementation Discussion	62
5.5.3	Comparison to Similar Implementations	62
6	Conclusions	63
6.1	Report Summary	63
6.2	Conclusion	65
7	Recommendations and Future Work	66
7.0.1	Board Manufacture	66
7.0.2	Test Hardware	66
7.0.3	Receiver Coil Attachment	67
7.0.4	Tissue Environment Design Process and Benchmarking	67
7.0.5	Multi-coil/Novel Geometry Implementation	67
7.0.6	Misalignment Tuning	67
7.0.7	Benchmarking Reflections of Power Electronics Systems	67
7.0.8	Optimisation of Testing Procedures	67
Bibliography		69
A Appendix		76
A.1	ICNIRP Documentation	76
A.2	Benchmark Simulation	77
A.3	Iterative Designs: Additional Simulation Results	78
A.3.1	Design Iteration 1	78
A.3.2	Design Iteration 2	79

A.3.3 Design Iteration 3	80
A.4 Physical System Implementation	81
A.5 Practical Coil Coupling Results	82

List of Figures

2.1	Figure depicting the genetic transfection of light-gated proteins with neurons enabling light-based control of a rodent specimen [1]	5
2.2	Figure depicting structure of Near-Field Inductive Coupling (NFIC) link [2]	8
2.3	Figure depicting the 3-coil system implemented by Mirbozorgi et al. [3]	10
2.4	Data measured by Wu et al. regarding NFIC coupling factors for different coil shapes as a function of Printed Circuit Board (PCB) transmitting coil sizes [4]	11
2.5	Figure depicting receiver shapes analysed by Basir et al. From left to right: circular planar, half-sphere, solenoid and sphere [5]	11
2.6	Figure depicting transmitter system employed in the power chamber implemented by Jow et al. [6]	12
3.1	Diagram depicting NFIC using a two coil system [7]	17
3.2	Diagram depicting the skin effect occurring at high frequencies [2]	19
3.3	Diagram depicting the proximity effect occurring at high frequencies [2]	19
3.4	Figure depicting various single resonant compensation techniques [2]. a.) Series-Series Compensation (S-S) b.) Series-Parallel Compensation (S-P) c.) Parallel-Series Compensation (P-S) d.) Parallel-Parallel Compensation (P-P)	20
3.5	Figure depicting the role of an Impedance Matching (IM) network	22
3.6	Figure depicting the performance of a Class E amplifier under various tuning cases [8]	23
3.7	Diagram depicting Equivalent Circuit of a two-coil NFIC system	23
3.8	Figure depicting the reflected impedance into the primary [2]	24
3.9	Figure depicting a two-stage voltage doubler circuit	25
4.1	Figure depicting a flowchart of the project timeline	28
4.2	Diagram depicting the Optogenetic system architecture	29
4.3	Diagram depicting design process undertaken for the NFIC link	29
4.4	Figure depicting receiver modelled in benchmark simulation	31
4.5	Figure depicting transmitter modelled in benchmark simulation	31
4.6	Benchmark Finite Element Analysis (FEA) Parameters	31
4.7	Figure depicting the results of the lateral and rotational misalignment tests	32
4.8	Figure depicting the results of the Lateral and Rotational Misalignment Tests	33
4.9	Figure depicting the geometry of the double helix receiver	34
4.10	Figure depicting the simulated model for the final design	35
4.11	NFIC FEA Parameters	35
4.12	Figure depicting the results of the lateral misalignment test for the accepted NFIC link	36
4.13	Figure depicting the results of the rotational misalignment test for the accepted NFIC link	36
4.14	Flowchart depicting the receiver circuit structure	37

4.15 Figure depicting equivalent impedance of the voltage doubler and Microscale Inorganic Light Emitting Diode (μ -LED) seen from the receiver coil [9]	38
4.16 Figure depicting the L-type IM network	39
4.17 Figure depicting the receiver circuit	39
4.20 Flowchart depicting the primary-side circuit structure	44
4.21 Figure depicting EPC Class E power amplifiers with required design parameters [8]	45
4.22 Figure depicting EPC9510 Class D power amplifier [10]	46
4.23 Figure depicting Class E Power Amplifier Circuit schematic [8]	47
4.24 Figure depicting EPC9058 design equations [8]	47
5.1 Figure depicting the magnetic field strength generated by the NFIC link	49
5.2 Figure depicting the temperature changes induced by the NFIC link	50
5.4 Figure depicting the PCB with attached receiver coil	53
5.5 Figure depicting the test rig used to benchmark the system performance	53
5.6 Figure depicting the receiver inductance results obtained from the Vector Network Analyser (VNA)	54
5.7 Figure depicting the transmitter inductance results obtained from the VNA	55
5.8 Figure depicting the results of the lateral misalignment tests	57
5.9 Figure depicting the results of the rotational misalignment tests	57
5.10 Figure depicting the board inspection under the MP4522 Ball bonding machine	59
5.11 Figure depicting the Implantable Medical Device (IMD) temperature variance	60
5.12 Figure depicting voltage waveform measured at the receiver of the IMD	61
A.1 Figure depicting International Commission on Non-Ionizing Radiation Protection (IC-NIRP) magnetic field strength regulations	76
A.2 Figure depicting ICNIRP Specific Absorption Rate (SAR) regulations	76
A.3 Figure depicting the commercial Radio Frequency Identification (RFID) transmitter used in [11]	77
A.4 Figure depicting the comparative RFID transmitter modelled in simulation	77
A.5 Figure depicting the simulated magnetic field vectors for the 3mm benchmarking setup .	77
A.6 Figure depicting an isometric view of the simulated setup with a wire-wound transmitter	78
A.7 Results obtained during the rotational misalignment sweep with a wire-wound transmitter	78
A.8 Results obtained during the lateral misalignment test with a wire-wound transmitter .	78
A.9 Figure depicting simulated setup for the double helix coil	79
A.10 Figure depicting a side view of the double helix coil	79
A.11 Figure depicting the response of the double helix setup to parallel misalignments . .	79
A.12 Figure depicting the response of the double helix setup to rotational misalignments .	79
A.13 Figure depicting an isometric view of the 15-turn solenoid setup	80
A.14 Figure depicting the results of the 15-turn lateral misalignment sweep	80
A.15 Figure depicting the results of the 15-turn rotational misalignment sweep	80
A.18 Figure depicting the simulated receiver coil inductance vs frequency	82

Abbreviations

μ -LED Microscale Inorganic Light Emitting Diode

AC Alternating Current

CHR-2 Channelrhodopsin-2

DBS Deep Brain Stimulation

DC Direct Current

EMF Electromotive Force

FEA Finite Element Analysis

HFSS High Frequency Simulation Software

ICNIRP International Commission on Non-Ionizing Radiation Protection

IM Impedance Matching

IMD Implantable Medical Device

NFIC Near-Field Inductive Coupling

P-P Parallel-Parallel Compensation

P-S Parallel-Series Compensation

PCB Printed Circuit Board

PSC Printed Spiral Coil

PTE Power Transfer Efficiency

RF Radio Frequency

RFID Radio Frequency Identification

SAR Specific Absorption Rate

SMD Surface Mount Devices

S-P Series-Parallel Compensation

S-S Series-Series Compensation

VNA Vector Network Analyser

WPT Wireless Power Transfer

ZVS Zero Voltage Switching

Chapter 1

Introduction

Any man could, if he were so inclined, be the sculptor of his own brain.

—*Santiago Ramon y Cajal*

1.1 Background

The study of neural networks provides an understanding as to how all behaviours of living things transpire [12]. A fundamental question arises within this field of study dealing with whether the behaviour of these neural networks can be monitored and modified to investigate and address different disorders of the brain.

This question opens an expansive field of treatment known as ‘neuromodulation’. As the name describes, neuromodulation is the technique of altering neuronal activity. This is achieved through employing a stimulant directly to a target area in the brain to either inhibit or excite the action of these neurons. In conventional medical applications these stimulants are provided pharmaceutically, though recent developments in engineering allow for miniaturised [IMDs](#)¹ to stimulate neuronal activity. Whilst an array of stimulation methods exist, Optogenetic neuromodulation forms the basis of this report.

Optogenetics enables the activity of targeted neurons to be driven or inhibited by light [13]. This is achieved through the genetic modification of these targeted neurons such that they express a family of proteins which behave as light-gated ion channels. In illuminating these proteins, the action potentials² of neurons can be controlled. Early implementations of Optogenetics focally delivered light to these targeted neurons via a tethered laser-diode optical fibre [14]. This process has since evolved to incorporate the use of [Wireless Power Transfer \(WPT\)](#) technology to power these [IMDs](#).

The use of [NFIC](#) facilitates the implantation of a μ -LED to direct light to targeted regions of the brain. The ability to power these devices internally has eliminated certain bio-compatibility and functional constraints of previous implementations, such as system tethers or bulky battery systems. This advancement has played a crucial role in achieving the compact dimensions characteristic of contemporary implant designs.

The design of an Optogenetic system entails the culmination of fields pertaining to electromagnetism, power electronics and bio-materials engineering and thus represents a rich field of applications.

¹In the context of this report, IMDs refer to implantable neural control prosthetics.

²Also known as nerve impulses, these are a sequence of voltage changes occurring across a membrane in the brain responsible for information transmission.

1.2 Objectives

The overarching objective of this project is the successful implementation of an Optogenetic [IMD](#) with miniaturised geometry comparable to that of contemporary architectures. This implant must be powered via [NFIC](#) and must provide sufficient output power to theoretically excite neurons via illumination in a safe manner. The following list outlines the main objectives of this project:

1. To design an Optogenetic [IMD](#).
2. To simulate and practically implement a functioning [NFIC](#) system.
3. To employ efficient power electronics to support the [NFIC](#) system.
4. To holistically combine these modules to create a wirelessly powered Optogenetic [IMD](#).

1.3 System Requirements

In ensuring the accomplishment of the objectives defined above, the following system requirements are defined:

1. A theoretically implantable device of dimensions comparable to contemporary architectures is manufactured.
2. Power is transferred to this device over a distance of 10mm using [NFIC](#).
3. The system employs efficient power electronics to ensure optimal power transfer.

1.4 Project Scope

The following project outlines the research and development of a wirelessly powered Optogenetic implant. The scope of the project, therefore, includes the following:

- A review outlining relevant literature pertaining to similar applications and qualities of interest of these applications.
- An overarching explanation of the theory pertaining to [WPT](#) and power electronics which was used to inform design decisions.
- The design and implementation of a simulated [NFIC](#) power transfer link.
- The design and implementation of power electronics in primary and secondary circuits to support this link.
- The selection and implementation of suitable circuitry to drive the Optogenetic receiver.
- The physical manufacture of the full system used to perform Optogenetic neuromodulation.
- Test benchmarks that outline the performance of each module of the overarching wirelessly powered Optogenetic system.

1.5 Project Limitations

A significant limitation in any field that pushes the boundaries of contemporary hardware is the availability of both the necessary technology for hardware manufacture and testing as well as the financial resources to bring designs to fruition. These constraints are particularly relevant to this project, where operating at high frequencies with miniaturised, sensitive circuitry demands specialised equipment.

Given the limited budget of R2000, achieving a high frequency inductive link is a notable accomplishment, considering the expenses associated with the required power electronics. When factoring in the costs of specialized manufacturing techniques needed to produce a [PCB](#) of the desired dimensions, the challenge seems nearly insurmountable. Considering these factors, the implemented system had to adhere to slightly enlarged dimensions and abandoned certain bio-compatibility standards, functioning as a working prototype. The 13 week project timeline served to impact final benchmarking through manifesting as initial oversights in project design which were prompted by the need for rapid development due to tight timelines. Whilst these oversights became clear following the ordered production of the [PCB](#) and are consequently discussed in this project report, their impact remains in testing as no changes could be made to the board once manufactured due to its scale.

The ability to benchmark and debug the final system was a considerable limitation that requires extensive forethought given the scale of the hardware. Conventional means of measuring voltages, currents and properties of [WPT](#) using standard tools was immensely challenging given the inability to physically interface with the small hardware using large probes. This was made more challenging given the inability to work with the hardware at hands reach due to safety concerns regarding device operation at megahertz frequencies. Moreover, the necessary tools to implement testing procedures at megahertz frequencies were, for the most part, unavailable at the University of Cape Town, or only unveiled themselves at the last moment. The tolerances of testing equipment were again incredibly influential in skewing data in the testing procedures given the nature of the small values that were being worked with. Thus, the testing process, in itself, was an immensely complex task.

Finally, the tolerances involved in any form of manufacture, be it [PCB](#) manufacture or coil manufacture, became evident in the testing process.

1.6 Report Outline

The report commences in chapter [2](#) with a review of relevant literature pertaining to previous implementations of Optogenetic devices and [NFIC](#) in the field, outlining characteristics of interest that serve to guide the development of this project. Following this, in chapter [3](#), an insight is given into the theory of power electronics and [NFIC](#) used to govern the design decisions made over the course of the project's development. These design choices are covered in chapter [4](#), which outlines the full design and implementation process of the wirelessly powered Optogenetic system. Chapter [5](#) outlines the test procedures used to benchmark the system alongside an analysis and discussion of results obtained during testing. Finally, chapter [6](#) provides a summary of the report and the conclusions drawn from the experimental test procedures, followed by recommendations of how the project may be carried forward in the future in chapter [7](#).

Chapter 2

Literature Review

Wisdom is not a product of schooling but of the lifelong attempt to acquire it.

—Albert Einstein

The following chapter presents an overarching background pertaining to the field of [WPT](#) with specific applications in Optogenetic neuromodulation. With this in mind, its purpose is to offer the reader a thorough understanding of the existing literature on the intersection of [WPT](#) and Optogenetic [IMDs](#), thus contextualising the development of this project.

The structure of the literature review commences with an exploration of the concept of neuromodulation and the introduction of [IMDs](#). This is followed by an examination of the pertinent literature outlining the field of Optogenetics, thus contextualising the application and prerequisites of the [IMD](#) developed within the scope of this project. Subsequently, a focal point is placed on the introduction of [WPT](#) to [IMDs](#). This section provides an overview of the most prevalent [WPT](#) types found in the literature. The spotlight then shifts to the applications of [NFIC](#) in related works wherein various link characteristics in existence are highlighted and discussed. Following this is a discussion of the hardware attributes employed in the literature to attain state-of-the-art [IMDs](#) along with a mention of considerations for the primary circuit. The chapter concludes with a comprehensive summary of the relevant findings in the literature published to date.

2.1 Neuromodulation in Medicine

The nervous system controls body processes through densely interconnected neural networks. The activity patterns within these neural networks govern all behaviours exhibited by living organisms. Consequently, the ability to modify these biological processes by directly interfacing with neurons enables the treatment of a range of neurological, neuropsychiatric, and neuromuscular disorders [\[12, 15, 16\]](#). Neuromodulation involves altering neuronal activity by applying a stimulus directly to a target area in the brain. Within the field of medicine, this stimulus typically takes the form of pharmaceutical agents. Conversely, within the field of Biomedical Engineering, these agents may arise in the form of electroceutical devices¹ [\[17\]](#). Various methods are currently employed to modulate or stimulate certain neuronal behaviours. Beyond the use of conventional pharmacological stimuli exists methods of electrical, thermal and optical stimulation. This paper focuses on the neuromodulation technique known as Optogenetics, which has its foundations in optical stimulation.

¹Implantable devices which deliver neural impulses to specific anatomical targets.

2.2 The Implementation of Optogenetics

During the early 2000s, research in the field of neuromodulation saw the emergence of techniques beyond traditional electrical stimulation. Optogenetics rose to prominence in research, largely attributed to the work of Edward S. Boyden and Karl Deisseroth. Boyden defined Optogenetics as ‘the set of genetically encoded molecules that, when targeted to specific neurons in the brain, enable their activity to be driven or silenced by light [13].’ In 2003, the discovery of an opsin² known as **Channelrhodopsin-2 (CHR-2)** marked the beginning of using implanted optical fibers in the brain for precise neural control. The years 2004 to 2006 witnessed Deisseroth’s transition from *in vitro*³ microbial opsin expression experiments towards fiber-optic neural interfaces allowing for behavioural control in mammals, particularly rodents at the time [14].

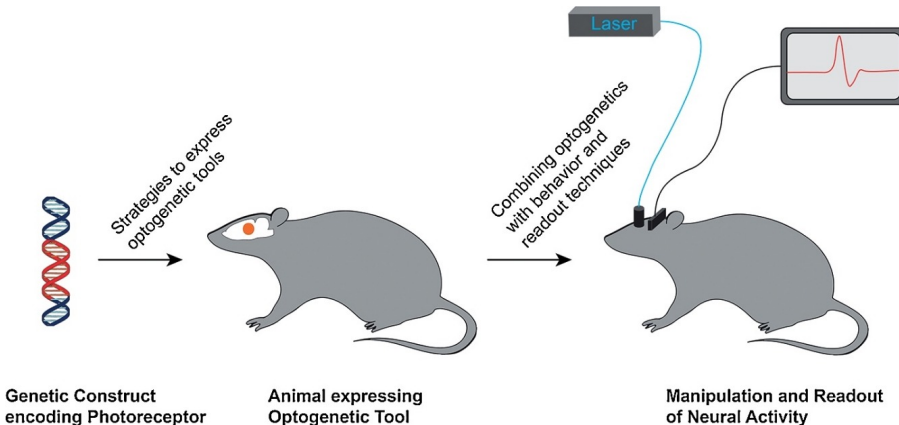


Figure 2.1: Figure depicting the genetic transfection of light-gated proteins with neurons enabling light-based control of a rodent specimen [1]

The surge of Optogenetics was propelled by the ability to offer more selective targeting of neurons than other neurostimulation methods of the time. As depicted in Figure 2.1, the process necessitates three fundamental criteria: the culturing of photosensitive ion channels or proteins, accurate targeting of these ion channels/proteins to neurons, and the capability to deliver strong and precisely timed light to the intended brain regions. While this report primarily focuses on the final criterion, a brief discussion of the initial two criteria follows to provide a contextual understanding for the functioning and requirements of Optogenetic **IMDs**.

In the context of Optogenetic neuromodulation, achieving control over neurons necessitates the culturing and genetic transfection⁴ of specific photosensitive proteins, known as microbial opsins. These opsins are capable of directly converting photons into electrical current. As noted in current applications, one of the primary microbial opsins utilized is **CHR-2** [18]. Although **CHR-2** is widespread within the literature, it’s important to note the existence of various opsin variants within this family. Optogenetics commonly employs three branches of this opsin family: bacteriorhodopsins, halorhodopsins, and channelrhodopsins [14].

To exert behavioral control over genetically modified neurons, a safe and precise method is required to deliver visible light deep into the brain at an intensity of 100mWmm^{-2} [14]. Within much of the

²A naturally occurring protein which functions as a ‘light-driven ion pump’ [13].

³Experimentation which occurs in petri dishes or test tubes.

⁴Artificial introduction into cells.

literature, light is introduced into the targeted cells using laser-diode optical fibers coupled to external light sources with varying wavelengths based on the opsin used [19, 20, 21]. For example, Aravanis et al. discuss the implementation of laser-based optical implants by coupling the implant with a waveguiding optical fiber [22]. To understand the underlying causal relationship behind neural activity and resulting behaviour, a neural probe able to measure light-excited electrical signals was combined with an optical implant in [23, 24]. A more complex technique was introduced by Zorzos et al. wherein an array of multi-waveguide probes aligned in a parallel manner was used to implement independent light delivery 3-dimensionally throughout the brain [25]. Kwon et al. designed head-mountable Optogenetic implants using a tethered apparatus to provide μ -LEDs driving power [26]. However, these approaches create an internal tether to external light sources, presenting several limitations. A laser system with considerable weight and a large form factor cannot be directly inserted into brain tissues and, furthermore, an additional tool for the delivery of focal light is required for localised stimulation.

These limitations have spurred the development of fully implantable IMDs, enabling the implantation of highly efficient μ -LEDs for light targeting [27]. In numerous applications, these μ -LEDs have been powered by internal battery systems. However, using batteries in this implementation introduces additional drawbacks due to the large form factors and heavy weight which causes susceptibility to brain damage and, furthermore, the need for battery replacements leading to additional surgeries [28]. The evolution of these IMDs has given rise to a variety of hardware characteristics which are necessary to ensure suitable device implantation.

2.3 An Overview of Wireless Power Transfer

One of the key issues identified within early literature is the strain and micromotions which results from the IMD being tethered to an external stimulation hub which causes damage in surrounding neural tissue and the blood brain barrier [3, 29]. While the incorporation of implantable battery systems has been examined in the literature [30], their limitations as noted in section 2.2 have prompted a shift in the field of IMDs towards the adoption of WPT.

Depending on the method of power harvesting, WPT systems can be categorized into Far-Field or Near-Field protocols. Given the specific focus of this project on Near-Field approaches, a concise review of literature regarding applications of Far-Field power transfer will be presented, aiming to briefly characterise the strengths and limitations of Far-Field power transfer in biomedical applications. Following this, Near-Field power transfer and its important overarching developmental trends in the field will be provided. This will serve as a segue into specific applications of Near-Field implementations in related biomedical works.

2.3.1 Far-Field Power Transfer

Far-Field WPT is implemented using Radio Frequency (RF) signals, covering a wide frequency range from $420MHz$ to $2.4GHz$, and characterized by wavelengths spanning $0.1m$ to $1m$ [29]. This technology enables power delivery across significant distances, extending over several meters and enabling antennas to be positioned freely within experimental environments due to its radiative nature. The applications of Far-Field are thus well suited to situations requiring deep implants without precise alignment for power transfer, though energy loss caused by human tissue is of concern from excessive microwave

radiation [31]. Recent advancements in Far-Field applications for **IMDs** have their primary focus on specialized antenna structures with attributes like stretchable electronics, flexible substrates, and intelligent architectural designs [32, 33, 34, 31].

Biomedical Implementations of Far-Field Power Transfer

As an example, in 2015, Park et al. introduced a system that harnessed a flexible antenna-based Far-Field power transfer protocol. This system operated at a frequency of 2.34GHz , accommodating a $3\times 3\text{mm}$ wide bandwidth antenna. The setup incorporated four transmit antennas configured to deliver 2W of **RF** power to the implanted antenna at distances of up to 20cm . The system further demonstrated robust tolerance to variations in location and rotational misalignments due to its inherent radiative nature [32].

McCall et al. re-affirm the advantage of employing Far-Field applications as stemming from the radiative nature of this power transfer [33]. In their study, the Far-Field protocol implemented facilitated power transfer over distances of up to 2m , making it suitable for multiple $\mu\text{-LED}$ devices. The system developed operated at 915MHz , with the receiver featuring a dual **PCB** setup incorporating a ceramic antenna and supporting **IM** and rectification circuitry. On the transmitter side, a Class AB power amplifier, RF signal generator, and antenna provide a power output of around 1W [33].

In 2023, Sharma et al. published a paper discussing the implementation of a transmitter antenna array which provided power to a rectenna (rectifier and antenna) for powering a pacemaker capsule [31]. The implantable antenna was printed on Rogers **PCB** substrate and operated in dual-bands of 915MHz and 2.45GHz enabling power transfer over a distance of 15cm . An inherent limitation in existing **WPT** methods for **IMDs** lies in the provision of illumination at a single, specific brain region using a single optical wavelength constrained by a sole **RF**. To address this issue, Park et al. introduced a novel approach by implementing a multichannel stretchable antenna system. This system facilitated the use of multiple well-separated operating frequencies for various light sources within a single platform, capable of delivering up to 1W of power. The system offered frequency-selective control at 2.3GHz and 2.7GHz [35].

Optogenetics applications demand low-power transmission over short distances, as well as low power density. Importantly, the transmission characteristics of Far-Field power transfer, concerning distances and the scale of the hardware used, extend beyond the applications of Optogenetics. Far-Field applications are generally found in deep body implants given their available power transfer distances [36]. In the context of close-range power transmission, radiative methods are both redundant and find less preference in the literature due to their lower operational efficiency. This operational efficiency generally falls below 1% [5]. Furthermore, Far-Field power transfer often exceeds the regulated **SAR** limits, as noted in [37].

2.3.2 Near-field Inductive Coupling Power Transfer

Given the extensive application of **NFIC** in the literature, the following section serves to provide a brief contextual of **NFIC** prior to engaging with a detailed discussion of its applications in Biomedics in section 2.4.

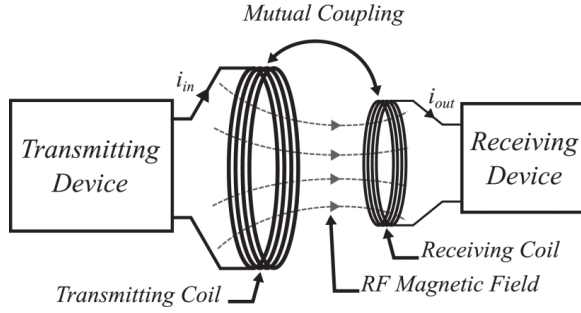


Figure 2.2: Figure depicting structure of [NFIC](#) link [2]

As explained by Schormans et al. [NFIC](#) involves the alignment of two inductive coils in close proximity, establishing a magnetic coupling [2]. [NFIC](#) systems typically achieve loose coupling coefficients⁵, operating over distances smaller than their coil diameters [29]. The primary figure of merit in [NFIC](#) systems encompasses a high [Power Transfer Efficiency \(PTE\)](#), which requires the facilitation of robust power transfer networks achieving minimal variances in coupling at various distance and misalignment conditions.

The [PTE](#) of the link serves as a crucial indicator for evaluating [NFIC](#) systems as it quantifies power losses in both transmitter and receiver circuits as well as the absorbed electromagnetic energy in surrounding tissue which may lead to localized temperature rises and tissue damage [38]. Low frequency applications tend to reduce the effect of tissue absorption, enabling greater transfer distances albeit with larger coil geometric requirements. A frequency of 13.56MHz generally poses an attractive operating frequency selection given its acceptable level of tissue absorption and its alignment with Near-Field communication standards [29]. Efficient power transfer can be attained with high quality factor coils, though attaining high power efficiency in most applications proves to be a complex task due to geometric constraints within Biomedical use cases. Therefore, a great deal of literature has focused on optimizing [NFIC](#).

2.4 Biomedical Applications of Near-Field Inductive Coupling

Although [NFIC](#) is a prevalent architecture in the field of [IMDs](#), no universally agreed-upon design for these systems exists. A vast collection of literature details various techniques which aim to increase the system's [PTE](#). As noted, in a typical [NFIC](#) system, two closely coupled coils form the core, although some variations employ multi-coil configurations, as evidenced in studies such as [39, 40, 41, 3]. Extensive research has delved into the critical features of these networks, encompassing coil types, biocompatibility, geometric aspects, and misalignment properties [41]. This section serves to characterise the findings from these studies.

2.4.1 Two-coil systems

Whilst the implementation of two-coil [NFIC](#) links form the foundation of many basic systems, there have been many variants thereof which have interesting characteristics. A major consideration in two coil systems is the comparative performance of planar and 3-dimensional coils. In 2009, Jow et al. commented on the advantage of [Printed Spiral Coils \(PSCs\)](#) being that they offer more flexibility

⁵Loose coupling refers to coupling coefficients less than 0.5.

in design and have the potential to conform to body curvature when fabricated on flexible **PCB** substrates [42]. In a paper published in 2007, Jow et al. provide a comprehensive design process for planar transmitter and receiver coils achieving efficiencies of 41.2% and 85.8% at $1MHz$ and $5MHz$ accordingly in an air environment [43]. Comparatively, in 2017, Delhaye et al. reported the use of a 3-dimensional wire-wound solenoid with a ferrite core coupled with a planar transmitter operating at $1MHz$ on a sheet of ferrite. The system achieved a coupling of 0.03 at a distance of $10mm$ with ferrite and 0.01 without ferrite, enabling **PTEs** of around 20% [44].

The implementation by Delhaye et al. raises concerns regarding the tissue environment. Evidently the use of ferrite is non-compatible with implantation in the body. It is further evident that the environment does not merely influence the core of the receiver transmitter. In 2009, Jow et al. noted that the design implemented in their paper in 2007 did not include the effects of a surrounding tissue environment. Taking the tissue environment into consideration is an important factor on link performance as it affects the parasitic components of the coils as well as coil coupling. This variance in coupling arises due to increased tissue absorption from a change in dielectric properties as depicted in Table 2.1 [43]. As noted by Jow et al. modelling of the tissue concerns the dielectric losses, $\tan(\delta)$, which is related to the conductivity, $\sigma = \epsilon_0 \epsilon_r \omega \tan(\delta)$.

Table 2.1: Table depicting material dielectric properties [43]

Material	Air	Saline	Muscle	FR4	Silicone
Frequency (MHz)	13.56	13.56	13.56	13.56	13.56
$\sigma (S/m)$	0	0.60	0.58	$1.344e^{-4}$	$2.26e^{-6}$
ϵ_r	1	78	136	4.4	3.0
$\tan(\delta)$	0	10.2	6.0	0.04	0.001

In a 2017 paper, Waters et al. emphasized that two crucial factors influencing high **PTE** are coil coupling and the quality factor of each coil [45]. The impact of different tissue environments on these factors was addressed by Jow et al., who noted that the quality factor of each coil decreases in environments with higher permittivity and conductivity, such as saline and muscle, leading to increased losses. Table 2.1 provides an overview of the dielectric properties of various environments, affecting permittivity. It is generally observed that changes in the environment result in a significant reduction in **PTE**. Waters et al. further emphasized that high quality factors do not necessarily guarantee high coupling, especially when the coil geometry is asymmetric [45]. Their study illustrated that, for a flat spiral coil, the optimal ratio of the inner diameter to the outer diameter of the coil is 0.4. Moreover, in 2010, Kiani et al. presented a two-coil, planar air-core system capable of delivering $11.2mW$ of power to the load over a distance of $0.5cm$ to $2cm$ with a variance in the required transmitter power of $78mW$ to $1.1W$, indicating the effect of coil separation in reducing **PTE** [46].

2.4.2 Multi-coil Systems

In considering the work done by Kiani et al. it is evident that coupling coefficients exhibit an inverse relationship with the distance between transmitting and receiving coils. To address the challenges posed by changes in gap distance and horizontal misalignments between primary and secondary coils,

one effective solution involves integrating additional coils into either the primary or secondary side [39, 5, 47]. This approach further helps reduce the impact of misalignment issues [48].

For example, in 2017, Mirbozorgi et al. introduced a system that enables inductive power transfer to multiple small implants placed with arbitrary misalignments at a distance of $8mm$ from the transmitter coil, distributed across a large area of the brain [3]. This highlights the need for robust misalignment tolerance. They observed that two-coil inductive links often suffer from weak coupling when the distance exceeds the diameter of the receiver coil. To address this, Mirbozorgi et al. introduced an additional resonator with a high quality factor at the receiver plane as depicted in Figure 2.3. This served to enhance the magnetic field coverage area and significantly extended the range of the transmitter coil. Their system consisted of a one-turn planar transmitter coil and resonator, paired with a four-turn 38AWG pancake-wound receiver coil. The coupling achieved between the transmitter coil and resonator was 0.132, while the coupling between the transmitter coil and receiver coil was 0.002. This system delivered $1.3mW$ of power to the load with an efficiency of 2.4% using a $60MHz$ carrier frequency. In 2022, Basir et al. reported the implementation of a three-coil system [5]. Like Mirbozorgi et al., they observed that the inclusion of an additional driver coil resulted in an improved PTE. This enhancement arose out of the increased quality factor and the strengthening of the mutual coupling caused by the additional driver coil.

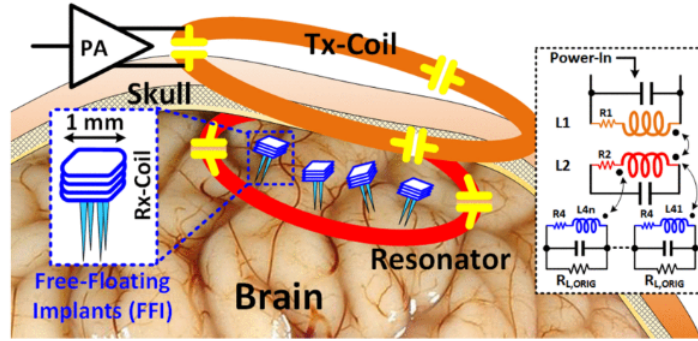


Figure 2.3: Figure depicting the 3-coil system implemented by Mirbozorgi et al. [3]

In a similar vein, Mirbozorgi et al. introduced a system in 2014 designed to power multiple receivers for facilitating WPT in research involving freely moving animals [49]. They employed a parallel multi-coil array structure, primarily based on a four-coil inductive link. The system achieved a PTE of 16% and delivered $28mW$ of power to the load, maintaining a variation in power delivery below 14% at an operating frequency of $13.56MHz$. Multi-coil systems are often used to counteract variances arising from the loading effect. In 2015, Chang et al. showcased a three-coil configuration for this specific purpose. They compared a two-coil system, which achieved a PTE of 12%, to the three-coil system which significantly outperformed it with a PTE of 22% [40]. This marked an 83% increase in efficiency. Xu et al. corroborate the findings presented by Chang et al., noting that two-coil systems experience a substantial reduction in PTE as the distance between the coils increases [47]. While the overall configuration of the NFIC system has a profound impact on its performance, it is equally vital to take into account how the inherent design of the transmitter and receiver coils affect the PTE of the link. Numerous research publications have delved into novel coil shapes with the aim of enhancing system performance.

2.4.3 Novel Coil Systems and Geometries

The specific implementation of coil geometry has a significant impact on the system performance. This pertains to the size of coils and the various coil shapes implemented. Simple comparisons have been conducted regarding planar shapes like circles and rectangles, further considering the impact of the combination of the two. Wu et al. noted in 2014, in comparing the performance of circular and rectangular coils, the combination of circular transmitters to rectangular receivers for **PCB** planar coils perform the best in terms of coupling [4].

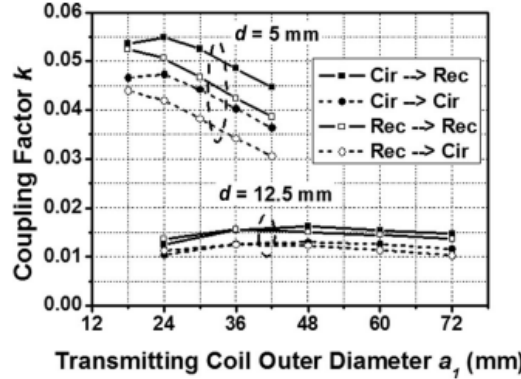


Figure 2.4: Data measured by Wu et al. regarding **NFIC** coupling factors for different coil shapes as a function of **PCB** transmitting coil sizes [4]

In 2017, Yang et al. demonstrated a system wherein the receiver comprised a novel two-layer FR4 **PCB** design to increase efficiency. This receiver coil system had an inner dual-layer **PSC** and an outer layer Helical coil [39]. The implant coil was implanted on both rigid and flexible substrates. The efficiencies achieved through air for either substrate were 19.1% and 14.8% and through tissue they were 11.7% and 7.7%.

In 2022, Basir et al. introduced an innovative sphere-shaped receiver coil designed to increase the robustness of **WPT** systems to misalignments and extend charging coverage [5]. Previous strategies implemented included using Helmholtz body transmitter coils [50], crossed-loop 3-D transmitter and receiver coils [51, 52], and half-sphere-shaped coils [53]. Within these papers it is noted that Helmholtz body coils provide a uniform field distribution but are large and not easily portable. Furthermore, crossed-loop 3-D transmitter coils are designed to address angular misalignments but add bulk and weight to the system, making them impractical for mobile patients. Orthogonally connected multi-coil setups also mitigate angular misalignments but contribute to the weight of the implant, affecting wearability. In contrast, the sphere-shaped coil introduced by Basir et al. offers a more lightweight, simple, and portable solution.



Figure 2.5: Figure depicting receiver shapes analysed by Basir et al. From left to right: circular planar, half-sphere, solenoid and sphere [5]

The performance of the sphere-shaped coil was compared with that of circular planar, half-sphere, and standard solenoid coils. The PTE of these various receiver coil shapes were analyzed under different lateral and angular misalignments, through both simulations and experimental measurements. Under nominal conditions, the receiver efficiencies achieved were 7.68%, 10.18%, 25.01%, and 22.38%. However, during a 90° misalignment these efficiencies dropped to 0%, 0.2%, 0.15%, and 5.4% [5]. Xu et al. also introduced a unique receiver coil design involving two planar sub-coils positioned on either side of a helical sub-coil, forming a closed cylinder configuration [47].

Notably, efforts to enhance system performance extend beyond innovative receiver geometries and encompass diverse transmitter architectures as well. In 2014, Mirbozorgi et al. introduced a transmitter architecture designed to power multiple receivers, particularly in the context of WPT for freely moving animal research. This approach was founded on a parallel multi-coil array structure. Their transmitter system comprised a chamber that utilizes a resonance-based multi-coil array structure, enabling uniform power transmission in three dimensions. They achieved a PTE of 16% and delivered 28mW of power to the load. The system was able to limit the maximum variation in power delivered to the load to 14% at an operating frequency of 13.56MHz [49]. Furthermore, the system achieved natural power localization without the need for intricate circuitry to pinpoint receiver locations.

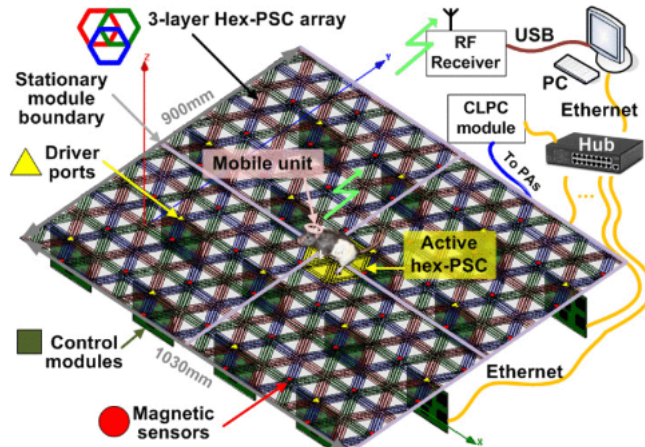


Figure 2.6: Figure depicting transmitter system employed in the power chamber implemented by Jow et al. [6]

The use of power chambers, while not entirely commonplace, finds references in other systems wherein a single large coil or multiple smaller coils form the transmitter chamber as seen in the work of Jow et al. in 2014 [6]. This system, was more complex than the one implemented by Mirbozorgi et al. in 2014, and incorporated three-axis magnetic sensors to be able to focus WPT on a target. Furthermore, they identified that chambers tiled with smaller coils tend to be more efficient in providing a homogeneous magnetic flux density across the entire chamber.

Similarly, in 2013, Xu et al. presented a mat-based transmitter design for powering mobile receiver targets. This system adopts a four-coil configuration, consisting of a driver-coil array, a hexagonally packed transmitter mat, a secondary receiver coil, and a load coil. This design generated a flat magnetic distribution over a defined area, ensuring consistent power output regardless of the receiver coil's location [47]. The system utilised coupled resonance between two coils in the transmitter section. The first coil served as the driver, which excited the transmitter mat. On the receiver side, there was a

secondary coil functioning as the receiving resonator, closely connected to the load coil. The driver coil and transmitter mat together act as a voltage step-up transformer, creating stronger resonance to increase **PTE** to the secondary.

2.4.4 Methods of Regulating Power Transfer

The implementation of certain techniques to ensure closed-loop control of the activity of **IMDs** has served to optimise the behaviour of devices to variations in operating conditions. The impact of misalignment conditions, variations in coil spacing, and fluctuations in load conditions can lead to a decrease in the system's **PTE**. Numerous research publications explore strategies for mitigating these issues. These methods include closed-loop back-telemetry, resonant load transformation and frequency tuning amongst other things. These systems are generally complex and thus fall outside the scope of this project, though this section serves to offer some insight into more advanced techniques that exist within the literature.

As an example, in 2013, Xue et al. published a paper discussing optimal resonant load transformation as a means to improve **PTE** [28]. In this paper it is noted that the addition of a compensation capacitor to form a resonant circuit contributes to greater transfer efficiencies, though this is limited due to loading effects. The introduction of load transformation serves to mitigate these loading effects. Moreover, in 2008, Si et al. presented a method to regulate the **PTE** of a link by adjusting the resonant operating frequency of the primary during variations in load and coupling. The operating frequency is varied through altering the effective tuning capacitance through soft-switched phase control [54]. This system retains low switching losses and smooth frequency variations. The soft-switched system achieved a **PTE** of 80% when transferring 15W over a 10mm air gap.

In 2010, the two-coil system implemented by Kiani et al. made use of an off the shelf **RFID** reader operating at 13.56MHz to drive the transmitter coil. In this paper, the back telemetry capability of the commercial **RFID** circuit is stated to be beneficial as it enables stabilisation of received voltage on the implant. These load voltage variations would otherwise occur as a result of changes in the load which occur during stimulation or misalignments [46].

2.5 Contemporary Implantable Devices

In the last two decades, there have been significant advancements regarding the biological compatibility of **IMDs**. Engineering development enabling the manufacture of soft, flexible and multifunctional devices has progressed. These progressions are fueled by factors including the movement towards smaller dimensions and the manufacture of implants using bio-compatible materials that further flexible mechanical properties. Emphasis on these aspects stems from their role in determining the level of invasiveness, functional performance and potential for long-term use within the body. This section serves to characterise the state-of-the-art **IMDs**.

2.5.1 Form Factors

Given the nature of Optogenetic **IMDs** being implanted in the head, the allowable form factor is highly constrained, typically limited to around 5x5mm. Given the fact that these devices are implanted

between the skull and scalp or inside the skull, the distances that power needs to be transferred is in the range of at least 5mm to 12mm [4]. Table 2.2 summarises some of the dimensions of **IMDs** found in the literature.

Table 2.2: Figure depicting **IMD** dimensions found in the relevant literature

Source	[39]	[28]	[37]	[42]	[40]	[55]	[11]
Dimensions (mm)	5x5	25x10	6x11	10x10	5x5	3x2	3.5x1

2.5.2 Mechanical Considerations

Won et al. consider the significance of material properties in the design of these devices, highlighting that high stiffness can lead to considerable insertion-related lesions and heightened inflammation responses due to relative motion between biotic and abiotic materials [29]. As a result, flexible substrates for **PCBs**, known for their soft mechanical compliance and minimal disruptive integration, are preferred over rigid FR4 substrates [49, 56]. Considering this, Yang et al. reported the use of both FR4 substrates and flexible **PCBs** made from R03010 Rogers FPC in their **IMDs** for **Deep Brain Stimulation (DBS)** treatment of Parkinsons disorder [39]. Moreover, the integration of soft materials, such as flexible electronics utilizing components like flexible wiring made of carbon nanotubes, Polydimethylsiloxane, graphene films and single-walled carbon nanotubes have been reported in found use in the literature [57, 58, 59, 60]. In addition to this, other printed elastic and stretchable conductors with structures like buckled nanoribbons and serpentine nanowires, has been reported. In a paper published by Park et al. a low modulus, flexible **IMD** is reported using serpentine electrical interconnects and encapsulated by silicone to accommodate anatomical shapes and natural motions [32].

2.5.3 Bio-compatible Surface Coatings

In addition to the considerations to minimise invasive implantation, considerations need to be made to ensure functionality throughout chronic implantation. Consequently, **IMDs** necessitate protective measures to isolate them from biofluids that can harm their electrical characteristics. This is supported by a paper published by Hassler et al. wherein it is noted that discrepancies in mechanical properties can trigger cellular reactions resulting in encapsulation of the implant, thereby impairing electrical performance [61]. Additionally, surface properties that are not bio-compatible may provoke undesired foreign body reactions. Hence, surface coatings are often applied to the device hardware to enhance bio-compatibility. For instance, Montgomery et al. utilized Acrylic encapsulation to electrically insulate the hardware and offer resistance against biological degradation [55].

Shin et al. demonstrated the functional operation of devices coated in Parylene after 90 days of immersion in physiological saline solution at 60°C [62]. This supports the practice used by Montgomery et al. through indicating a potential year-long expected device lifetime at 37°C due to the device's encapsulation. Hassler et al. suggests that the use of bio-compatible polymers for neural implants is optimal due to their ability to elicit minimal to no response upon implantation, ensuring long-term stability in hostile environments, maintaining low material stiffness, and providing effective electrical insulation [61].

2.5.4 Common Circuit Infrastructure

The circuit designs for **IMDs** are strongly influenced by the constraints posed by **NFIC** systems, as discussed in section 2.4. When these systems operate in tissue environments, the loose coupling between coils often results in low **PTE** to the receiver. Consequently, various solutions are prevalent in the literature to optimise power transfer under such conditions.

As an example, in 2022, Zhang et al. published a paper regarding a self-reporting impedance measuring platform for vascular implants [63]. The **IMD** in this paper made use of an **IM** network to achieve optimal power transfer to the load. The network used was an L-type matching circuit. Within the publication, it is noted that the use of matching networks is crucial in minimising the RF-DC conversion loss and preventing power reflections. **IM** networks are found extensively in the literature [44, 5]. Chang et al. make use of a T-Type **IM** network in their paper, which they state provides greater flexibility than L-type matching [40]. Similarly, Yang et al. make use of T-type **IM** over L-type, noting that, unlike L-type, T-type matching does not require that coils have precise inductance and capacitance ratings which makes it a more tolerant system [39]. They further note that π -type networks were considered for use however they are not commonly used as they cannot attain a high quality factor and narrow band matching because of the general low resistance of coils in biomedical applications.

In addition to mitigating the sensitivity of **PTE** to misalignments, rectification is required to achieve the **Direct Current (DC)** requirements to drive implantable μ -**LEDs**. Various rectifier topologies have been covered in the literature pertaining to single-diode, single-stage voltage multipliers and multi-stage voltage multipliers. The design of which is conducted in Keysight Advanced Design System software in much of the literature [63].

Designing rectifiers for such systems is a complex task. These rectifiers need to be compact enough to fit inside the device, maintain high RF-to-dc conversion efficiency, and produce adequate output voltage at low power levels [5]. Previous rectifier designs for implantable applications achieved efficiencies of 76.1%, 34%, 66.8%, and 70.4% at different power levels but had size limitations or used half-wave rectifier topologies, unable to provide an output voltage exceeding 1V. The two-stage voltage doubler rectifier implemented by Zhang et al. achieved a 93.6% conversion efficiency [63]. Basir et al. designed a voltage doubler coupled with a modified matching network to achieve high a RF-to-DC conversion efficiency of 89% with an output voltage greater than 3V [5].

When examining the circuitry employed in state-of-the-art **IMDs**, it is further essential to offer a concise overview of the necessary primary circuitry for high frequency operations.

2.6 Primary Circuit Considerations

Within the literature, several common power electronics components are prevalent in the primary circuitry. A notable example being the use of power amplifiers, particularly at higher operating frequencies. For instance, in 2017, Yang et al. emphasized the requirement for a high-power amplifier within their primary circuitry and opted for an E Class power amplifier due to its notable efficiency [39]. This choice was complemented by the implementation of a T-type **IM** network to mitigate power reflections from the load back to the source. Additionally, in 2010, Kiani et al. introduced a system in which the primary circuit also incorporated a Class E power amplifier, coupled with a DC-DC converter

[46]. Furthermore, Jow et al. also acknowledged the utilization of a Class E power amplifier to drive their transmitter system [42].

2.7 Summary of Implementations and Findings

The relevant literature within this section commenced with a general overview of neuromodulation in medicine, characterising the introduction of **IMDs** to the field. This was followed by a contextualisation of the field of Optogenetics, indicating the necessity for and prerequisites imposed on **IMDs**. Furthermore, the need for the adoption of **WPT** in this specific context was addressed. A discussion of the methods of **WPT** used in Biomedics followed, before commencing a detailed review of Biomedical applications of **NFIC**. This section covered varying coil systems including two-coil, multi-coil and novel coil systems and geometries. Furthermore, methods of power transfer regulation existing in the literature were engaged with. Following this was an investigation into the nature of existing **IMDs**, regarding specific hardware characteristics such as form factors, mechanical considerations, bio-compatibility and commonly used circuits. Finally, a discussion was made regarding relevant primary circuit considerations. Given the in-depth insight provided by the prior application cases, a summarised contextual of the current field of implementations is presented in Table 2.3.

Table 2.3: Table depicting summary of **NFIC** characteristics found in the literature

Source	Frequency (MHz)	Coil Type	Coil Structure	Coupling (Tissue/Air) %	Efficiency (Tissue/Air) %	IMD Size (mm ²)	Separation (mm)
[39]	13.56	Helical/ PSC	Four-coil	NA/0.075	11.7/19.1	25	10
[42]	13.56	PSC	Two-coil	0.0697/0.0301	30.8/72.2	100	10
[28]	13.56	PSC	Two-coil	NA	58.2/75	250	10
[4]	6.78	PSC	Two-coil	NA/0.015	NA/9.2	5.265	12.5
[44]	1	Planar/Solenoid	Two-coil	NA/0.03	21.6	NA	10
[37]	7.15	PSC	Two-coil	NA	NA/4.1	67.5	5
[64]	13.56	PSC	Two-coil	NA/0.0031	NA/0.56	100	NA
[65]	40	Wire-wound	Three-coil	NA	NA/2.56	1	70
[43]	1	PSC	Two-coil	NA	NA/41.2	NA	10
[43]	5	PSC	Two-coil	NA	NA/85.8	NA,	10
[49]	13.56	Wirewound/Chamber	Four-coil	NA	NA/16	100	60
[40]	NA	PSC	Three-coil	NA	NA/4.5	25	5
[3]	60	PSC	Three-coil	NA/0.002	NA/2.4	1	8

In considering the summarised details in Table 2.3, certain trends are evident. The majority of works make use of an operating frequency of 13.56MHz. Moreover, the use of two-coil systems and **PSCs** is common. Coil coupling falls below 0.1 for most two-coil systems operating at distances in excess of 5mm whilst the **PTEs** achieved vary heavily from 0.56% to 85.8%. In addition to this, the size of **IMDs** vary heavily, the smallest of which makes up an area of 1mm² and the largest an area of 250mm².

Chapter 3

Theoretical Background

The brain has no knowledge until connections are made between neurons.
All that we know, all that we are, comes from the way our neurons are connected.

—Tim Berners-Lee

This chapter aims to build upon the contextual knowledge acquired in chapter 2. The following sections provide a specific theoretical foundation for the concepts that were applied during the hardware design process discussed in chapter 4.

3.1 Near-Field Inductive Coupling

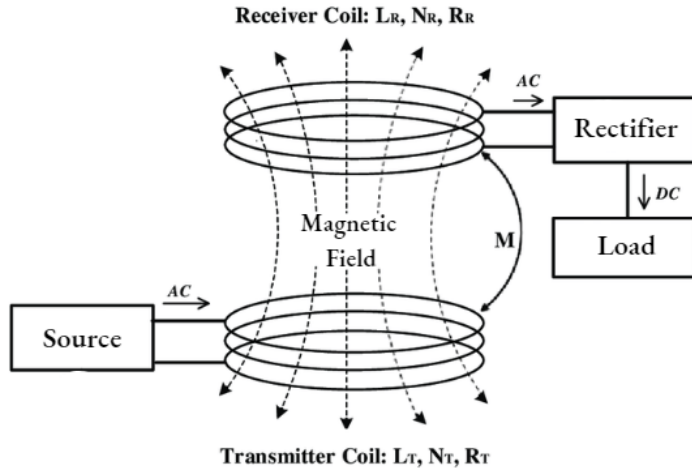


Figure 3.1: Diagram depicting NFIC using a two coil system [7]

NFIC utilises a coil-based system comprising a transmitter and receiver. This mechanism resembles that of an air transformer, where energy transfer occurs through a magnetic field [66]. The transmitter coil is supplied with an alternating voltage to create a time-varying magnetic field. This field generates magnetic flux which, when coupled with the receiver coil, induces an **Electromotive Force (EMF)** in the receiver. As a result of this electromagnetic induction, a current flows in the receiver.

NFIC relies on the fundamental electromagnetic principles of Biot-Savart's Law and Faraday's Law of Electromagnetic Induction. The formation of a time-varying electromagnetic field, $B(r)$, arises

according to the Biot-Savart law as follows:

$$B(\vec{r}) = \frac{\mu_0}{4\pi} \int \frac{I dl \times (\vec{r} - \vec{r}')}{|(\vec{r} - \vec{r}')|^3} \quad [T] \quad (3.1)$$

where μ_0 is the permeability of free space, I is the transmitter current, dl is a unit vector in the direction of the differential length element of wire and $|\vec{r} - \vec{r}'|$ provides a vector pointing from the differential length element to the position of interest.

The property of interest pertaining to Faraday's law of Electromagnetic Induction is the magnetic flux, Φ_B . This property describes the quantity of magnetic field passing through a given surface. The magnetic flux which enters the receiver coil with area vector \vec{A} , namely the linking flux, is calculated as:

$$\Phi_B = \int B \cdot d\vec{A} \quad [Wb] \quad (3.2)$$

And, according to Faraday's law, the induced electromotive force can be calculated as follows:

$$\mathcal{E} = -\frac{d\Phi_B}{dt} \quad [V] \quad (3.3)$$

Equation 3.3 illustrates that the induced **EMF** in the receiver coil is directly proportional to the change in flux entering the coil. Consequently, the time-varying magnetic field generated by the transmitter initiates a current flow within the receiver coil. This project builds upon these fundamental principles to achieve inductive coupling for **NFIC** applications in Optogenetic implants.

3.1.1 Coil Properties and Coupling

The characterisation of the relationship linking the transmitter and receiver coil is of critical importance in understanding the behaviour of an **NFIC** system. The fundamental description of this link can be expressed in terms of the coupling coefficient, k , and mutual inductance, M , of the two coils. The coupling coefficient quantifies the fraction of magnetic flux generated by the transmitter coil which enters the receiver coil. Consequently, a high coupling coefficient indicates strong magnetic linkage between the two coils. This means that a significant portion of the transmitter-generated flux enters the receiver, inducing a greater **EMF**. The coupling coefficient can be calculated as follows:

$$k = \frac{M}{\sqrt{L_1 L_2}} \quad (3.4)$$

Where L_1 and L_2 are the inductances of the transmitter and receiver coils at the frequency of interest. The inductance of a solenoid coil, as used in this project, is represented by:

$$L = \frac{\mu_0 N^2 A}{l} \quad [H] \quad (3.5)$$

Notably, equation 3.5 does not explicitly consider the operating frequency of the coil when calculating its inductance. This formula is based on the assumption of ideal conditions, where material properties are constant, and there are no losses. However, the **NFIC** system in this project operates at high

frequency, where these assumptions do not hold true.

At higher frequencies, variations in inductance become apparent due to the interplay of the skin effect, proximity effect, and the influence of eddy currents [2]. The skin effect, as depicted in Figure 3.2, refers to the tendency of **Alternating Current (AC)** current to concentrate near the surface of a conductor at higher frequencies, reducing the effective cross-sectional area of the coil. Additionally, the proximity effect, depicted in Figure 3.3 is observed when conductors are closely positioned at high frequencies, leading to a preferential flow of **AC** current along their facing sides. Furthermore, the influence of eddy currents induced in adjacent conductive materials becomes more pronounced with increasing frequencies, collectively contributing to variances in coil inductance from the theory outlined in equation 3.5.

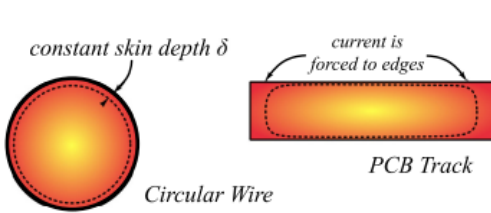


Figure 3.2: Diagram depicting the skin effect occurring at high frequencies [2]

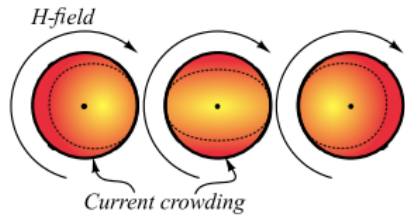


Figure 3.3: Diagram depicting the proximity effect occurring at high frequencies [2]

The relationship relating the voltage induced in the receiver to properties of the **NFIC** coil link and supplied alternating voltage is characterised by equation 3.6.

$$V_2 = kV_1 \sqrt{\frac{L_2}{L_1}} \quad [V] \quad (3.6)$$

In practical terms, the coupling coefficient provides valuable insights into how the coil structure, alignment, and geometry influence the efficiency of energy transfer between coils. A higher coupling coefficient allows the induced voltage at the secondary to be achieved with a significantly smaller voltage driven in the primary circuit. Consequently, this reduces the current in the primary circuit, minimizing primary losses. By reducing the need for high power delivery from the primary to receive small amounts of power at the secondary, the magnetic field strength can be diminished, enhancing safety when interacting with biological tissue. Achieving optimal coupling necessitates careful consideration of various factors, including the distance between the coils, the alignment of the coils, the number of turns, as well as the shapes and sizes of the coils.

3.1.2 Resonance

Resonance is achieved by adjusting the frequency of the **AC** in the primary¹ coil to align with the system's inherent natural resonant frequency, resulting in enhanced **PTE**. Tuning the system involves adjusting its reactive properties to match a desired operating frequency. This is achieved by integrating capacitor compensation networks into both the primary and secondary circuits. During resonance

¹Within this report, usage of the term 'primary' references the transmitter side of **WPT** and 'secondary' references the receiver side.

the system's impedance is minimized, primarily due to the elimination of the net reactive impedance resulting from the 180° phase shift between the inductor and capacitor's reactances, X_L and X_C . This reduction leaves behind only resistive losses, thereby enhancing [PTE](#) from the primary to the secondary. The system's natural resonant frequency is calculated using equation 3.7, which is commonly utilised to determine the required capacitor compensation for a given operating frequency.

$$f_{\text{res}} = \frac{1}{2\pi\sqrt{LC}} \quad [\text{Hz}] \quad (3.7)$$

3.2 Compensation Networks

The integration of compensation networks into both primary and secondary circuits plays a critical role in obtaining efficient power transfer in [WPT](#). Numerous established methods exist for implementing these compensation networks. This project primarily focuses on single resonant compensation, encompassing configurations of compensation capacitors such as [S-S](#), [S-P](#), [P-S](#), [P-P](#), and [IM](#) networks.

3.2.1 Compensation Capacitor Configurations

Transmitter and receiver coils operating at resonant frequencies lower than their self-resonant² frequencies necessitate compensation capacitors to achieve resonance in the primary and secondary circuits [67]. Primary-side compensation aims to minimize apparent power on the input side, reducing the necessary current driven by the source [68]. This reduction in primary current significantly mitigates primary losses. Compensation in the secondary circuit is geared toward the maximization of the system's power transfer by negating the losses associated with the receiver coil inductance [68].

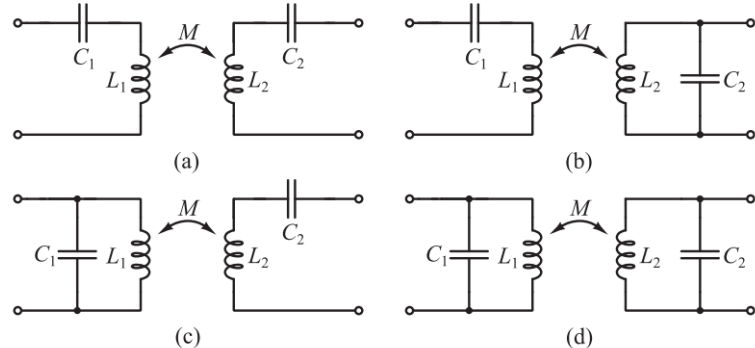


Figure 3.4: Figure depicting various single resonant compensation techniques [2]. a.) [S-S](#) b.) [S-P](#) c.) [P-S](#) d.) [P-P](#)

Depending on the utilization of these network configurations, control over power transfer in a [WPT](#) system can be exerted through the primary circuit, the secondary circuit, or a combination of the two. In applications related to wireless charging, opting for primary-side control proves advantageous as it eliminates the necessity for a DC-DC converter stage on the secondary side, instead substituting it with a rectifier and filter [69]. The elimination of the DC-DC converter stage yields notable efficiency improvements as well as a reduced form factor. This approach is commonly adopted in biomedical

²The frequency at which the coil's inductance and parasitic capacitance resonate with each other and cancel the net reactive effect of the coil.

applications due to its potential to facilitate a more compact system, resulting in a suitable implant that is both small and lightweight.

Furthermore, a careful selection of a suitable compensation network can provide the capability to regulate voltage and/or current output, enabling load-independent current or voltage outputs. Table 3.1 presents a comprehensive overview of the advantages and disadvantages associated with different compensation networks [67, 68, 69, 70].

Table 3.1: Advantages and Disadvantages of Single Resonant Compensation Networks [68]

Compensation	Advantages(A)/Disadvantages(D)
S-S	<ul style="list-style-type: none"> A: Primary/Secondary compensation independent of coupling coefficient/load variations at the resonant frequency. A: Higher system efficiencies achieved at lower coupling coefficients. A: Unity power factor at resonance and low sensitivity to misalignments. D: Poorer efficiencies at lighter loads.
S-P	<ul style="list-style-type: none"> A: Primary/Secondary compensation independent of coupling coefficient/load variations at the resonant frequency. A: Lower receiver coil self-inductance requirement than S-S. D: Current control at primary-side is required thus increasing system complexity. D: Power factor varies as a function of the link mutual inductance. D: Resonant frequency may change depending on coupling coefficient, yielding a change in primary capacitance.
P-S	<ul style="list-style-type: none"> A: Higher efficiency and power factor at low mutual inductances/during variations in load. D: Requires current source input. D: Primary compensation capacitor is dependent on both coupling and load variations. D: Higher source voltages are required for power transfer to compensate for high input resistance.
P-P	<ul style="list-style-type: none"> A: Provides constant current operation which is beneficial for applications such as battery charging. D: Primary compensation capacitor is dependent on variations in coupling/load. D: The input requires a large current source and low power factor. D: A higher load voltage is needed at the secondary side.

3.2.2 Impedance Matching

IM is a technique employed to reduce losses caused by power reflections. An in-depth analysis of power reflection behavior is intricate and not extensively covered in the relevant literature, consequently a surface-level comprehension suffices for the scope of this paper.

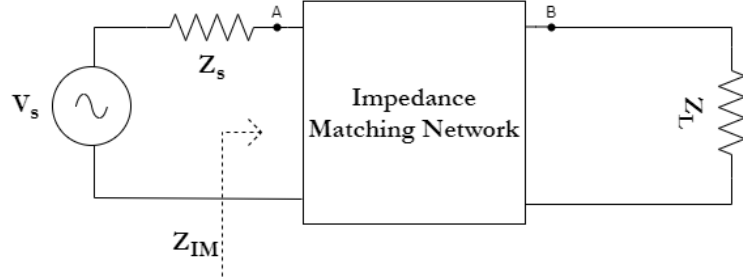


Figure 3.5: Figure depicting the role of an **IM** network

The selection of an appropriate **IM** network configuration follows the principle of maximum power transfer. This principle asserts that the most efficient power transfer between a source and a load occurs when the load impedance matches the complex conjugate of the source impedance. As illustrated in Figure 3.5, when the source and load impedances, Z_s and Z_L , are not complex conjugates an **IM** network is introduced between the source and load [71]. This network is designed to make the resistance seen from the source into the **IM** network, Z_{IM} , appear to be the same as the source impedance. Achieving **IM** is accomplished by inserting a matching network, typically in the form of an LC network, between the source and load. In **NFIC** applications, **IM** is utilized in the secondary to align the impedance of the load with that of the receiver coil. Moreover, **IM** is also implemented in the primary to match the impedance of the transmitter seen from the source impedance.

3.3 Power Amplifiers

In instances of high frequency operation, the utilization of inverters is infrequent due to cost considerations. As highlighted in the literature in section 2.6, a practical alternative at frequencies in excess of $10KHz$ to $10MHz$ involves the combination of a high frequency signal generator with a power amplifier [69].

Due to the inherent inefficiencies in miniaturized **NFIC** links, highly efficient power amplifiers are essential. Class D and Class E Power Amplifiers are ideal for driving high frequency circuits, often achieving efficiencies exceeding 90%. While both are suitable for **WPT**, this theory section focuses on Class E amplifiers due to their relevance to this project. Class E amplifiers achieve high efficiencies through zero voltage and zero current switching. This technique significantly reduces power losses associated with transistor switching. However, designing and implementing Class E amplifiers can be more complex due to the precise tuning and synchronization needed to achieve zero switching characteristics at specific loading conditions.

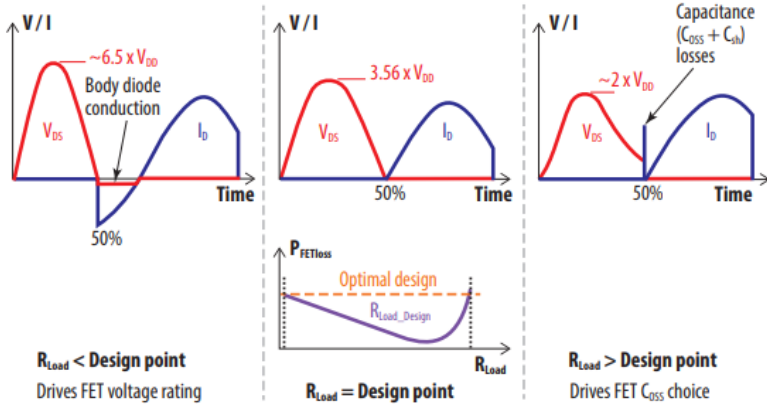


Figure 3.6: Figure depicting the performance of a Class E amplifier under various tuning cases [8]

The first waveform in Figure 3.6 illustrates a load condition smaller than the design value. In this case, during switching, the current drawn from the amplifier spikes rapidly, prompting an increase in the supply voltage to achieve the required output power [8]. Consequently, there is a marked voltage increase across the Field Effect transistor, leading to body-diode conduction during the device off period which results in losses. The second waveform represents ideal conditions where there is no overlap between voltage and current waveforms, ensuring zero switching and minimizing losses. The third waveform demonstrates a scenario where the load condition exceeds the design value. During switching, a residual voltage across the switch causes a shunt capacitance, resulting in losses [8].

3.4 Inductive Link Equivalent Circuit Theory

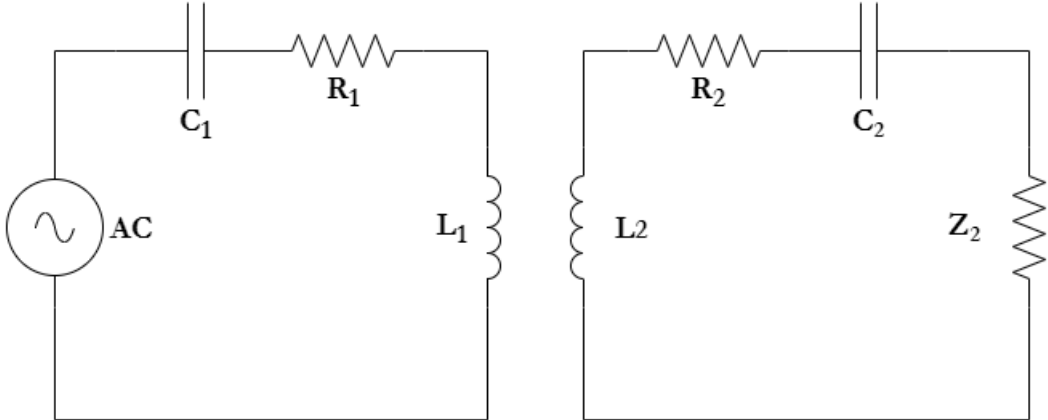


Figure 3.7: Diagram depicting Equivalent Circuit of a two-coil NFIC system

In Figure 3.7, a simple representation of an **S-S** compensated **NFIC** system is presented. The schematic portrays the primary circuit situated on the left-hand side, comprising an **AC** source, a compensation capacitor, C_1 , and the transmitter coil, L_1 , along with its associated equivalent series resistance, R_1 . R_1 characterizes losses attributed to conduction and eddy currents arising from the skin and proximity effects. The secondary comprises the receiver coil, L_2 , its series resistance, R_2 , compensation capacitor, C_2 , and a dynamic load symbolized by Z_2 . The dynamic load comprises a rectification stage and dynamic resistance, representing a generic case of **NFIC**.

3.4.1 Link Impedance

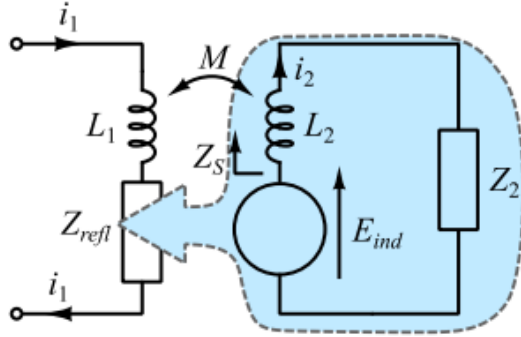


Figure 3.8: Figure depicting the reflected impedance into the primary [2]

As described by Terman, the current driving the primary coil induces a voltage, E_{ind} in series with the secondary coil [2]. This induced voltage appears as a reflected impedance in the primary circuit, as depicted in Figure 3.8. It is crucial to account for this reflected impedance when analyzing the primary circuit, specifically when considering both the load that the power amplifier is driving and the required IM conditions.

3.4.2 Load Power

The output voltage seen across the load, V_{out} , can be denoted in terms of the induced voltage in the secondary as follows:

$$v_{out} = \frac{E_{ind}Z_2}{R_2 + j\omega L_2 + \frac{1}{j\omega C_2} + Z_2} \quad (3.8)$$

Hence, the true power³ delivered to the load can be solved as follows:

$$P_{out} = \frac{|v_{out}|^2 \Re\{Z_2\}}{|Z_2|^2} \quad (3.9)$$

In interpreting Equation 3.9, it is evident that maximum power transfer to the load occurs when both V_{out} and Z_2 are purely real. This scenario represents a unity power factor, occurring at resonance. Furthermore, the maximum power transfer theorem applies where, at resonance, R_2 must equal Z_2 .

3.4.3 Power Transfer Efficiency

The efficiency of the primary circuit is given by the power delivered to the reflected impedance as a fraction of the input power supplied by the source. The efficiency in the secondary circuit is given by the power delivered to the load as a fraction of the power supplied by the reflected impedance.

$$\eta_1 = \frac{P_{Z_{ref}}}{P_{in}} \quad (3.10)$$

$$\eta_2 = \frac{P_{out}}{P_{Z_{ref}}} \quad (3.11)$$

³The real power dissipated in the load with units of Watts.

The efficiency of the **NFIC** link, η_{link} can be depicted as the combination of the two efficiencies of the primary and secondary circuits.

$$\eta_{link} = \frac{P_{out}}{P_{in}} \quad (3.12)$$

The calculated losses for each coil can be considered as a proportion of the coil's reactive impedance, characterized by its quality factor, Q , denoted as follows [2]:

$$Q_1 = \frac{\omega_0 L_1}{R_1} \quad (3.13)$$

$$Q_2 = \frac{\omega_0 L_2}{R_2} \quad (3.14)$$

Furthermore, the maximum transmission efficiency for a **S-S** system is often given in terms of the transmitter and receiver quality factors, Q_1 and Q_2 [68].

$$\eta = \frac{k^2 Q_1 Q_2}{(1 + \sqrt{1 + k^2 Q_1 Q_2})^2} \quad (3.15)$$

3.5 Rectification

NFIC utilizes **AC** excitation for power transfer. As a result, the signal detected by the receiver is **AC**. However, the typical operation of the receiver's load requires a **DC** voltage. Therefore, a rectifier is necessary to convert the received **RF** power into **DC**. While conventional bridge rectifiers are commonly used in **WPT** applications, they find less application in **IMDs**. This is primarily due to the low power and low voltage nature of **IMDs**, where bridge rectifiers tend to be inefficient [5]. Consequently, Dickson-Villard voltage doublers are commonly adopted in these applications, in both single and double stages based on the required voltage and power at the load, followed by a low pass capacitor as seen in section 2.5.4.

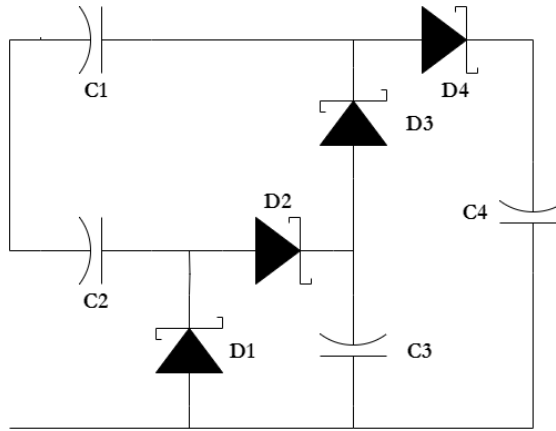


Figure 3.9: Figure depicting a two-stage voltage doubler circuit

A two-stage voltage doubler is depicted in Figure 3.9, the function of this circuit is to quadruple the voltage seen at the input across output. The DC passing capacitor filters the **AC** voltage doubler output signal into DC. The two-stage voltage doubler operates as follows: during the negative half-cycle, diode D2 charges capacitor C2 while in the positive half-cycle, D2 is forward-biased and D1 is reversed,

preventing the discharge of fully charged C2. This arrangement leads to the addition of an equal voltage to the input, charging C3 and doubling the input's peak voltage. In a multistage setup, the output voltage of the first stage charges the capacitor C1 in the next stage, thus boosting the peak rectified voltage to the required level [72].

3.6 Magnetic Field Safety

The [ICNIRP](#) provides [guidelines](#) to limit human exposure to time-varying electromagnetic fields up to $300GHz$ due to potential health risks associated with high power [RF](#) fields. Their publication aims to establish protective exposure limits that guard against proven adverse health effects from both short- and long-term, continuous, and discontinuous [RF](#) exposure [73]. While the guidelines encompass comprehensive safety regulations, this report specifically focuses on the permissible magnetic field strength, [SAR](#) and temperature variances at relevant megahertz frequencies. The [ICNIRP](#) guidelines establish specific criteria for safety at $13.56MHz$. As seen in the details provided in section [A.1](#) of the Appendix, the allowable local magnetic field strength is restricted to $80A/m$. Furthermore, the accepted [SAR](#) should not exceed $10W/kg$. Additionally, the temperature increase is considered safe within the range of 1 to $2^{\circ}C$.

3.7 Summary of Theoretical Background

The theoretical foundation presented in this section commenced with a general overview of [NFIC](#). In the context of [NFIC](#), a clear explanation was provided regarding the formation of inductive links between coils, relying on fundamental field theory principles. This initial discussion laid the groundwork for a comprehensive exploration of the electrical properties intrinsic to inductive links. This exploration encompassed aspects such as coil coupling, inductance, losses attributed to high frequency resistive elements, and the various factors influencing coil coupling.

The next section initiated a discussion on resonance which aimed to introduce the reader to the mechanisms used in ensuring optimal power transfer. This resulted in further discussion surrounding the topics of compensation networks and [IM](#). Following this, a brief characterisation of power amplifiers ensued. A discussion was raised regarding a means to characterise power transfer through equivalent circuit theory. Within this section mathematical formulae were provided to assist the reader in understanding the underpinnings of reflection theory and quantitative power transfer. These derivations shed light on the means to characterize link impedance, quantify power delivered to the load, and ascertain [PTE](#). This was followed by a discussion of the rectification techniques implemented at low power.

Finally, mention was made regarding the necessary safety frameworks that require cognisance when implementing high frequency [WPT](#). The theoretical framework provided in this section serves to provide a technical framework for comprehending the subsequent design procedures outlined in chapter [4](#).

Chapter 4

System Design and Simulation

The human brain is the supreme creator of all fortune. It is the biggest miracle of nature which makes all other miracles possible.

—Abhijit Naskar

This chapter delves into the design process employed for implementing the [WPT](#) Optogenetic system. The decisions outlined in this chapter were leveraged using the knowledge acquired from chapters [2](#) and [3](#). Given the complexity of designing a system with numerous intricate components which rely on one another, breaking the project down into manageable subsystems was crucial to meet the specified time constraints. Consequently, the full [WPT](#) Optogenetic system was divided into three distinct parts, focusing on the primary power electronics, the [NFIC](#) link, and the Optogenetic receiver circuitry alongside the manufactured [PCB](#). This approach enabled the underlying complexities of each of these modules to be addressed in turn, thus reducing the potential for bottleneck in system design which was particularly important given the extended lead times associated with the hardware manufacturing process.

4.1 Design Process

The initial phase of this project involved formulating a foundational hardware structure, necessitating the identification of the system's fundamental characteristics. Once this overarching structure was established, attention was directed towards the Optogenetic [IMD](#). This focus stemmed from concerns regarding a potential bottleneck during the manufacturing process. Consequently, this phase entailed the design of the various circuit elements constituting the receiver. Early on, it became apparent that insight into the electrical properties related to the [NFIC](#) coil link was crucial for certain aspects of the receiver's design. This realization prompted a shift towards the simulated design of the coil system to be utilized. After conducting suitable simulations and validating an [NFIC](#) coil system, emphasis was redirected towards expediting the design-to-manufacture process of the [IMD](#). Once manufacture of the [PCB](#) commenced, the primary side electronics were designed. Upon completion of all stages, the entire system was implemented. The trajectory of this design process is summarized in Figure [4.1](#).

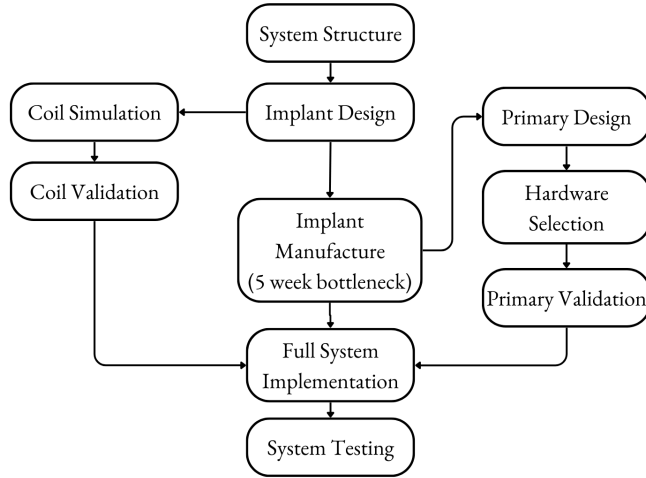


Figure 4.1: Figure depicting a flowchart of the project timeline

4.2 Foundational Characteristics of the System Architecture

The project's outset required the selection of an appropriate **WPT** framework, taking into account the necessary constraints including the system's operating frequency, coil structure and **IMD** geometry. This served to lay the groundwork for the simulation design process.

4.2.1 Wireless Power Transfer Protocol Selection

As outlined in chapter 2, section 2.3, a variety of **WPT** technologies are used in **IMD** applications. Notably, **IMDs** often utilize **NFIC** due to its ability to direct power rather than radiate it. This is more efficient and safer for Biomedical applications. Consequently, the project's scope was focused on **NFIC**, motivated by its consistent usage in current literature and the flexibility it offers in designing coil geometry. The choice of the system's operating frequency was guided by the potential for smaller coil dimensions achievable at higher frequencies. Typically, higher frequencies lead to increased tissue absorption, thereby reducing penetration depth and compromising device safety ratings. The selection of 13.56MHz , however, ensures enhanced efficiency and compactness without compromising on absorption, as would be seen in the gigahertz frequency range. In addition to this, in considering table 2.3, an operating frequency of 13.56MHz finds common use. Given the selection of an operating frequency of 13.56MHz , non linear effects noted in section 3.1.1 are bound to arise. Therefore, the analysis of coil behaviour requires the use of **FEA** software.

4.2.2 Coil Link Structure

Whilst the advantages of multi-coil structures identified in section 2.4.2 are significant, the scope of this project was focused on a dual-coil structure. This decision aimed to avoid the complexity associated with multi-coil structures, considering the time constraints of this project. Benefits which arise from multi-coil structures in the form of increased coupling and **IM** could be accounted for in the scope of this project through the introduction of an **IM** network in the primary/secondary. A primary objective of this project is to develop an implant comparable to existing hardware in size. Section 2.5.1 in chapter

2 indicates that smaller implants typically range from 2x3mm to 10x10mm [55]. Thus, a geometric constraint of 2x3mm was set on the PCB for this project. In previous works, receiver coil sizes were in the scale of 2mm. Consequently, the receiver's geometry in this project will be constrained to a similar size.

4.2.3 System Structure

The system architecture is illustrated in Figure 4.2. As detailed in section 3.3, a signal generator operating through a power amplifier is chosen to generate the required voltage for driving the compensated transmitter coil. An NFIC link supplies power to the receiver, wherein the receiver coil is coupled with compensation, followed by the dynamic load. This dynamic load encompasses a dual-stage voltage doubler circuit and a μ -LED.

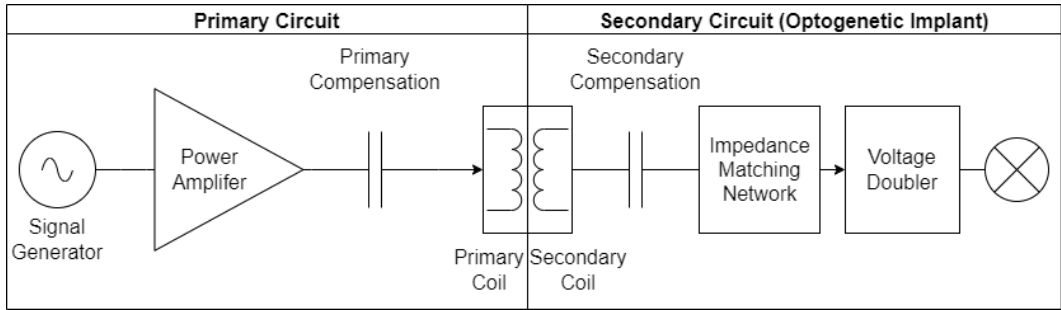


Figure 4.2: Diagram depicting the Optogenetic system architecture

4.3 Near-Field Inductive Coupling Characteristics

Figure 4.3 illustrates the iterative process undertaken to implement the coil design in simulation. The initial step in designing the link involved identifying the constraints and objectives of the link system. These constraints formed the basis for determining the coil geometry, which was essential given the specific use case and the objective of minimizing hardware volume.

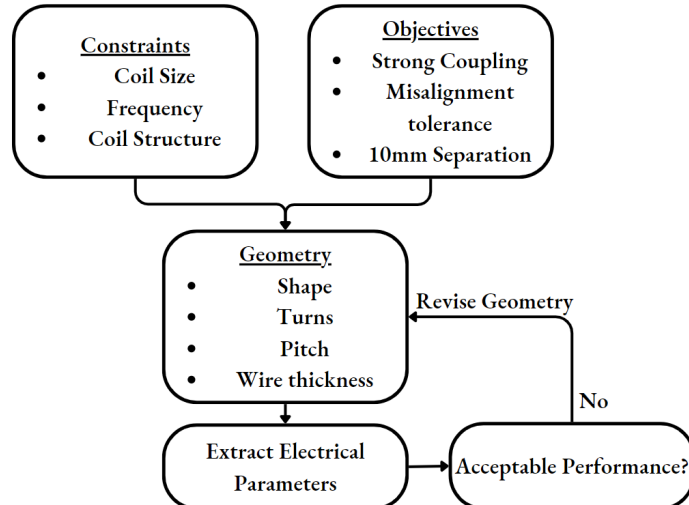


Figure 4.3: Diagram depicting design process undertaken for the NFIC link

4.3.1 Inductive Link Constraints

The design of the coils' geometry, encompassing both their volume and physical shapes represent an initial overarching constraint. The geometry of the transmitter is relatively less critical than that of the receiver, allowing for transmitter optimisation after selecting a suitable receiver. The receiver's geometry is heavily constrained by the implant's specific application. In the case of an Optogenetic implant which is intended for placement in the human head between the skull and cerebral cortex, space is limited. Given the increased [PCB](#) size associated with planar coils, a decision was made to design the receiver coil as three-dimensional, enabling a smaller [PCB](#) area, and adhering to dimensions within the margin of $2mm$ to align with the current state-of-the-art.

Another identified constraint is the distance separating the transmitter and receiver coil. Due to the use case requiring the implant's proximity to the cerebral cortex, this distance needed careful consideration for optimal operation. While an exact biological analysis is beyond the scope of this report, it was noted that the average distance to the cerebral cortex from the outside of the skull is approximately $10mm$ [74]. Therefore, simulations and practical implementations were conducted with a coil separation of $10mm$.

Furthermore, biological compatibility imposed a significant constraint on the inductive link, limiting the types of materials that could be used within the human body. Specifically, the use of a magnetic core within the receiver coil was prohibited as it would render the devices unsafe for placement as noted in the discussion regarding the system implemented by Delhaye et al. in section 2.4.1 [44]. Consequently, simulations and designs were not conducted with the use of a magnetic core. It was further noted in the literature, section 2.5, that subcutaneously implanted [IMDs](#) undergo small motions due to biological interactions. Consequently, the coil link must exhibit robust misalignment tolerance.

4.3.2 Inductive Link Objectives

With these constraints defined, the objectives of the [NFIC](#) link were outlined to serve as validation criteria for the system:

- The simulation must maintain sufficient coupling comparable to documented literature outlined in Table 2.3 at a separation distance of $10mm$.
- The simulation must demonstrate tolerance to misalignment conditions, resulting in minimally excessive reductions in coupling.
- The simulation must operate at $13.56MHz$.
- The simulation must adhere to safety margins outlined in section 3.6.
- The simulation must translate to practical implementation.

4.4 Near-Field Inductive Coupling Simulated Coil Design

The software chosen to model the [NFIC](#) link and analyze its performance is Ansys, an [FEA](#) software. Specifically, three ANSYS packages were selected for this project: Maxwell 3D, [High Frequency Simulation Software \(HFSS\)](#), and IcePak. Maxwell 3D, being the core environment, is designed for

simulating and analyzing electromagnetic systems. This platform enables the calculation of electrical coil parameters such as inductances and coupling. This makes Maxwell 3D highly efficient in streamlining the otherwise intensive and iterative practical task of coil design. [HFSS](#) and [IcePak](#) were utilized to conduct [SAR](#) and temperature analysis for the [NFIC](#) link accordingly.

To commence the process of coil design, it was vital to establish a performance benchmark that could serve as a reference for subsequent design iterations. Considering the extensive nature of coil design optimisation techniques and the time constraints associated with coil design, such that a swift progression could be made to [PCB](#) design to expedite manufacturing, the complete optimisation of a coil link is beyond the scope of this report. Attaining a functioning link comparable to existing literature was identified as a suitable objective within the scope of this project. To facilitate this, the design process commenced by modeling the system used by Bansal et al. which closely resembles the use case of this project's [NFIC](#) link [11].

4.4.1 Benchmark Design

Notably, the system implemented by Bansal et al. operated with a *3mm* coil separation gap, as it was designed for use with rodent specimens.

System Modelling



Figure 4.4: Figure depicting receiver modelled in benchmark simulation



Figure 4.5: Figure depicting transmitter modelled in benchmark simulation

Dimensions (mm)	Tx	Rx
Inner Diameter	3.4	1.6
Outer Diameter	5	1.727
Pitch	NA	0.67
Length	12	2
Wire diameter	0.8/0.2	0.127

Figure 4.6: Benchmark [FEA](#) Parameters

The transmitter depicted in Figure 4.5 was modeled based on a standard commercial [RFID](#) transmitter, as illustrated in Figure A.3 in the Appendix. It was considered that one of these [RFID PCB](#) transmitter coils should be procured for use. However, it became evident that finding a commercial [RFID](#) coil with geometry precisely matching the simulated design was improbable. Therefore, the more feasible approach involved hand-winding these coils. This would prove to be a process that was more accessible and conserved the budget for the manufacture of the receiver [PCB](#).

The simulation was conducted twice to gather benchmarking data. The initial collection of data was done with the coils positioned along the z-axis with a separation distance of *3mm* as reported by Bansal et al. [11]. The second phase aimed to assess the same coil performance at the separation distance of *10mm* as identified in the scope of this project. This comparison allowed for a clear understanding of the necessary coupling improvements that needed to be made.

System results

The coil properties attained under nominal conditions¹ with a $3mm$ separation are depicted in Table 4.1

Table 4.1: Table depicting results obtained during Bansel et al. simulation setup

Coupling Coefficient (k)	Receiver Inductance, L_{RX} (nH)	Transmitter Inductance, L_{TX} (nH)	Mutual Inductance, $L_{TX/RX}$ (pH)
0.007954	28.44	13.27	154.52

To ensure comprehensive benchmarking data, simulations were conducted to assess the robustness of the coils under potential misalignment conditions. These misalignments were designed to simulate situations that could arise during the subcutaneous implantation of the receiver, encompassing both lateral and rotational misalignments between the coils.

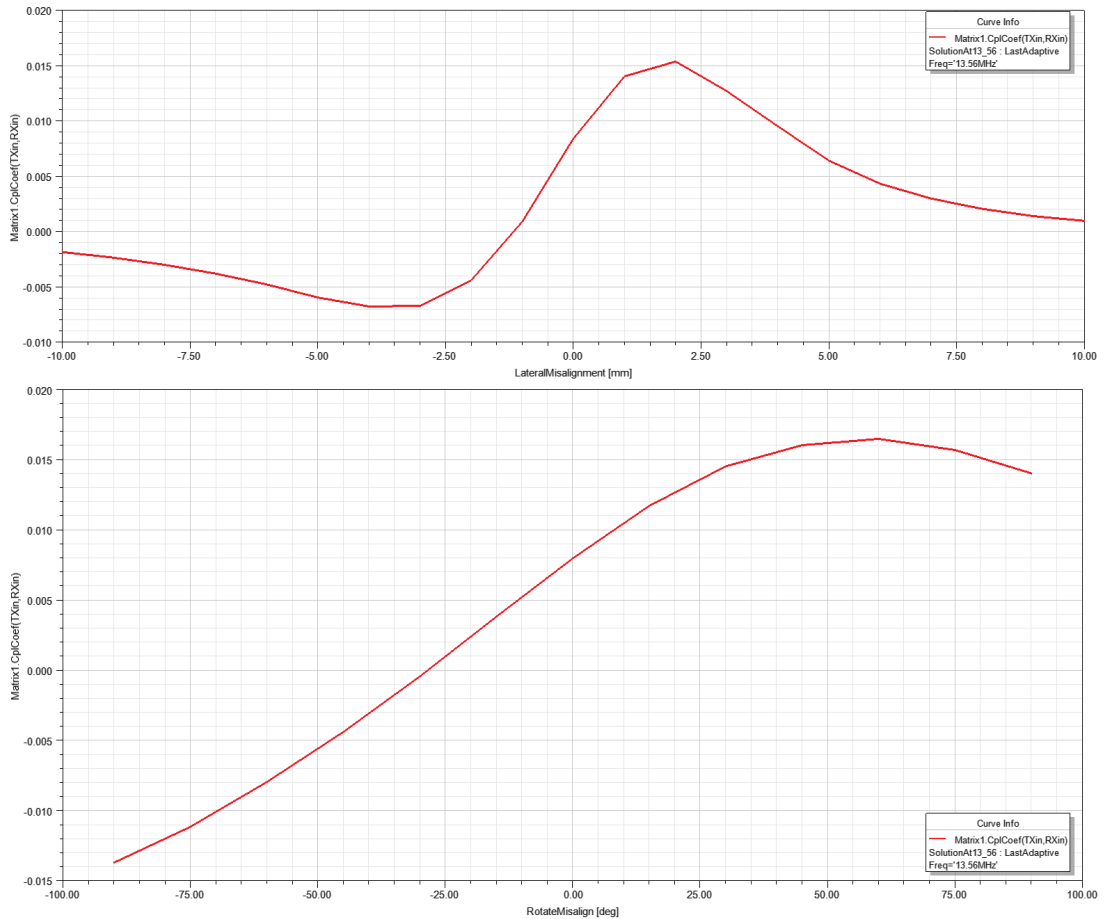


Figure 4.7: Figure depicting the results of the lateral and rotational misalignment tests

The plots depicted in Figure 4.7 provide a graphical depiction of the coil's misalignment properties. Notably, the coils exhibited optimal performance at a 60° misalignment, achieving a peak coupling of 0.0165. The explanation of this result can be construed from Figure A.5 in the Appendix. The proximity of the coils enables the receiver to capture both perpendicular and parallel flux from the transmitter coil at this misalignment. Consequently, coupling performance is enhanced at this misalignment compared

¹Nominal conditions are defined as the placement of the receiver coil $10mm$ above the transmitter coil without any rotational misalignments.

4.4. Near-Field Inductive Coupling Simulated Coil Design

to a perfectly vertical coil orientation. For similar reasons the optimal positioning of the receiver was found to be displaced 2mm from the axis of the transmitter yielding a coupling of 0.0155.

Given the changes in the flux characteristics which would occur in transitioning from 3mm to 10mm, the decision was made not to use 0.0155 as the nominal coupling benchmark because this same increase in coupling resulting from the summation of parallel and perpendicular flux could not be ensured at a 10mm distance. The extreme misalignment conditions were ultimately not considered for acceptable variance ranges at 3mm, where there would be minimal parallel flux compared to 10mm. Extreme bounds for acceptable variance ranges were selected at 15° misalignment to balance the lack of parallel flux at 3mm with the increase of parallel flux at 10mm. This is explained as greater reductions would occur at 3mm at large rotations than would occur at 10mm for the same rotations due to the increase in parallel flux as a function of distance from the transmitter. Moreover, a lateral misalignment extreme of 5mm was selected.

Table 4.2: Table depicting 3mm benchmark coupling results

Nominal Coupling	Lateral Misalignment acceptable reduction (%)	Rotational Misalignment acceptable reduction(%)
0.007954	19.53	50.97

The results at a vertical separation of 10mm are depicted in Figure 4.8 and table 4.3.

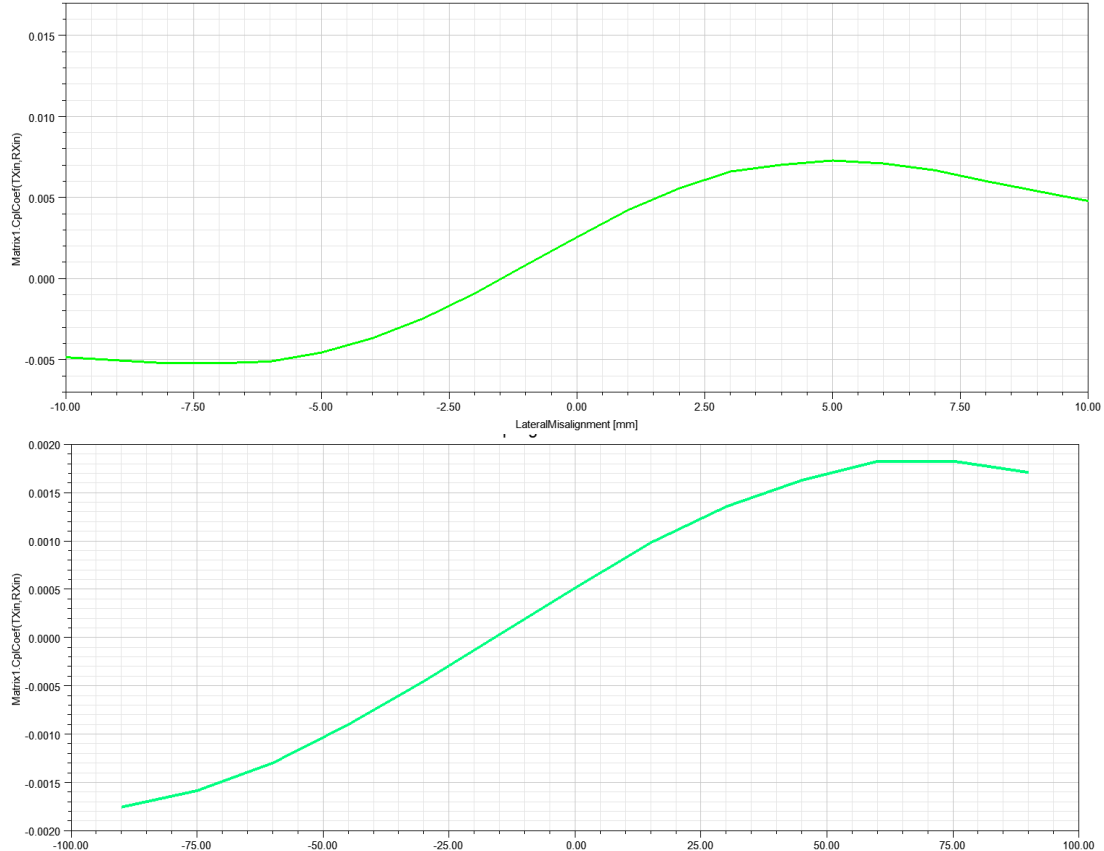


Figure 4.8: Figure depicting the results of the Lateral and Rotational Misalignment Tests

Table 4.3: Table depicting results obtained during benchmark simulation setup at 10mm coil separation

Coupling Coefficient (k)	Receiver Inductance, L_{RX} (nH)	Transmitter Inductance, L_{TX} (nH)	Mutual Inductance, $L_{TX/RX}$ (pH)
0.000513	30.43	13.22	10.29

The low nominal coupling indicates that this setup is inadequate in achieving the link's objectives. It was noted that an issue likely stems from the very low transmitter inductance. Therefore, a comprehensive redesign involving changes to the transmitter shape, volume, and the number of turns was identified as the next step.

4.4.2 Iterative Design Process

The design process of the inductive coil link was inherently iterative, exploring numerous coil geometries and dimensions. These design variations followed the same implementation process to that of the benchmarked system. Given the substantial number of designs generated during this phase, not all of them will be discussed. However, the designs that played a crucial role in shaping the thought process during this phase will be briefly discussed before delving into the final selected link.

The first key design change involved switching the transmitter from a solid design to a wire-wound structure. As noted in section 4.4.1 this shift was prompted by the realization that using a commercial **RFID** transmitter would restrict the adjustable parameters for optimising the transmitter. An optimisation process revealed that the highest coupling achievable occurs with transmitter dimensions using an inner diameter of $9.64mm$ and an outer diameter of $32.13mm$. The performance of this simulation is depicted in Table 4.4, design [1], with comprehensive results in Appendix section A.3.1. The coupling coefficient at a coil separation of $10mm$ closely approached that of the benchmarked system at $3mm$, showcasing promise for this design.

The next significant design change aimed to enhance the misalignment tolerance of the coil link. This involved the implementation of a novel double helix receiver coil structure, strategically designed to capture both perpendicular and parallel flux as noted in the $3mm$ benchmark simulation. The double helix receiver structure is illustrated in Figure 4.9 and is detailed further in the Appendix in Figures A.10 and A.9.

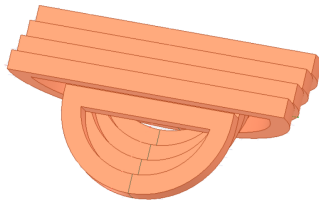


Figure 4.9: Figure depicting the geometry of the double helix receiver

Notably, the performance of the double helix structure proved to be significantly worse than the previous designs. The corresponding results are shown in Table 4.4, design [2], with comprehensive results in section A.3.2 of the Appendix. Given this poor performance and the impracticality of winding

4.4. Near-Field Inductive Coupling Simulated Coil Design

such a complex shape on a small scale, this concept was abandoned. A decision was made to return to solenoid receivers, given their simpler shape for winding and their superior comparative performance.

An investigation was carried out to evaluate the impact of increasing the number of receiver turns on coupling, following the theory outlined in section 3.1.1. Adhering to the coil length constraint of 2mm, a 15-turn coil was attainable with a wire width of 0.127mm and a 0.135mm pitch between turns. This receiver was coupled with the same wire-wound transmitter as used previously and is illustrated in Figures A.13 in the Appendix. The simulation results are presented in Table 4.4, design [3].

Table 4.4: Table depicting coil nominal and misalignment coupling conditions obtained during iterative design process

Design	Nominal Coupling	Lateral misalignment reduction (%)	Rotational misalignment reduction(%)
3mm Benchmark	0.007954	19.53	50.97
10mm Benchmark	0.000513	100	100
[1]	0.006868	22.83	10.45
[2]	0.003813	32.60	14.76
[3]	0.008655	28.79	24.90

Whilst the selection of design [3] appeared to be suitable to the application given its large increase in coupling with a minimal reduction in misalignment tolerance, it became apparent that the task of practically winding the coils would be better suited to a circular coil than a rectangular coil in terms of jig manufacture and difficulty. This was identified due to the characteristics of the copper wire used and will be briefly expanded upon in section 5.2.1. Hence, the final design of the transmitter was revised to be circular.

4.4.3 Accepted Link Design

The final design iteration replaces the rectangular wire-wound transmitter with a circular wire-wound transmitter to address concerns regarding the physical manufacture of the transmitter coil. Additionally, the inner diameter of the receiver coil was varied to assess the potential increase in coupling that could be achieved with a minimal diameter increase. This led to the choice of a 2.2mm inner diameter solenoid.

System Modelling

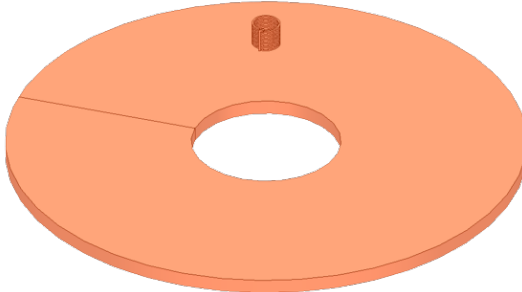


Figure 4.10: Figure depicting the simulated model for the final design

Dimensions (mm)	Tx	Rx
Inner Diameter	13	2.2
Outer Diameter	45.258	2.454
Pitch	0.086	0.127
Length	NA	1.905
Wire width	0.64516	0.127

Figure 4.11: NFIC FEA Parameters

System Results

A process was initiated to determine whether the simulated setup met all of the required objectives. Again, this included a nominal coupling test alongside misalignment tests. The inductive properties pertaining to the transmitter and receiver coils are depicted in Table 4.5.

Table 4.5: Table depicting simulated inductive properties of Optogenetic [NFIC](#) link

Coupling Coefficient (k)	Receiver Inductance, $L_{RX}(nH)$	Transmitter Inductance, $L_{TX}(\mu H)$	Mutual Inductance, $L_{TX/RX}(nH)$
0.011730	364.04	16.75	28.97

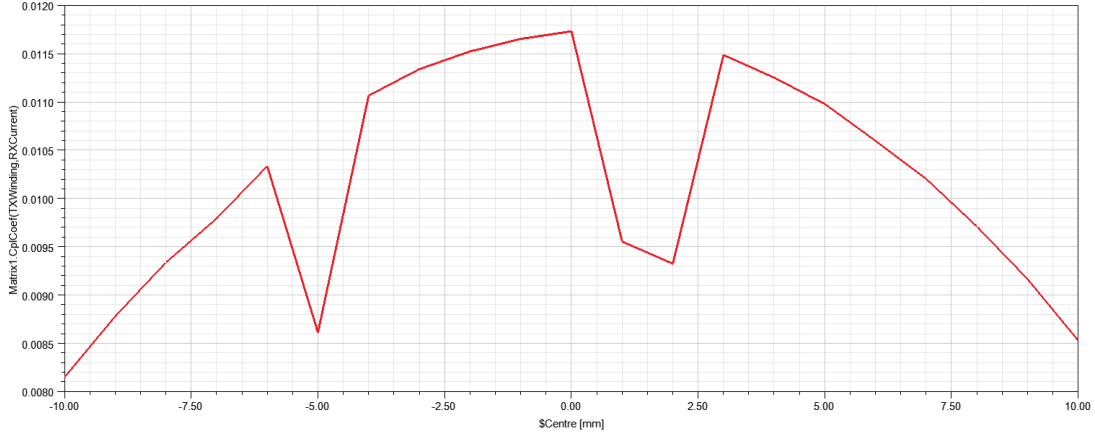


Figure 4.12: Figure depicting the results of the lateral misalignment test for the accepted [NFIC](#) link

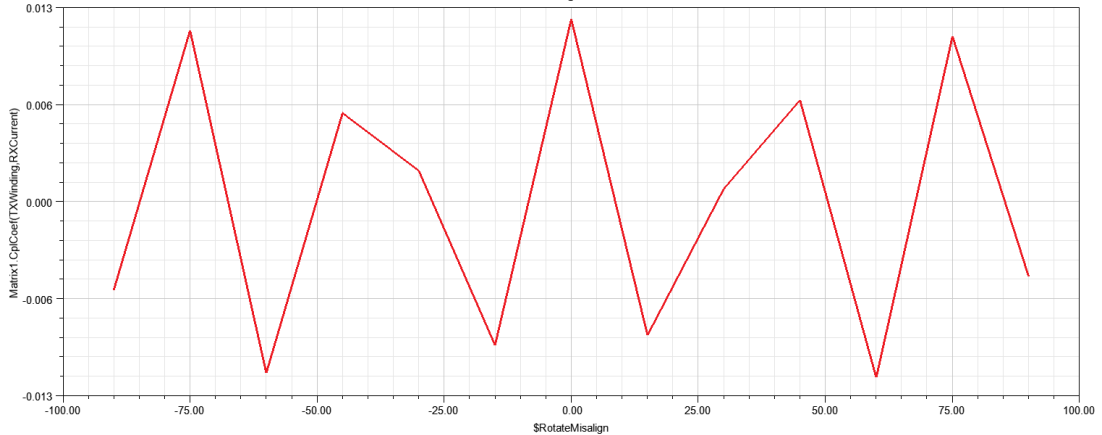


Figure 4.13: Figure depicting the results of the rotational misalignment test for the accepted [NFIC](#) link

Table 4.6: Table depicting coil nominal and misalignment coupling conditions obtained from Optogenetic [NFIC](#) link

Nominal Coupling	Worst case lateral Misalignment reduction (%)	Worst case rotational Misalignment reduction(%)
0.011730	26.68	24.98

The nominal coil coupling and misalignment characteristics fall within an acceptable range of the benchmark and thus fulfill the objectives of the coil link design. Before a transition to the receiver design could occur, the coils were manufactured and their properties experimentally validated. Details regarding the manufacture of these coils and the results of these validations are found in sections 5.2 and 5.3.1.

4.5 Receiver Circuit Design

The design of the receiver was divided into two sections. The first section involves designing the circuitry required to capture transferred power and drive the μ -LED. This aspect is guided by the theoretical framework discussed in chapter 3, with particular focus on sections 3.1.2, 3.2, and 3.5. The second component encompasses the design of the physical **PCB** inline with the constraints imposed by the manufacturing process.

The design process for the receiver circuit began by identifying the necessary stages to be included in the receiver. To formulate these stages, the objectives of the receiver electronics were defined as follows:

1. The circuit must drive the μ -LED at its nominal operating conditions.
2. The circuit should function based on the voltage supplied by the receiver coil.
3. The circuit should facilitate resonance and achieve maximum power transfer.

Figure 4.14 depicts a flowchart of the system implemented to meet these objectives.

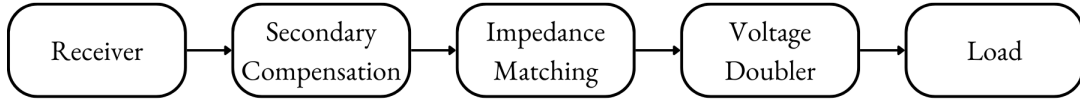


Figure 4.14: Flowchart depicting the receiver circuit structure

Implementing a voltage doubler addresses objectives 1 and 2, and is especially important due to the anticipated low induced voltage resulting from a loosely coupled **NFIC** link with a coupling coefficient of 0.011730, as described by equation 3.6. Additionally, the incorporation of secondary compensation and an **IM** network is aimed at fulfilling objective 3.

4.5.1 Secondary-side Compensation

The selection of a series capacitor for the secondary-side compensation was motivated by the theory outlined in section 3.2.1 in alignment with achieving a **S-S** resonant system. As noted, in Table 3.1, **S-S** networks are independent of variations of the load and coupling coefficient when operating at resonance. This is ideal given the small size of the receiver which is bound to result in misalignments thus varying the coupling. Moreover, as confirmed in section 4.4, the coupling coefficient of the **NFIC** is expectedly low and thus **S-S** is suitable as it has high efficiencies at lower coupling. **S-P** was deemed unsuitable given the fact that the power factor varies as a function of the mutual inductance which was not acceptable given the likely introduction of reactive losses and the inconsistent practical results obtained for the coil inductances and mutual inductance as outlined in section 5.3.2. Furthermore, it was identified that the resonant frequency was likely to change depending on coupling which would also serve to introduce reactive losses. Both **P-S** and **P-P** were ruled out given compensation dependency on both coupling and load variations.

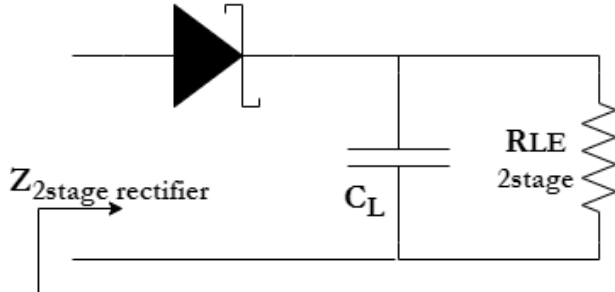
To determine an appropriate value for the series resonant capacitor, equation 3.7 was used with the selection of the resonant frequency as 13.56MHz . Notably, the simulated value of receiver inductance was not used in calculating the compensation capacitor value, rather the practical value of 940nH was

selected, midway between the estimated LCR value and the results of the [VNA](#) as depicted in section [5.3.1](#). This yielded a secondary capacitor value of 146.55pF .

4.5.2 Rectification Circuitry

Considering the load's dependency on [DC](#) voltage and the [NFIC](#) link supplying [AC](#) voltage, the introduction of a rectification stage before the load was necessary. As noted in section [2.5.4](#), the use of a voltage doubling circuit is a commonplace method of rectification which also serves to boost the low induced voltage at the receiver resulting from poor coupling. This is further emphasised in section [3.5](#), wherein the necessity for a voltage doubler is explained due to the inefficiencies arising at low power applications which occur as a result of the sub-optimal coupling highlighted in section [4.4](#). This poor coupling, inherent to the coil scale, requires the adoption of a voltage doubler to ensure the [μ-LED](#) receives the required nominal voltage. To further achieve rectification, the voltage doubler is complemented by a [DC](#) passing capacitor. The choice of a dual-stage voltage doubler in the scope of this project was further motivated by the anticipated low receiver voltage, outlined by equation [3.6](#), given the loose coupling.

To model the equivalent circuit of the voltage doubler such that the effect of its impedance on the load could be compensated for in the [IM](#) network, the voltage doubler's impedance was described by an equivalent simplified model:



$$Z_{diode} = R_s + \frac{1}{j\omega C_j} \quad (4.1)$$

$$Z_{2stagerectifier} = \frac{Z_{diode}}{n_{stages}} \quad (4.2)$$

$$R_{LE2stage} = \frac{R_{Load}}{2n_{stages}} \quad (4.3)$$

Figure 4.15: Figure depicting equivalent impedance of the voltage doubler and [μ-LED](#) seen from the receiver coil [9]

Where R_s is the series diode resistance and C_j is the diode junction capacitance. Furthermore, the impedance looking into the voltage doubler is given by equation [4.2](#) and the equivalent load impedance seen through the rectifier from the receiver coil is given by equation [4.3](#).

4.5.3 Impedance Matching

As described in subsection [3.2.2](#), the purpose of implementing an [IM](#) system is to transform the load impedance when viewed from the source. Guided by the theory of maximum power transfer identified in section [3.2.2](#), the load should appear to be the same resistance as that of the source itself. While chapter [2](#) delves into various [IM](#) techniques, there is an array of complexities that arise in many of these networks. Achieving optimally flexible [IM](#) is beyond the scope of this report, therefore an L-type network was selected for its suitable functionality in the given use case.

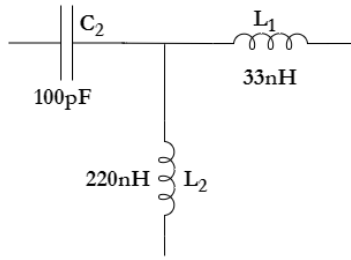


Figure 4.16: Figure depicting the L-type IM network

The inclusion of inductor L_1 serves to increase the IM network stability during voltage drops in the receiver by opposing these reductions in voltage, consequently creating an increase in current supplied to the load. Designing the IM network was a necessary undertaking due to the complex characteristics of the load's impedance. This complex loading arises from the significant junction capacitance effect introduced by the voltage doubling circuitry at high frequencies.

Although an analysis of the voltage doubler network's impedance was conducted, as outlined in section 4.5.2, validating the IM network's performance using the equivalent voltage doubler model proved challenging. In the literature discussed in chapter 2, it was noted that IM circuitry design and analysis are typically accomplished through Advanced Design System software rather than analytically. Unfortunately, this software was unavailable at the University of Cape Town.

As a result a 50Ω IM network, commonly found in the literature, was utilized. This choice influenced the selection of a 50Ω -rated receiver. It later became apparent that this decision presented challenges given that a suitable compensation capacitor for mitigating the inductance of the 15-turn receiver coil had been selected. This identified issue was anticipated to reduce the efficiency of power transfer from the source to the load, due to marginally incorrect matching, but would not render the circuit non-functional.

4.5.4 Final Receiver Circuit

The circuit schematic comprising the aforementioned modules is depicted in Figure 4.17.

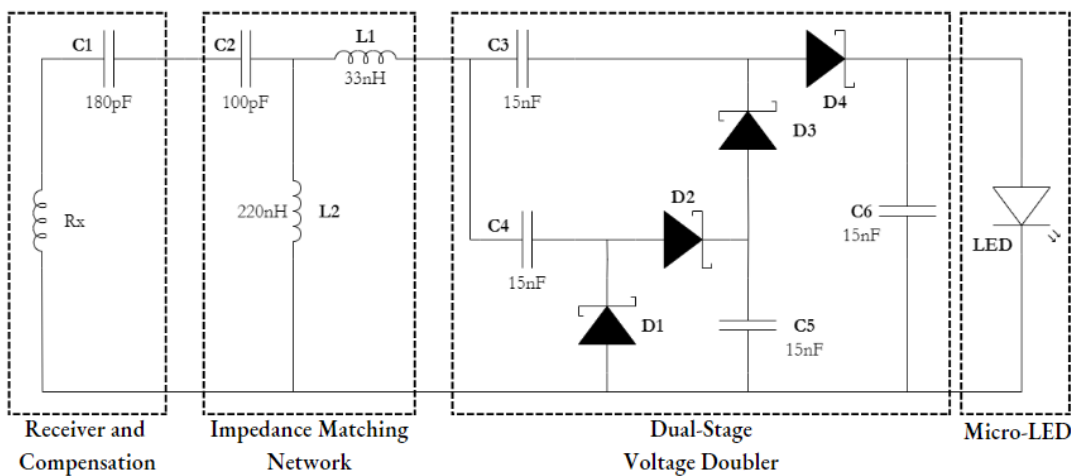


Figure 4.17: Figure depicting the receiver circuit

4.5.5 PCB Design

Manufacturer Constraints

The manufacturing process of the **PCB** posed a significant challenge. Prior to the design of the **PCB**, it needed to be determined whether a **PCB** outlined by the constraints of this project could feasibly be manufactured given the techniques used in the manufacturing processs and the tolerances thereof. Consequently, to begin designing the receiver **PCB**, attention once again needed to be drawn to the constraints and objectives outlined to guide the investigation into the manufacturers constraints. The **PCB** constraints and objectives are summarised below:

1. The **PCB** geometry should align with the state-of-the-art architecture, achieving dimensions within range of 2x3mm.
2. The **PCB** must adhere to bio-compatibility standards consistent with those observed in related architectures in the literature.

Given that the project timeline posed a significant challenge to project completion, particularly due to the potential bottleneck in manufacturing, initially the idea of opting for international **PCB** manufacturing was dismissed to avoid possible project delays. However, upon consulting with local manufacturers, it became evident that achieving the necessary board quality and specifications locally was not feasible. Subsequently, attention was turned to an international manufacturer.

Following extensive discussions with the manufacturer to assess the feasibility of board manufacture it was confirmed that production was possible, albeit with an estimated 5-week delay. Despite this potential delay, it was decided to proceed with international board manufacturing given the lack of an alternative. Subsequently, efforts were directed towards defining hardware constraints that align with the constraints specified by the manufacturer.

Table 4.7: Table depicting manufacturing capabilities for **PCBs** [75]

Manufacture Type	Layers	Thickness (mm)	PCB Panel Size (mm)	Delivery format	Minimum Package
Economic	2, 4, 6	0.8 - 1.6	10x10 - 250x250	Single, Panel with mouse-bites	0402
Standard	1-20	0.4 - 2	70x70 - 250x250	Single, Panel with V-cut/mouse-bites	0201

Manufacturing a board with the specified dimensions requires the use of 0201 components, requiring standard assembly and thus an increased manufacturing cost. Furthermore, multiple **PCBs** would have to be panelised on a single board given the minimum panel size being 10x10mm. The **PCBs** were panelised using mousebites instead of V-scoring due to the 0.4mm tolerance associated with V-scoring, which posed a risk of cutting into components on the board. A six-layer board was chosen to facilitate the use of reduced drill-hole sizing and vias on SMD pad services, to further minimize the **PCB** dimensions. The pad sizes and placements were carefully determined to accommodate 0201 components, ensuring a minimum clearance of 0.254mm between pads of opposite nets to prevent copper leakage. Furthermore, a minimum clearance of 0.3mm was established from the board's outline to any trace, inline with manufacturer requirements [76]. The available board material options included FR4, flexible substrate, and Rogers substrate [77]. While flexible substrate would have been ideal to meet the bio-compatibility objective, as will be discussed in section 4.5.5, bio-compatibility had to be compromised due to budget constraints.

Component Selection

Key component considerations revolve around the load, specifically the μ -LED, and the Schottky diodes employed in the voltage doubler. These components were chosen to be of 0201 SMD package type to align with the constrained board dimensions. Although smaller 01005 packages were considered, they were not feasible for assembly by the manufacturer. Notably, theoretically, the utilization of 01005 components would have allowed for even smaller dimensions of the PCB within the project's scope.

The specified requirements for the μ -LED are as follows:

1. The device must be an 0201 package.
2. Operating forward voltage drop in the range of 2.9-3.4V.
3. Operating current in the range of 20-25mA.
4. Power dissipation smaller than 100mW.
5. Wavelength of approximately 475nm.

The components selected for comparison are outlined in Table 4.8.

Table 4.8: Table depicting μ -LED comparison

LED Type	Dimensions (mm)	Forward Voltage (V)	Operating Current (mA)	Power Dissipation (mW)	Wavelength (nm)
APG0603VBC-A1-5MAV	0.65x0.35x0.2	3.2	5	16	468
IN-S21AT2B	0.65x0.38x0.36	3	2	6.2	468
LTST-FC03BD-5A	0.6x0.3x0.2	3.1	5	76	460 - 475
DA2432	0.32x0.24x0.15	3.1	25	40	475
XL-0201UBC	0.65x0.35x0.4	2.6 - 3.4	25	80	465 - 475
SML-LX0201USBC-TR	0.65x0.38x0.36	3.1	2	16	465

The Cree DA2432 was identified as the ideal selection for the load diode, meeting the specified requirements and having more compact package dimensions compared to other diodes. However, this diode was not selected due to its unavailability with the manufacturer. While these diodes could be sourced from Cree, the associated bottleneck in ordering from an alternate source to the manufacturer was regarded as unnecessary given the time constraints of the project and the availability of suitable alternatives. Furthermore, during this period, it was determined that a 2-sided assembly for the PCB would provide sufficient space for the μ -LED on the back of the PCB. As a result, the XL-0201UBC diode was chosen as it aligned with the geometric constraints and exhibits a suitable operating voltage and current range.

The selection of a suitable Schottky diode for the voltage doubler circuit required the consideration of various factors including the diode's switching speed, reverse recovery time, maximum operating frequency, reverse breakdown voltage, and junction capacitance. The specific requirements for the Schottky diode were as follows:

1. 0201 package size.
2. Capable of operating at 13.56MHz.
3. Parasitic impedance in the range of $C_p < 0.05pF$ and $L_s < 0.2nH$.

These specifications were established through a comparison with the Skyworks SMS7630-061 Schottky Diode, a component frequently cited in the literature. Notably, the availability of 0201 package Schottky diodes from the manufacturer was significantly constrained. The diodes considered are listed in Table 4.9 below:

Table 4.9: Table depicting Schottky Diode comparison

Diode Type	Dimensions (mm)	Breakdown Voltage (V)	Capacitance (pF)	Inductance (pH)	Frequency	Availability
BAT30F4	0.6x0.3x0.3	30	10	NA	NA	Available
SMS7630-061	0.6x0.226x0.273	min 1	0.2	0.2	< 26GHz	Unavailable

Due to the unsuitability of the BAT30F4 and the limited availability of alternatives, the decision was made to proceed with ordering the Skyworks SMS7630-061 diodes. Although this choice would introduce a 1-week backlog in PCB production, it was deemed the only viable option given the circumstances.

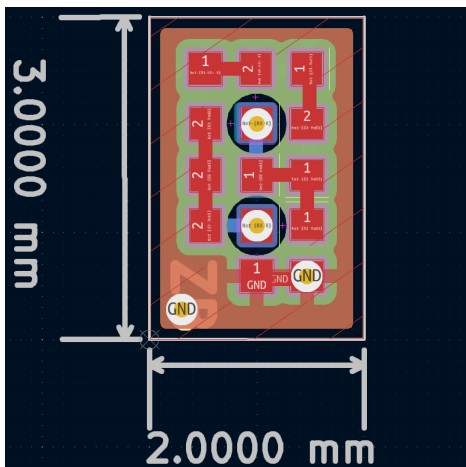
Design of Receiver Printed Circuit Board

The production of a 2x3mm PCB necessitated specific board characteristics, including trace widths, board layers, vias, and other parameters. Table 4.10 outlines the parameters that were specially adjusted for this production.

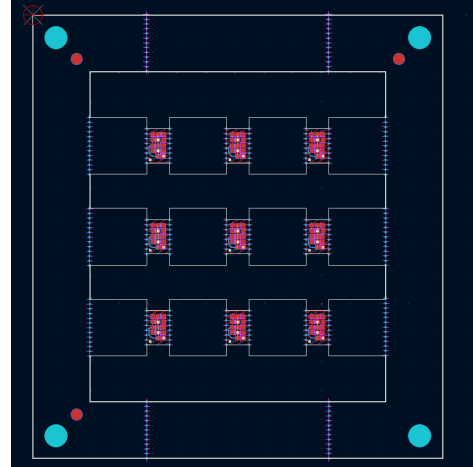
Table 4.10: Table depicting the selected PCB characteristics

Track Width (mm)	Via Size (mm)	Number of layers	Double-sided Assembly	PCB Material
0.127	0.3/0.15	6	Required	Flexible PCB

Accounting for these factors, the following PCB design was achieved depicted in Figure 4.18a.



(a) Figure depicting single Optogenetic receiver PCB in design tool



(b) Figure depicting panel of Optogenetic receiver PCBs in design tool

While confirmation was received that this PCB design was manufacturable, aligning with the project's objective of a 2x3mm PCB, the cost to manufacture this design exceeded the project's allocated budget. This prompted the initiation of a second design process. This subsequent design compromised on the original size and biocompatibility objectives to adhere to the financial restrictions imposed on the project.

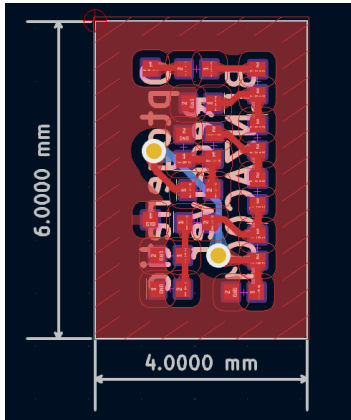
Upscaling the Printed Circuit Board

The production parameters for the second iteration of the board are highlighted in Table 4.11.

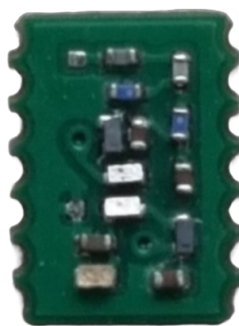
Table 4.11: Table depicting required PCB characteristics

Track Width (mm)	Via Size (mm)	Number of layers	Double-sided Assembly	PCB Material
0.127	0.35/0.3	4	Not Required	FR4

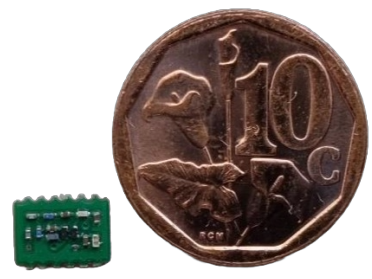
To stay within budget, some key changes were made. Dual-sided assembly was disregarded, and the PCBs were simplified to 4 layers, ruling out the option of SMD on pad placement and requiring slightly larger vias. This increased the board dimensions to 6x4mm. Moreover, compromises were necessary regarding bio-compatibility. The plan to use a flexible PCB was scrapped due to cost, and standard FR4 was used instead. The final board design is shown below:



(a) Figure depicting single scaled up Optogenetic receiver PCB in design tool



(b) Figure depicting close-up of manufactured Optogenetic receiver PCB



(c) Figure depicting physically manufactured Optogenetic receiver PCB alongside a 10 cent coin for scale

4.6 Transmitter Circuit Design

The hardware components required for the primary-side were identified in line with the limitations to access of pre-existing power electronics at the University of Cape Town. Inherently, power electronic devices including inverters and power amplifiers are expensive and fall far outside the budget allocated to this project. In addition to this, the project's short development time frame meant that any international orders were to be avoided. Therefore, prior to beginning a hardware selection process, an inquiry was made into the availability of an inverter which could function at megahertz operating frequencies. The only available inverter operated at a maximum of 200KHz. A UNI-T UTG2062B signal generator capable of operating within the megahertz frequency range was identified, however, and consequently this guided the decision to purchase a power amplifier that could couple to the signal generator and drive the transmitter coil through a series resonant network.

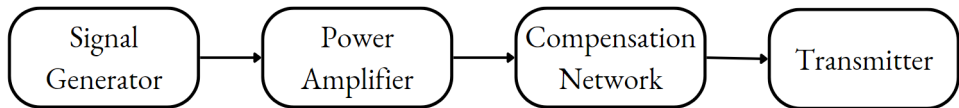


Figure 4.20: Flowchart depicting the primary-side circuit structure

4.6.1 Signal Generator

The selected use of a signal generator was guided by the absence of any suitable inverter at the University of Cape Town which could operate in the megahertz frequency range. The selected Signal Generator was UNI-T U2062B for its ability to drive up to $400mW$ of power and operate up to $60MHz$.

4.6.2 Power Amplifier Characterisation

Given the inherent poor efficiency of the **NFIC** coil link, as discussed in Section 4.4.3, primarily due to its geometry and loose coupling, it was imperative to ensure optimal efficiency on the primary side of the circuit. Therefore, the choice of a highly efficient power amplifier is of utmost importance as minimizing losses in this power amplifier, especially in low-power applications, is crucial.

In chapter 2, section 2.6, the Class E switching power amplifier was identified as an ideal architecture for driving **NFIC** links for **IMDs** due to its high efficiency. It is further worth noting that both Class D and Class E power amplifiers are well-suited for high frequency operation, offering the potential for achieving efficiencies exceeding 90%.

4.6.3 Board Requirements

In accordance with the system objectives, special attention was required to consider the power amplifier's capable operating frequency range. This was essential because the power amplifier needed to operate in the megahertz frequency range, which constrained the available hardware options. Furthermore, achieving precise resonance at exactly $13.56MHz$ for the practical implementation of the **NFIC** link and the compensation network was not guaranteed. This discrepancy was primarily due to practical coil implementations having slightly different inductance values compared to the simulations as identified in section 5.3.1.

Therefore, it was imperative that the power amplifier had a tunable operating frequency to accommodate these variations. Additionally, it was desirable for the power amplifier to have a wide operating voltage range to allow for adjustments in power provided to the transmitter coil, particularly in cases where the practical implementation might require more power than initially anticipated. A summary of the outlined board requirements is provided below:

1. Variable operating frequency range in excess of $13.56MHz$.
2. Able to operate at voltages in excess of $20V$.
3. Can deliver power up to $15W$.
4. Must be locally available.

The selection of the required operating voltage is governed by the poor coupling outlined in section 4.4.3, the necessity for a minimum voltage received at the receiver of 800mV and equation 3.6.

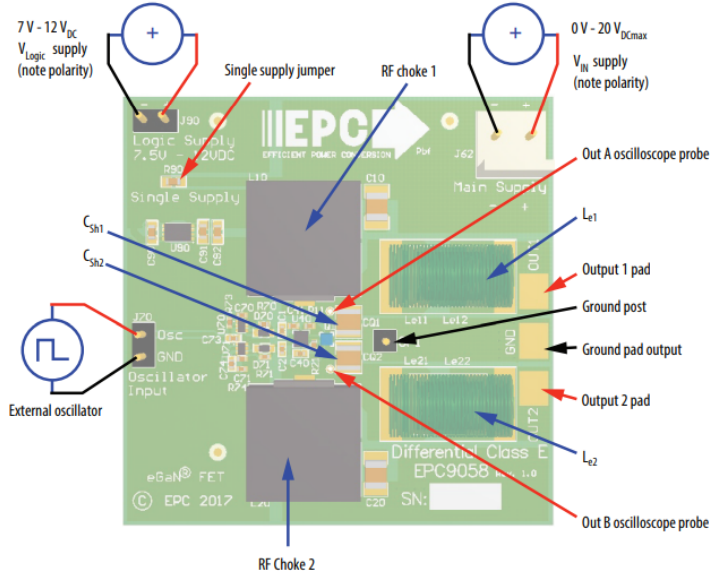
4.6.4 Available Hardware Options

Three power amplifiers were selected for comparison: the EPC9083, EPC9510 and the EPC9058. These amplifiers were selected due to their accessible cost, suitability to [WPT](#) as well as their design as development boards which mitigated the need for a full design of a power amplifier. Furthermore, these amplifiers are well documented.

Table 4.12: Table depicting maximum characteristics of power amplifier comparisons [78, 8, 10]

Power Amplifier	Class	Frequency (MHz)	V_{out} (V)	I_{out} (A)	Power Rating (W)
EPC9083	E	0 - 15	40	4	60 (rated)
EPC9510	D	6.78	66	0.8	50
EPC9058	E	0 - 15	20	2	40

EPC9083/EPC9058



EPC9510



Figure 4.22: Figure depicting EPC9510 Class D power amplifier [10]

The EPC9510 is a Class D power amplifier which achieves high efficiencies through [Zero Voltage Switching \(ZVS\)](#) [10]. The power amplifier is pre-tuned to an operating frequency of $6.78MHz \pm 678Hz$ via a preset onboard oscillator. [ZVS](#) is facilitated through an on-board pre-regulator, which is feedback controlled. The easily attainable [ZVS](#) characteristic of the EPC9510 makes it an attractive option though operating at $6.78MHz$ is non-ideal given the objective operating frequency of this project. Although it is possible to bypass the oscillator, it necessitates retuning the device for [ZVS](#) operation. Furthermore, the device's maximum operating frequency conditions are not clearly specified. The amplifier can handle a maximum supply voltage of $66V$, and its power consumption is capped at $10W$.

Device Selection

The decision to choose a Class E power amplifier over a Class D variant was based on the EPC9510's ambiguous operating frequency range and increased cost compared to the Class E power amplifiers. Both the EPC9058 and EPC9083 were suitable options, though the EPC9058 was selected due to wider availability.

4.6.5 Power Amplifier Tuning

The EPC9085 required tuning to operate at a frequency of $13.56MHz$. This involved the selection of additional components that needed to be soldered to the development board in the form of an RF choke, L_{RFck} , shunt capacitor, C_{sh} , and resonant network comprising an inductor and compensation capacitor. These additional parts are depicted in Figure 4.23:

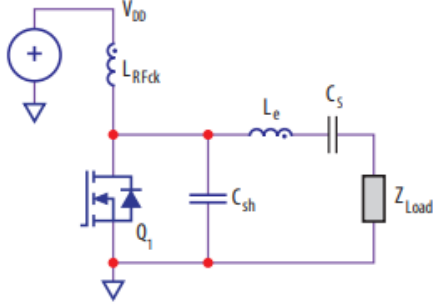


Figure 4.23: Figure depicting Class E Power Amplifier Circuit schematic [8]

$$\begin{aligned}
 1 \quad V_{DD} &= \sqrt{\frac{R_{Load} \cdot P_{Load} \cdot (\pi^2 + 4)}{8}} \\
 2 \quad L_e &= \frac{\pi \cdot (\pi^2 - 4) \cdot R_{Load}}{32 \cdot \pi \cdot f} \\
 3 \quad C_{OSSQ} + C_{sh} &= \frac{4}{\pi^2 \cdot (\pi^2 + 4) \cdot f \cdot R_{Load}} \\
 4 \quad C_{OSSQ} &= \frac{I}{V_{DD}} \cdot \int_0^{V_{DD}} C_{OSS}(V_{DS}) \cdot dV_{DS} \\
 5 \quad L_{RFck} &> \frac{(\pi^2 + 4) \cdot R_{Load}}{4 \cdot f} \\
 6 \quad \text{DC Block} \\
 7 \quad R_{Load}
 \end{aligned}$$

Figure 4.24: Figure depicting EPC9058 design equations [8]

Where R_{Load} represents the resistance resulting from the transmitter coil, accounting for the reflected impedance as detailed in section 3.4.1. Notably, the reactance of the transmitter is eliminated through resonance achieved by coupling with the compensation capacitor C_s . V_{DD} signifies the DC voltage that powers the switching circuitry. The specified expected power delivered to the load is 4W. C_{OSSQ} refers to the charge equivalent device output capacitance, which denotes the output capacitance of the FET within the power amplifier. It significantly influences losses and device switching speed, especially at high frequencies. The design components calculated using these formulae are depicted in Table 4.13. A compromise had to be made in sourcing some of the components as the Surface Mount Devices (SMD) sizes needed were in small supply locally, and given the time constraints, an additional international order could not be placed for the required components. Consequently, there is a slight deviation in the values of C_{sh} and L_e in Table 4.13.

Table 4.13: Table depicting design values calculated for the EPC9058 Class E power amplifier

Component	Design	Sourced
$L_{RFck}(\mu H)$	470	470
$C_{sh}(nF)$	5.46	10
$L_e(nH)$	5.21	6.67
$C_s(pF)$	8	8

4.6.6 Primary-side Compensation

Similarly to the selection of the secondary compensation capacitor, the selection of a series capacitor for primary-side compensation was guided by the theoretical framework expanded on in section 3.2.1, with the objective of establishing a S-S resonant system. Notably, the selected application of S-S compensation enables primary-side control of power transfer to the load, as explained in section 3.2.1 and depicted mathematically in sections 3.4.1 and 3.4.2. Considering this theory, it is evident that the output power delivered is directly proportional to the induced voltage in the secondary coil, which is equivalent to the voltage drop across the reflected impedance observed on the primary side. The

simulated value of transmitter inductance, which was confirmed by the practical value of $16.07\mu H$, was selected for calculation of the compensation capacitor. This yielded a primary capacitor value of $8pF$.

4.7 Summary of System Design and Simulation

The system design process began by formulating the essential system characteristics, which encompassed the choice of the **WPT** protocol, operating frequency, architecture structure, geometry, and the specifications and restrictions governing the **NFIC** coil link. In the scope of this project, a dual-coil **NFIC** protocol was chosen, operating at a frequency of $13.56MHz$, with a $10mm$ transfer distance to power a $2x3mm$ **PCB**.

Following this selection, the design and simulation of the power transfer coils was executed using Ansys Maxwell 3D **FEA** software. The design achieved a nominal coupling coefficient of 0.011730, with a misalignment tolerance that allowed for up to a 26.68% reduction under extreme misalignment conditions. Once the coil design was finalized, the receiver circuitry was developed, which included a compensation network, **IM** network, voltage doubler rectifier, and **μ -LED**.

With the receiver circuitry in place, the **PCB** layout was designed in compliance with the manufacturer's specifications. Two **PCB** designs were created: the first adhered to the $2x3mm$ size objective but proved to be too costly for manufacturing. The second design had dimensions of $6x4mm$ and fell within the budget, allowing for manufacture to commence.

Subsequently, attention was turned to the design of the primary circuitry required to drive the transmitter coil. The EPC9058 was selected and tuned to operate at a frequency of $13.56MHz$.

Chapter 5

Experiments and Results

Testing leads to failure, and failure leads to understanding.

—Burt Rutan

The system experimentation was structured into two main categories: simulation experiments and practical experiments. The simulated experiments aimed to evaluate the performance of specific submodules during the design phase and provided insights into the hardware's performance in scenarios that were impractical to test physically. The practical experiments focused on benchmarking the manufactured system's performance.

5.1 Simulation Experimentation

The following three simulated experiments analyse the system performance with regards to characteristics such as the magnetic field strength generated, the temperature variations caused by the coils, and the localized [SAR](#). The aim of these experiments is to assess the safety of the [NFIC](#) system in relation to the regulations outlined by the [ICNIRP](#).

5.1.1 Magnetic Field Strength

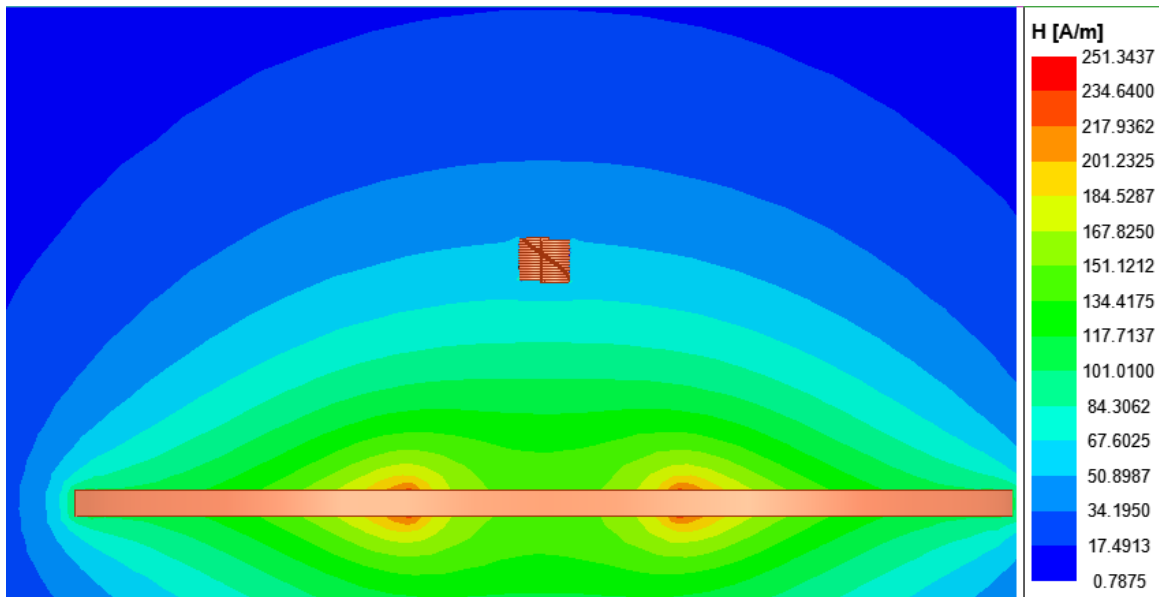


Figure 5.1: Figure depicting the magnetic field strength generated by the [NFIC](#) link

5.1.2 Temperature Variation

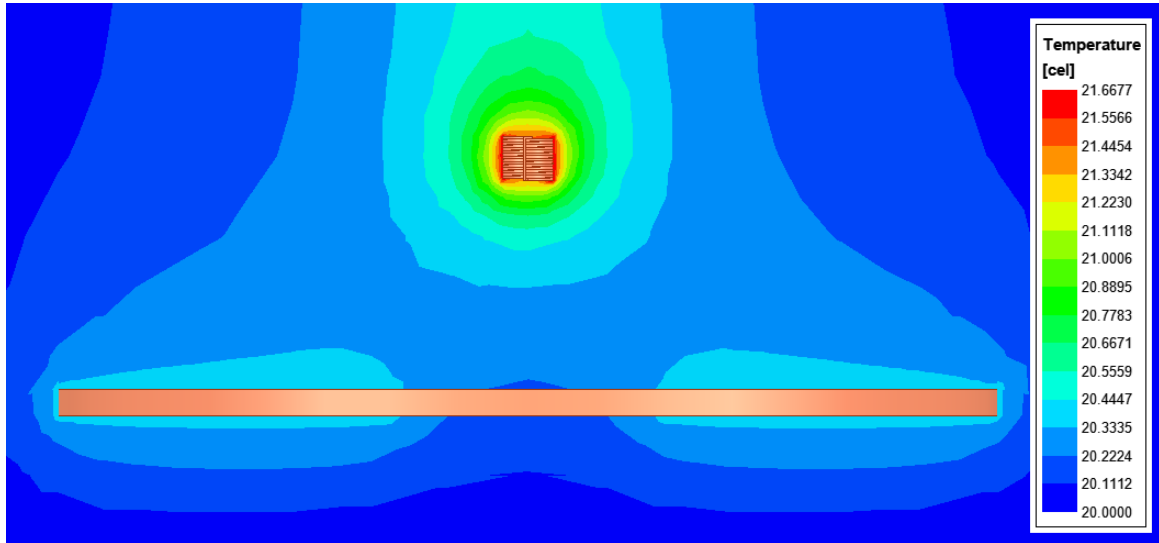
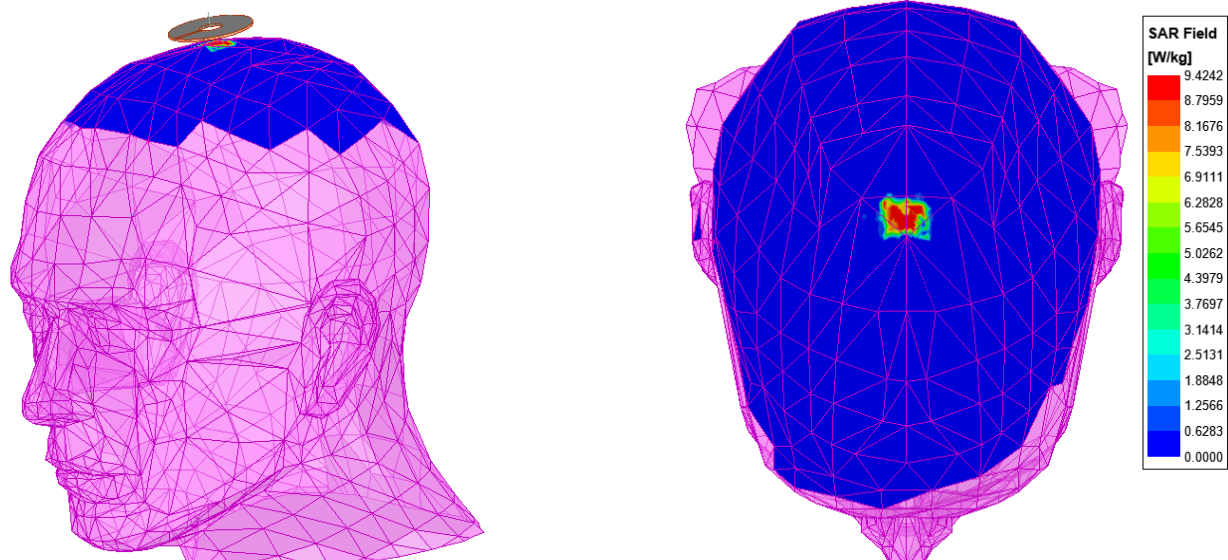


Figure 5.2: Figure depicting the temperature changes induced by the [NFIC](#) link

5.1.3 Specific Absorption Rate

Figure 5.3a illustrates the simulation configuration used for assessing the localized [SAR](#) when the system operates within the scope defined by this project. This entails powering the receiver coil, which is positioned between 5mm and 10mm inside the human head. Subsequently, Figure 5.3b presents the recorded [SAR](#) values on the part of the head closest to the transmitter.



(a) Figure depicting the simulated setup for [SAR](#) measurements

(b) Figure depicting the results of the [SAR](#) simulation

5.1.4 Near-Field Inductive Coupling Simulation Results Analysis

Figure 5.1 visually illustrates the magnetic field strength generated by the **NFIC** system in free space. When analyzing the data, the primary focus centers on the z-axis of the transmitter. This axis exhibits the highest field strength, which is of particular concern in terms of compliance with **ICNIRP** regulations as outlined in chapter 3, section 3.6. The data presented reveals that at a distance of $4.25mm$ above the transmitter, the field strength measures $117.71A/m$, gradually decreasing to $84.3A/m$ at $8.35mm$. Beyond $8.35mm$, entering the region where the receiver coil is positioned, the readings further decrease to $67.06A/m$.

The second parameter of interest relates to the temperature fluctuations in the surrounding tissue resulting from the operation of the **NFIC** link, as illustrated in Figure 5.2. Of specific concern is the temperature increase near the receiver coil, as it is the sole device intended for subcutaneous implantation and thus is responsible for any potential tissue damage. The figure shows that in the immediate vicinity of the coil, there is a maximum temperature increase of $1.67^{\circ}C$, which gradually decreases as it radiates outward, reaching less than a $1^{\circ}C$ increase at a distance of $1mm$.

The data presented in Figure 5.3b reveals that the highest localized **SAR** experienced by the head reaches $9.4242W/kg$. This peak **SAR** is concentrated along the central axis of the transmitter and decreases rapidly to $2.5131W/kg$ when moving radially outward within the transmitter's dimensions. Beyond the diameter of the transmitter, the **SAR** becomes negligible. Therefore, the area of interest for **SAR** values spans from $1.2566W/kg$ to $9.4242W/kg$ within a confined region of the head.

5.1.5 Near-Field Inductive Coupling Simulation Results Discussion

In accordance with the guidelines established by the **ICNIRP** as outlined in section 3.6, safety regulations mandate that exposure to magnetic field strengths should not exceed $80A/m$. While the magnetic field strength remains within acceptable limits at a distance of $10mm$ from the transmitter, measuring $67.60A/m$, the simulation raises a potential concern. Considering the transmitter's positioning relative to the head in the project's use case, it's possible that instances may occur where magnetic field strength exposures exceed the limits specified by the **ICNIRP**, as the head may at times be positioned between $4.25mm$ and $8.35mm$ from the transmitter.

Moreover, **ICNIRP** guidelines specify that temperature increases should remain within the range of $1-2^{\circ}C$, as discussed in section 3.6. Upon analyzing Figure 5.2, it becomes apparent that the simulation provides evidence of the **NFIC** link's safe temperature performance, with a maximum temperature increase of $1.67^{\circ}C$. Finally, as elaborated in section 3.6, **ICNIRP** sets a safe limit for localized **SAR** at $10W/kg$. The simulation results depicted in Figure 5.3b validate the compliance of the coil link designed for Optogenetic implementation with these safety regulations.

5.2 Physical System Implementation

Before conducting practical experiments, it was necessary to assemble the physical test system. This section outlines the assembly process commencing with the fabrication of the **NFIC** coils, followed by a discussion of the assembly of the **PCB** and primary circuit. Subsequently, a brief overview of the test rig's construction is provided.

5.2.1 Coil Manufacture

The fabrication of the **NFIC** transmitter and receiver coils followed the design specified in section 4.4.3. To achieve precise winding of the practical coils consistent with these simulations, a planar winding jig was constructed for the transmitter, and a bobbin with a suitable inner diameter was prepared for the receiver. The necessary coil properties are summarized in Table 5.1:

Table 5.1: Table depicting required practical coil parameters

Coil Type	Number of turns	Inner diameter (mm)	Pitch (mm)	Wire diameter (mm)
Solenoid (Receiver)	15	2.2	0.127	0.127
Circular Planar (Transmitter)	25	13	0.135	0.64516

While sourcing wire for the winding process, it became apparent that the University of Cape Town only had access to wire diameters of 0.1mm and 0.6mm , making it impractical to obtain exact wire sizes. Consequently, a slight deviation from the simulated inductance and coupling values was anticipated. After obtaining the wire, an iterative process began to construct a functional jig for winding the transmitter coil. The final design is illustrated in the Appendix, Figure ??, featuring a 3D printed round base and a 3mm laser-cut perspex disk securely fastened together using a nylon nut and bolt to avoid interference with the magnetic field. Special attention was given to the wire's angle of entry during winding and the tensioning method used to ensure a uniform planar coil given the inflexible properties of the copper wiring. A 2.2mm bobbin was sourced and the 15-turn receiver was wound and fastened using an adhesive given its fragility.

5.2.2 Transmitter Assembly

The assembly of the transmitter circuitry was a relatively straightforward process. The sourced **SMD** components were soldered onto the EPC9058 power amplifier. Afterward, the output of the power amplifier was linked to the transmitter coil via the primary compensation network. Finally, this assembly was connected to the UNI-T UTG2062B signal generator.

5.2.3 Receiver Assembly

The **PCBs** were manufactured without the addition of the receiver coil as this needed to be hand-wound and assembled upon arrival. An OMS2350 Zumax microscope was procured, and an attempt was made to manually solder the coils onto the **PCB**. The setup used in this initial attempt is illustrated in the Appendix, Figure A.17a. While it was acknowledged that this task was technically achievable given that a coil was successfully soldered down, it became evident that it required an extraordinary level of precision and skill to accomplish without causing any unintended damage. Any damages would be immensely difficult to perceive at this scale and therefore, given the pressing time constraints and the limited supply of expendable **PCBs** it was decided that a safer alternative was needed. The difficulty in assembly can be seen as an oversight in the design phase as the pads where the coil needed to be soldered could have been made significantly larger, considering the available space on the **PCB**, as shown in Figure 4.19a.

In light of the need for an alternative solution, the Nanotechnology lab within the Physics department at the University of Cape Town was approached for assistance. An MP4522 Ball Bonding machine was

identified as a potential solution to join the receiver coils to the **PCB**. However, it was not directly compatible with soldering the coils. Therefore, an adaptor board was designed to bridge the pads on the **PCB** intended for the receiver coil to a larger set of pads that could be easily soldered to. The equipment setup and the ball-bonded adaptor board, are depicted in the Appendix, Figures [A.17b](#) and [A.17c](#). The **PCB** with the receiver coil in Figure [5.4](#).



Figure 5.4: Figure depicting the **PCB** with attached receiver coil

5.2.4 Test Rig Assembly

A test rig was designed and 3D printed for the practical test procedures. This rig served the purpose of precisely positioning the receiver above the transmitter, maintaining a fixed separation of $10mm$. The design incorporated slots fixed at $1mm$ distances to accommodate measured misalignments. The test rig was designed to allow for the pre-wound receiver coil to be fastened down and **IMD** to be moveable by hand. An illustration of this test setup is provided in Figure [5.5](#) for reference.

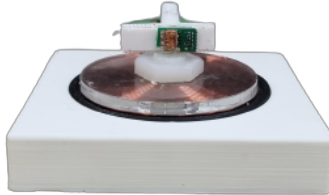


Figure 5.5: Figure depicting the test rig used to benchmark the system performance

5.3 Practical Experimentation

The process of practical experimentation served to benchmark the performance of the physically manufactured **NFIC** link and **IMD**.

5.3.1 Near-Field Inductive Coupling Simulation Performance Validation

The objective of validating the simulated **NFIC** link is to evaluate how closely the practical implementation of the coil system aligns with the final simulated design, particularly concerning the inductive properties of both the transmitter and receiver coils. The measurement of coil coupling is not included in this section and is addressed in section [5.3.2](#). The validation process operates on the assumption that the **FEA** software and **VNA** function according to the descriptions provided by Ansys and outlined by **Omicron**. Validating these tools goes beyond the scope of this project.

Receiver Validation Results

The data collected using the [VNA](#) regarding the receiver coil's inductance while coupled with the transmitter is illustrated in Figure 5.6. The peak point on the graph indicates the coil's resonant frequency and the corresponding inductance at this resonance.

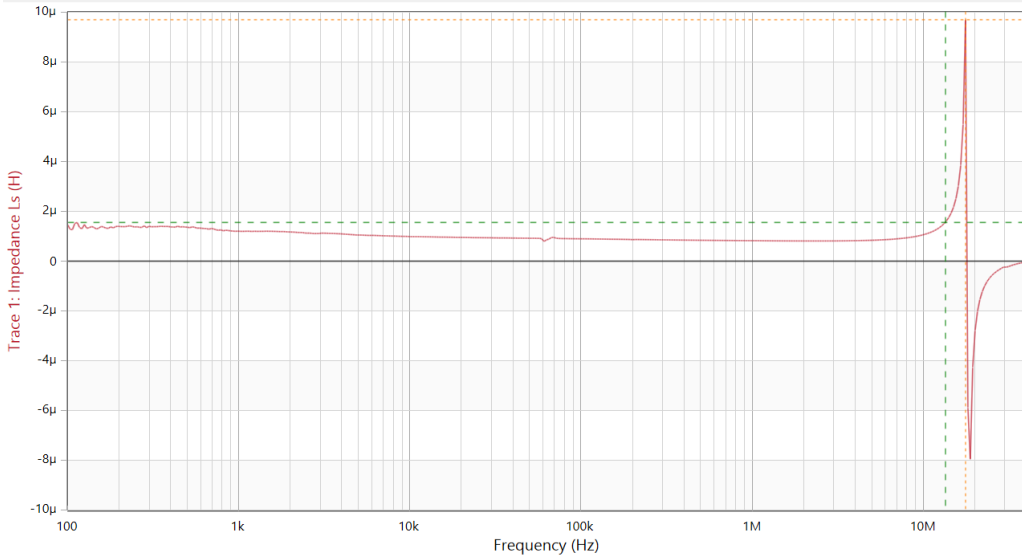


Figure 5.6: Figure depicting the receiver inductance results obtained from the [VNA](#)

At $13.56MHz$, the measured inductance was $1.55\mu H$, a substantial increase from the simulated value of $364.04nH$. The resistance was found to be 132.45Ω . While an increase in inductance at megahertz frequencies, as discussed in section 3.1.1, is expected and a further variation was anticipated due to wire sizing as noted in section 5.2.1 this drastic deviation from the simulation is unexpected since the simulation was conducted at $13.56MHz$.

Following this, an ISO-Tech LCR821 meter was used to verify whether the simulation or the [VNA](#) provided inaccurate inductance values. Notably, the ISO-Tech LCR821 meter was not the primary choice for measurement due to its limited frequency range, which only extends up to $200KHz$. Consequently, it could not provide a precise measurement of the coil's inductance at higher frequencies. The ISO-Tech LCR821 meter measured an inductance value of $240nH$, aligning more closely with the simulated $364.04nH$.

Receiver Validation Discussion

While an increase in inductance from $200KHz$ to $13.56MHz$ was expected, the results from Figure 5.6 indicated that this increase was no more than $700nH$. Therefore, the data gathered from the ISO-Tech LCR821 suggests that the inductance of the receiver is estimated to fall within the range of $240nH$ to $940nH$. This range represents a significant disparity from both the simulation and the [VNA](#) result of $1.55\mu H$. While this analysis may not perfectly indicate the receiver coil's inductance, it does offer an understanding of the coil's properties and suggests an inductance value within the estimated range from the simulation. This discrepancy can perhaps be attributed to the challenges inherent in operating at a small scale with imperfect geometry and a high frequency, highlighting a notable constraint within this project. Though this explanation was not accepted at face value, further investigation into this

discrepancy was conducted in section 5.3.1, yielding another suspected explanation.

Transmitter Validation Results

The data concerning the inductance and resistance of the transmitter coil, as obtained from the VNA, is presented in Figure 5.7. The peak of the graph signifies the resonant frequency of the coil and the corresponding inductance at that resonance frequency.

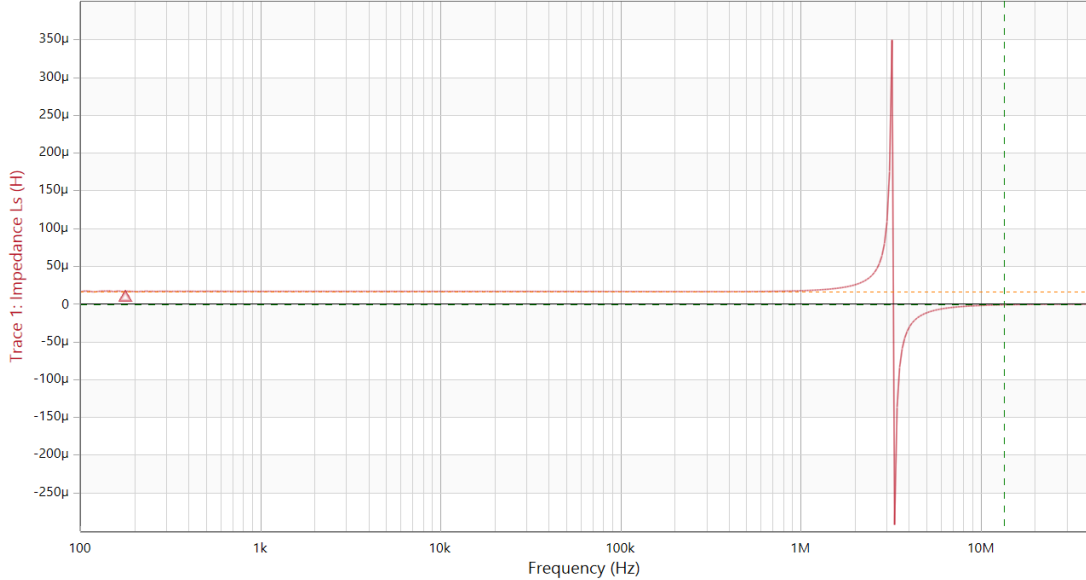


Figure 5.7: Figure depicting the transmitter inductance results obtained from the VNA

The inductance measured at $13.56MHz$ was $831.89nH$, significantly deviating from the anticipated value of $16.75\mu H$ obtained through simulation. To confirm the accuracy of this measurement, this measurement was crosschecked using the ISO-Tech LCR821 meter at $200KHz$ in the same manner as the receiver, which yielded an inductance measurement of $16.06\mu H$, aligning more closely with the simulated $16.75\mu H$. This deviation follows a pattern similar to that observed with the receiver coil.

Inductive Link Validation Discussion

In an attempt to further explain the variance between the practical implementation and the results of the simulation software, the frequency of operation within the simulations conducted in Ansys Maxwell 3D was swept up to $20MHz$ to determine how the FEA software responds to high frequencies. The results of this test are depicted in Figure A.18 in the Appendix. It was noted that little change occurred in the simulated receiver inductance value across the frequency spectrum indicating that the potential high frequency analysis offered by Ansys does not behave similarly to the practical response depicted in Figure 5.6.

5.3.2 Coupling Experiments

The following tests are conducted to compare the performance of the simulated coil system, as detailed in section 4.4.3, to its practical implementation. This comparison is based on its performance under nominal coupling conditions, as well as during lateral and rotational misalignments. The tests involve

positioning the coils at three different locations on the test rig and assessing the coupling at each of these positions. To ensure the accuracy of the results, each test is repeated six times at each location to account for any inaccuracies that may arise due to the small scale of the rig. The selected points of interest for placement of the receiver during the practical testing are $(0,0,10)mm$ as indicated in Figure 5.5, $(0, \pm 2.5, 10)mm$, and $(0, \pm 5, 10)mm$, along with the introduction of rotational misalignments at $\pm 45^\circ$ and $\pm 90^\circ$. Since coil coupling is not dependent on frequency, the available 200KHz ISO-Tech LCR821 meter was employed to carry out the coupling experiments. The setup of the coupling experiments is as follows:

- The receiver coil was positioned 10mm above the transmitter on the test rig.
- The transmitter was connected to the ISO-Tech LCR821, and its inductance was measured.
- The receiver was connected to the ISO-Tech LCR821, and its inductance was measured.
- Both the transmitter and receiver were connected to the ISO-Tech LCR821, ensuring that one terminal of each coil was connected, and the other was connected to the ISO-Tech LCR821. The inductance was measured.
- The coil terminals were then switched in the same configuration as the previous step.
- The difference between the two measured values was calculated and divided by 4 to yield the mutual inductance.
- The coil coupling is calculated using equation 3.4 with the mutual inductance and the inductances measured in steps one and two.

Experiment Limitations

Due to the small scale of the hardware and the corresponding need for exceedingly precise measurements regarding the relative positioning of the receiver in relation to the transmitter, it was expected that various imperfections related to spatial orientation and coil geometry would likely affect the coupling results. Firstly, the receiver coil was manufactured with great care; however, due to the wire's $0.1mm$ width, it was challenging to maintain a perfect shape. As a result, the actual receiver did not precisely match the simulation. Using a vernier caliper, it was determined that the coil's length deviated by up to $\pm 0.22mm$ from the expected $2mm$, and the coil's diameter exhibited some inconsistency across its 15 turns, with a maximum error of $\pm 0.4mm$.

Additionally, placing the receiver onto the test rig demanded the use of precision tweezers, and despite measurements being taken with a vernier caliper, it was estimated that inaccuracies occurred in the y and z axes, with deviations of maximum $\pm 1mm$.

Moreover, the ISO-Tech LCR821 used, whilst continuously calibrated throughout testing, could not maintain 100% consistent results due to the tolerance involved with the machine. Whilst in any ordinary scenario with normal coils, this machine tolerance would likely be negligible, the small scale of the receiver coil and its associated small inductance meant that the ISO-Tech LCR821 tolerance was non-negligible in the scope of measuring changes in inductance to deduce the coil coupling. Consequently, the coupling measurements were swayed by the LCR's tolerance.

Finally, the precision of the ISO-Tech LCR821 meter proved to be a considerable limiting factor. Although the ISO-Tech LCR821 meter could provide measurements in nano Henrys, to two decimal places, this level of precision often fell short because the changes in coil inductance were minimal, sometimes as low as $0.01nH$. Consequently, measurements could not be captured at $1mm$ intervals, as in the simulation, due to the impracticality and immense difficulty of accurately measuring changes in receiver inductance without using larger misalignment steps.

Experiment Results

The following figures illustrate the variations in coil coupling, averaged over the six tests conducted at each test point. Figure 5.8 depicts the averaged results obtained during the lateral misalignment tests, whilst Figure 5.9 illustrates the averaged results of the six tests for each rotational misalignment condition. The calculations used to determine the coil coupling make use of equation 3.4 as depicted in section 3.1.1.

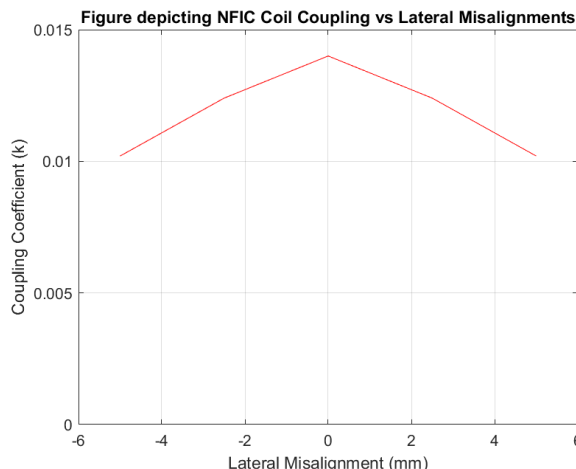


Figure 5.8: Figure depicting the results of the lateral misalignment tests

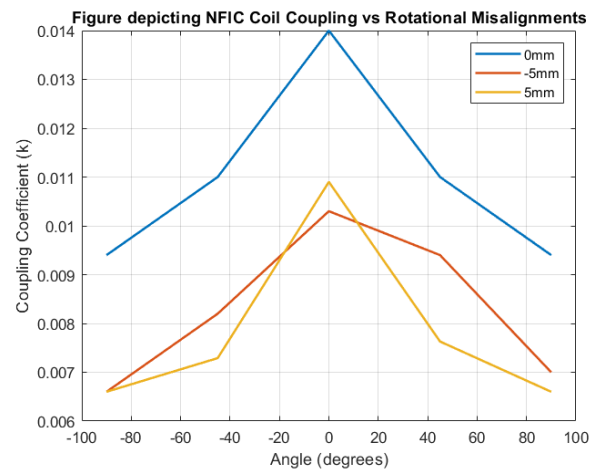


Figure 5.9: Figure depicting the results of the rotational misalignment tests

Results Analysis

As depicted in Figure 5.8, the practical coil coupling at nominal conditions was determined to be 0.014 with maximum reductions in coupling yielding 0.0102 at the extreme misalignment conditions. This is representative of a 27.14% reduction in coupling due to lateral misalignments at extreme conditions of $\pm 5mm$. The summarised reductions in coil coupling determined through rotational misalignments are depicted in Table 5.2.

Table 5.2: Table depicting rotational misalignment results

Lateral Misalignment (mm)	Worst case reduction due to rotational misalignment (%)
0	32.85
5	35.92
-5	39.44

Comparison to Simulation Results

In comparing the results obtained in section 5.3.2 with the results obtained in section 4.4.3 it is evident that the physical **NFIC** results closely resemble the expected link performance. The simulated performance of the coils identified a nominal coupling of 0.011730 with a worst case reduction to 0.0086 at the extreme misalignment condition of $5mm$ representing a 26.68% decrease in coupling. This is mirrored well by the practical nominal coupling of 0.014 with a worst case reduction to 0.0093, i.e. 33.56%. The slight variances in nominal coupling from the practical 0.014 to the simulated 0.011730 as well as the deviations in misalignment reductions can be accounted to the various non-idealities identified in section 5.3.2. Notably, there is a mild inconsistency that arises in the averaged values for the nominal coupling at the positive and negative extremes in the practical measurements. In comparing the coupling obtained at the right extreme during the lateral misalignment test to that of the coupling identified at the right extreme misalignment condition in the rotational misalignment test there is a variance of 0.0007 from 0.0102 to 0.0109 representing a tolerance in practical measurement of 6.42%. Likewise at the left extreme, an error of 0.0001. Notably, the practical variations in coupling were on average slightly larger than the simulated value.

5.4 Optogenetic Implant Benchmarking

The following section briefly details the benchmark tests conducted to validate the functionality of the Optogenetic **IMD**.

5.4.1 Voltage Doubler Performance

The voltage doubler performance assessment aimed to evaluate the efficiency of the voltage doubler under the conditions necessary to activate the **μ -LED**. This entailed measuring a minimum output voltage of $2.6V$ across the DC output capacitor. The **PCB** was connected to the UNI-T UTG2062B power supply for this purpose. An oscilloscope with fine-tipped probes was used to measure the output voltage while adjusting the input voltage to meet the turn-on voltage requirement. This test was performed on three separate **PCBs** to account for potential manufacturing errors, given the boards' scale, which might lead to unexpected faults in the board.

It was observed that at an input peak of $0.86V$, the output voltage measured $2.62V$. The anticipated output for this input was a $3.44V$. As a result, the voltage doubler demonstrated an efficiency of 76%.

Experiment Limitations

Measuring the output voltage across the DC-passing capacitor posed a significant challenge due to the scale of the hardware. Moreover, the high-frequency operational characteristics further complicated establishing a reliable measurement connection to the board. As a result, there was noticeable variability in the measured results, necessitating the sampling and averaging of data over a period of time.

5.4.2 Illumination Characteristics

The following test aimed to characterize the illumination behavior of the **μ -LED** under varying input powers. The test configuration involved direct connection of the assembled **IMD** to the UNI-T

UTG2062B Function Generator, providing an input voltage across the receiver coil terminals capable of driving up to $400mW$. The system was initially powered with voltages ranging from $1.4Vpp$ to $2Vpp$, considering the expected fourfold output scaling by the dual-stage voltage doubler. In the absence of any illumination, the voltage was gradually increased, reaching up to $2.6Vpp$ to account for potential losses previously observed in the voltage doubler. This testing was performed on three PCBs, with none illuminating.

5.4.3 Illumination Characteristics Results Discussion

The complete absence of any visible illumination indicated a potential manufacturing error. Given the device's small scale, the Nanotechnology lab was revisited to enable visual inspection of component placements on the board, as illustrated in Figure 5.10. The Schottky diodes, marked by their black color and cathode indicators, were verified to be correctly positioned. However, visually confirming the accurate placement of the μ -LED, circled in red, proved challenging.

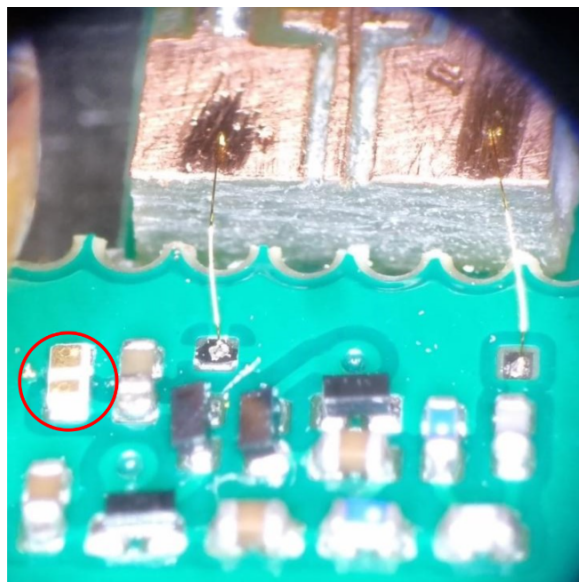


Figure 5.10: Figure depicting the board inspection under the MP4522 Ball bonding machine

An effort was made to confirm the polarity of the μ -LED using fine-tipped test probes available in the lab and a multimeter. The diode was successfully illuminated when tested in the expected reverse polarity of that of its intended operation in the circuit. This test indicated an assembly error on the part of the manufacturers.

5.4.4 Impedance Analysis

To assess the effectiveness of the IM network on the PCB, the full IMD was connected to the UNI-T UTG2062B Function Generator and powered at $13.56MHz$. It was noted that at this frequency, the reactance of the compensation capacitor would nullify the reactance of the inductor as explained in section 3.1.2. As a result, the resistance of the load seen by the coil was solely the real resistance due to the IM network. Table 5.3 depicts the measured characteristics:

Table 5.3: Table depicting the resistance measured at varying input conditions

Voltage (Vpp)	Current Drawn (mA)	Resistance (Ω)
0.8	22	36.36
1	24	38.46
1.2	26	46.15

Experiment Limitations

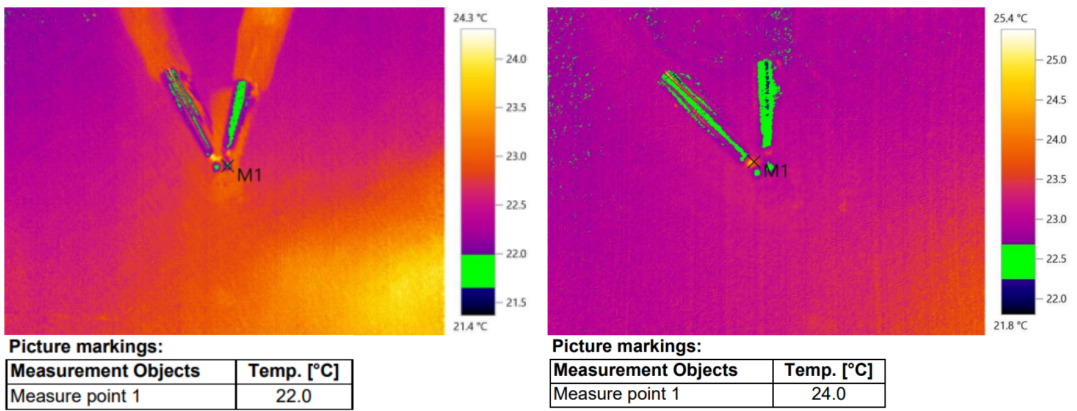
Establishing a reliable connection with the board using large probes presented challenges, resulting in notable instability in the measured current values. To mitigate this instability, it again became necessary to record the current over time and calculate averages. Additionally, while using a **VNA** is typically the preferred method for impedance measurements, it was not feasible in this case due to the absence of an SMA or BNC connector on the **PCB**. This can be attributed to an initial design oversight.

5.4.5 Impedance Analysis Results

The anticipated impedance of the matched network was 50Ω . Although the practically measured impedance exhibited some variation, the measurements closely approached 50Ω . Notably, the measurement was closest to the expected value when an input of $2.4Vpp$ was provided to the **PCB**, resulting in a current flow of $26mA$. This indicated an impedance of approximately 46.15Ω , suggesting that the **IM** was in proximity to the expected design value.

5.4.6 Temperature Benchmark

Figure 5.11 illustrates the results captured using the EN 13187 thermal imager. The receiver coil on the **PCB** was, again, powered at $13.56MHz$ using the UNI-T UTG2062B to ensure controlled input conditions. Consequently, the large green isotherms above the two squares represent the input probes, while the coil is positioned above the two squares which signify the copper pads. The left figure illustrates the temperature of the **IMD** coil when unpowered, whereas the right figure illustrates the temperature of the **IMD** after being powered for 5 minutes with an input of $1.72Vpp$, simulating the required voltage at the receiver to activate the μ -LED.

Figure 5.11: Figure depicting the **IMD** temperature variance

5.4.7 Temperature Benchmark Discussion

The results reveal a 2°C temperature rise in the coil. This practical outcome demonstrates a slight temperature increase compared to the simulation, which showed a 1.67°C temperature rise. Nevertheless, this outcome remains in close alignment with the regulations specified by the [ICNIRP](#).

5.5 Wireless Power Transfer Test

The objective of the following test is to evaluate the efficacy of the full [WPT](#) Optogenetic system. The tests were conducted at an operating frequency of 200KHz using the available Wolfspeed inverter, bypassing the power amplifier. This approach was chosen to eliminate potential non-idealities stemming from the power amplifier, as there was limited time available for debugging it. To account for the reduced frequency, a new calculation for the primary compensation capacitor was determined. Notably, the compensation for the [IMD](#) could not be adjusted due to its size, resulting in a partially compensated system.

While this testing scenario is not entirely ideal for the [IMD](#) designed within the scope of this project, as the [IMD](#) incorporates both compensation and [IM](#) in the secondary, it was still valuable to conduct these tests. This is because similar systems in the literature, such as the system developed by Bansal et al., which was used as a benchmark, were entirely uncompensated on the secondary side [11].

5.5.1 Full System Experimentation

The [IMD](#) was setup in the test rig under nominal conditions, with the receiver coil connected to the Yokogawa PX8000 power scope. The transmitter's voltage was adjusted until a sufficient voltage across the receiver terminals was achieved to ensure the operation of the $\mu\text{-LED}$. A voltage of 50V was applied to the transmitter, drawing a current of 210mA , thus resulting in a power dissipation of 11.55W in the primary. The received waveform is depicted in Figure 5.12.

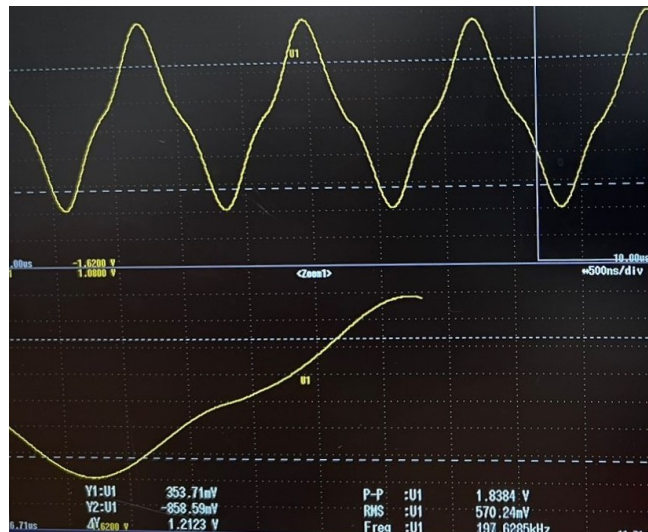


Figure 5.12: Figure depicting voltage waveform measured at the receiver of the [IMD](#)

Results Analysis

The measured peak received voltage was $0.92V$, which was found to be adequate for the proper operation of the μ -LED, as discussed in section 5.4.1. The current observed across the PCB when the peak input voltage was $0.92V$ fell within range of $25mA$. Consequently, taking into account the efficiency of the voltage doubler determined in section 5.4.1, the power supplied to the μ -LED was calculated to be $70mW$, resulting in a PTE of 6.84%.

5.5.2 Full System Implementation Discussion

Evidently, this testing procedure is limiting in providing holistic insight into the functionality of the full system in meeting the intended system objectives. Nevertheless, due to time constraints, it represents the most practical approach available for benchmarking that could be pursued.

The primary limitation arises from the reduction in the operating frequency to $200KHz$. This frequency reduction leads to an incorrect configuration of the compensation network, resulting in suboptimal PTE. Furthermore, the decrease in frequency significantly lowers the inductor's resistance, which was measured at $135.10m\Omega$ using the ISO-Tech LCR821 meter. Consequently, the system's IM is also incorrect at this frequency.

Despite these non-optimal conditions, it was observed that the system could still provide the necessary voltage to operate the μ -LED, indicating a higher likelihood of success at the correct operating frequency with a greater PTE.

5.5.3 Comparison to Similar Implementations

The full system benchmark depicted a PTE of 6.84% with a voltage induced at the receiver of $920mVpp$ and a coupling of 0.014.

Biswas et al. [37] developed a planar spiral two-coil system operating at $7.15MHz$. Their system demonstrated effective operation over a distance of $5mm$, with the implemented IMD having an area of $67.52mm^2$, which is approximately 2.8 times larger than the IMD implemented in this project. In their setup, a voltage of $500mVpp$ was induced in the receiver over half the distance of this implementation. Notably, their design did not incorporate a voltage doubler rectifier, resulting in the delivery of a DC voltage of $200mVpp$ to the load and a lower PTE of 4.1%. Hence, the system implemented in this paper outperforms this system.

Wu et al. [4] designed a two-coil system utilizing PSCs, which achieved a comparable coupling coefficient of 0.015 and a higher PTE of 9.2% while operating over a distance of $12.5mm$. Their system exhibited superior performance compared to the one presented in this work. Notably, their system differed by undergoing a far more extensive coil optimization process.

Chapter 6

Conclusions

From error to error, one discovers the entire truth.

—Sigmund Freud

6.1 Report Summary

The principal goal of this project was to create a [WPT](#) protocol designed to power an Optogenetic implant. This overarching objective included several critical components, such as designing and practically implementing an [NFIC](#) coil link, incorporating power electronics principles to improve [PTE](#), and producing an [IMD](#) of a size similar to contemporary devices.

This report commenced in chapter 2 with an extensive review of the relevant literature pertaining to the field of [WPT](#) for Optogenetic [IMDs](#). The literature review began by providing an overview of neuromodulation in medicine and the introduction of [IMDs](#) within this domain. It then delved into the implementation of Optogenetics, emphasizing the imperative role of [IMDs](#) and the adoption of [WPT](#) in this context. The discussion proceeded with an exploration of various [WPT](#) methods in the field of Biomedics, along with an in-depth review of the Biomedical applications of [NFIC](#). This review encompassed diverse coil systems and methods for regulating power transfer. The subsequent section delved into the hardware characteristics of existing [IMDs](#), including considerations related to form factors, mechanical aspects, bio-compatibility, and commonly used circuitry. Chapter 2 concluded by addressing key circuit considerations pertaining to the primary before presenting a concise summary of the relevant literature in Table 2.3.

The knowledge acquired in chapter 2 was built upon in chapter 3 by an analysis of the pertinent theoretical concepts essential for implementing high frequency [NFIC](#) in Biomedical applications. This chapter commenced with the specific theory underpinning [NFIC](#) and the electrical properties inherent to inductive links. These properties included aspects such as coil coupling, inductance, and high frequency losses. Subsequently, the chapter delved into the topics of resonance and compensation, examining various types of compensation methods, including capacitor and [IM](#) networks. This was followed by a concise discussion on power amplifier operation, followed by the provision of the mathematical foundation for [NFIC](#) equivalent circuit theory. The subject of rectification was then addressed, and the chapter concluded with a brief discussion regarding the safety frameworks provided by the [ICNIRP](#).

The report continued in chapter 4 with the main implementation of the project including both the design and simulation of the [NFIC](#) coil system, the Optogenetic receiver [PCB](#) and the primary circuitry.

The design process began by outlining the foundational characteristics of the **WPT** Optogenetic system architecture consisting of the **WPT** framework, operating frequency and structure of the **WPT** link before laying out the full system structure. The chapter then streamlined the focus onto the simulation design of the **NFIC** coil link in Ansys **FEA** simulation software. The results of the simulation were validated through the use of an **LCR** and the **Bode 100 VNA** before moving onto the design of the receiver circuitry.

The design of the receiver circuitry entailed identifying the submodules to be incorporated in the receiver. These submodules included a capacitor compensation network, **IM** network, a dual-stage voltage doubler and a μ -LED as the driven load. A **S-S** compensation network was selected for primary and secondary compensation given its load and coupling independence as well as high efficiency characteristics with loose coupling. As noted, the rectification stage featured a dual-stage voltage doubler, for which a complex analysis was conducted to establish an equivalent model to be used in the design of **IM** circuitry. Subsequently, an L-type **IM** network was designed and implemented, with the understanding that such network analyses are typically executed using Advanced Design Simulation software, and thus the design ensured alignment with existing literature. Once the relevant submodules had been designed, the full circuit was ready to be implemented on a **PCB**.

Section 4.5.5 discussed the design of the implantable **PCB** inline with the constraints imposed by the manufacturing process. The section began by outlining the manufacturer constraints, followed by the component selection for the **PCB**. With the components selected, the board characteristics necessary to achieve the design were highlighted and the design of a $2 \times 3\text{mm}$ board was completed. Following the realisation that this **PCB** fell outside of the budget allocated for the project, a second **PCB** was designed which compromised on the size constraint and necessity for bio-compatibility of the board, yielding a $6 \times 4\text{mm}$ FR4 **PCB**. Once the **PCB** design was complete, the design process began for the primary circuit. The limitations on available hardware for high frequency operation were noted in conjunction with the limited budget before it was decided that the transmitter would be driven by a Class E power amplifier and **RF** signal generator. The UNI-T UTG2062B signal generator was identified for use and the EPC9058 was identified as a suitable power amplifier. Following the purchase of this amplifier, a design process commenced to tune the amplifier to operate at 13.56MHz . The primary-side compensation was designed inline with the tuning process of the amplifier, maintaining the **S-S** compensation network as defined in the scope of this project. Following the completion of all submodules, the system was implemented in practice wherein the coils were wound and attached to the primary and secondary and a test rig was setup for benchmarking.

Following the completion and physical implementation of the system design in chapter 4, the report detailed the evaluation and discussion of the system's performance in chapter 5. Both simulated and practical experiments were conducted in order to benchmark the system. The initial set of simulated experiments aimed to gauge the **NFIC** system's safety and compliance with the regulations stipulated by the **ICNIRP**. Parameters such as the magnetic field strength, coil temperature variations, and **SAR** were analysed. The magnetic field strength analysis revealed a marginal deviation from regulations, with the coil link slightly exceeding the permissible limit. At a distance of 8.35mm from the transmitter a magnetic field strength of 84.3A/m was recorded, signifying a potential safety concern if the transmitter is situated within 8.35mm of the head. Contrastingly, the examination of the temperature variation

resulting from the coil link revealed a temperature increase of 1.67°C , which falls well within the acceptable regulatory limits. Furthermore, the **SAR** was assessed and determined to be 9.42W/kg , which was also compliant with the established regulations.

Following the safety testing of the system, a practical validation process was carried out to confirm the electrical characteristics of the coil design predicted by the **FEA** simulation software. This involved validating the inductances of the coils to ensure they matched the simulated values. The results revealed a substantial disparity in practical and simulated coil inductances at high frequencies, whereas at lower frequencies, the practical and simulated values showed better alignment. To investigate this further, a test was conducted to assess the performance of the **FEA** simulation software at high frequencies. The findings indicated that the simulated high frequency performance did not align with expected practical performance.

The practical coil coupling was subsequently compared to the simulated performance, showing a close correlation in the results. The practical nominal coupling was measured at 0.014, with a maximum reduction occurring during lateral misalignments of 27.14%. Furthermore, when positioned directly above the transmitter, the maximum reduction due to rotational misalignments was 32.85%. As the lateral misalignments increased to $\pm 5\text{mm}$, the reductions due to rotational misalignments reached 35.92% and 39.44%.

The functionality of the manufactured Optogenetic **IMD** was then evaluated. It was confirmed that the voltage doubler and **IM** network were operational, exhibiting an efficiency of 76% and 46.15Ω matching at operating conditions. However, the performance of the **PCBs** were marginally inconsistent, primarily attributed to manufacturing faults and issues with testing at this scale. Notably, an issue with the polarity of the $\mu\text{-LED}$ was identified, which prevented the assessment of the illumination characteristics of the **IMD**. Finally, the full system was benchmarked, operating at a lower frequency due to inefficiencies in the power amplifier which, given the time constraints, could not be solved. At 200KHz , the **NFIC** Optogenetic system delivered 70mW of power to the load yielding a system efficiency of 6.84%.

6.2 Conclusion

While the project did not fully achieve all its objectives, particularly in terms of an optimal high frequency implementation and the creation of a holistically functional Optogenetic **IMD**, it represents significant progress in developing a working **NFIC** coil link and successfully manufacturing such an **IMD**. The resulting device, with dimensions of $6\times 4\text{mm}$, is comparable to state-of-the-art devices and features functional modules, except for a minor manufacturing fault. In this context, the project can be considered a considerable success. The physical **NFIC** system achieved results that matched or even exceeded those from simulations, laying the groundwork for future developments in coil structures and geometries. Furthermore, it is worth noting that the hardware manufacturing process pushed the boundaries of contemporary manufacturing practices and testing methodologies. In doing so, certain shortcomings in the design of the **IMD** and the testing procedures implemented were revealed, offering valuable insights for future research endeavors. Thus, the culmination of this work can be seen as a worthwhile contribution to the field of research in **IMDs** for Optogenetic neuromodulation.

Chapter 7

Recommendations and Future Work

Our greatest weakness lies in giving up. The most certain way to succeed is always to try just one more time.

—Thomas A. Edison

In light of this project's completion, there are various lessons that should be carried forward regarding the implementation of this design. These regard the physical manufacture of the [PCB](#) and the testing procedures implemented.

7.0.1 Board Manufacture

While minimizing the size of the [IMD](#) was a fundamental goal driving this project, it is not practical to directly transition to the manufacture of a [PCB](#) at the achieved dimensions. The nature of prototyping devices is essential to reaching a final functional design. However, due to time constraints in this project, the design process could not include iterations of [PCB](#) manufacturing and thus a prototype of the [PCB](#) on a larger scale could not be achieved before scaling it down without compromising the project's core objectives.

Nonetheless, for testing purposes, it is recommended that some compromises on the geometric constraints of the [IMD](#) are made. For instance, it may be beneficial to aim for a larger [PCB](#) size, aligning with dimensions found in some literature at around 250mm^2 . Additionally, implementing test points on the [PCB](#) would significantly enhance the ability to benchmark its performance accurately. Furthermore, due to safety considerations when operating at high frequencies, the [PCB](#) could not be probed by hand while wirelessly powered. The [PCB](#) needed to be pre-rigged to measurement devices, which posed a significant challenge due to the lack of test points, the sheer size of the [PCB](#), and the probe size and weight of the test equipment. In addition to test points, integrating SMA connectors into the board design would allow for more comprehensive testing using a [VNA](#).

7.0.2 Test Hardware

Working at higher frequencies presented challenges due to the somewhat unpredictable behavior of the coils at these elevated frequencies and the increased demands on power electronics. While this is not an insurmountable limitation, it highlights the need for more strategic planning when acquiring testing hardware, including an appropriate [VNA](#) and higher-precision equipment. The precision required to measure inductances, resistances, voltages and current characteristics of the small-scale receiver coils revealed a consistent shortfall in the tolerances of the available testing equipment.

7.0.3 Receiver Coil Attachment

Considering the cost of manufacturing the boards and the resulting limitation on the number that can be produced, manually assembling the receiver coils is a risky undertaking. Unfortunately, achieving the dimensions outlined in this project makes it an unavoidable step. Therefore, it's crucial to acknowledge the need for skills training to prepare for soldering the boards and, furthermore, the early sourcing of required equipment such as a microscope and fine-tip soldering iron. Additionally, it is crucially important to maximise the size of the receiver coil pads on the [PCB](#) design. A significant oversight in the [PCB](#) design was creating pads that were only slightly larger than the 0201 component pad sizes.

While there are valuable lessons to be learned to avoid repeating certain mistakes, there is also a wealth of knowledge and experience to build upon from this particular implementation.

7.0.4 Tissue Environment Design Process and Benchmarking

Testing the coil link within a tissue environment was not feasible due to time constraints, although it is recognized as a significant factor affecting system performance, as discussed in chapter [2](#). Section [2.4.1](#) highlighted the variations in coupling caused by changes in dielectric properties. A future recommendation for projects extending this research is to implement a design optimization process involving comprehensive tissue modeling using [FEA](#) software. This approach can be complemented by practical testing with phantom tissue models to evaluate the link's performance in the given use case.

7.0.5 Multi-coil/Novel Geometry Implementation

As covered in chapter [2](#), an array of three, four and novel coil architectures exist that serve to optimise the coupling of the system. While these systems add complexity to the scope of the project, they are a clear addition that can be made to further the research in this topic. An attempt was made at a novel coil implementation, though a more extended coil design process is likely to yield better results in new geometries.

7.0.6 Misalignment Tuning

Considering additions noted as above, section [2.4.4](#) further discusses an array of closed-loop systems implemented to tune the device operation to increase robustness to variances in the load, misalignments and separation. The [IMD](#) complexity could be increased to account for a closed-loop system for monitoring and tuning.

7.0.7 Benchmarking Reflections of Power Electronics Systems

A significant portion of the system's impedance and power reflection characteristics could not be effectively benchmarked given the time constraints and certain identified design oversights. Future projects should account for these test procedures through the use of a [VNA](#).

7.0.8 Optimisation of Testing Procedures

As highlighted in chapter [5](#), significant limitations stemming from the scale of the hardware and the precision required for testing were encountered. It is worth noting that the development of test

procedures demands as much attention, if not more, than the design of the [NFIC](#) link and [IMD PCB](#). This is due to various challenges related to the size and weight of testing probes compared to the [IMD](#), the tolerances of the testing equipment, and the precision of the test rig and equipment utilized. For future projects, it is advisable to conduct an in-depth design process aimed at creating a test rig and test conditions that offers higher precision than the one achieved in this project.

Bibliography

- [1] J. Deubner, P. Coulon, and I. Diester, “Optogenetic approaches to study the mammalian brain,” *Curr. Opin. Struct. Biol.*, vol. 57, pp. 157–163, 2019.
- [2] M. Schormans, V. Valente, and A. Demosthenous, “Practical inductive link design for biomedical wireless power transfer: A tutorial,” *IEEE Trans. Biomed. Circuits Syst.*, vol. 12, no. 5, pp. 1112–1130, 2018.
- [3] S. A. Mirbozorgi, P. Yeon, and M. Ghovanloo, “Robust wireless power transmission to mm-sized free-floating distributed implants,” *IEEE Transactions on Biomedical Circuits and Systems*, vol. 11, no. 3, pp. 692–702, 2017.
- [4] R. Wu, W. Li, H. Luo, J. K. O. Sin, and C. P. Yue, “Design and characterization of wireless power links for brain–machine interface applications,” *IEEE Transactions on Power Electronics*, vol. 29, no. 10, pp. 5462–5471, 2014.
- [5] A. Basir, I. A. Shah, and H. Yoo, “Sphere-shaped receiver coil for misalignment-resilient wireless power transfer systems for implantable devices,” *IEEE Transactions on Antennas and Propagation*, vol. 70, no. 9, pp. 8368–8378, 2022.
- [6] U.-M. Jow, P. McMenamin, M. Kiani, J. R. Manns, and M. Ghovanloo, “EnerCage: A smart experimental arena with scalable architecture for behavioral experiments,” *IEEE Trans. Biomed. Eng.*, vol. 61, no. 1, pp. 139–148, 2014.
- [7] L. Goje, “An overview of wireless power transmission (wpt),” 04 2021.
- [8] Efficient Power Conversion (EPC), “Development board epc9058 quick start guide,” Data sheet, Efficient Power Conversion (EPC), 2023. [Online]. Available: <https://epc-co.com/epc/products/demo-boards/epc9058>
- [9] S. Keyrouz, H. Pflug, and H. Visser, “Input impedance calculation of a multi-stage rectifier circuit,” in *2019 IEEE Wireless Power Transfer Conference (WPTC)*, 2019, pp. 30–35.
- [10] “Demonstration system EPC9510 quick start guide,” https://epc-co.com/epc/Portals/0/epc/documents/guides/EPC9510_qsg.pdf, accessed: 2023-10-27.
- [11] A. Bansal, F. Yang, T. Xi, Y. Zhang, and J. S. Ho, “In vivo wireless photonic photodynamic therapy,” *Proc. Natl. Acad. Sci. U. S. A.*, vol. 115, no. 7, pp. 1469–1474, 2018.
- [12] S. M. Won, E. Song, J. T. Reeder, and J. A. Rogers, “Emerging modalities and implantable technologies for neuromodulation,” *Cell*, vol. 181, no. 1, pp. 115–135, 2020. [Online]. Available: <https://www.sciencedirect.com/science/article/pii/S0092867420302312>

- [13] E. Boyden, “A history of optogenetics: The development of tools for controlling brain circuits with light,” *F1000 biology reports*, vol. 3, p. 11, 05 2011.
- [14] K. Deisseroth, “Optogenetics: 10 years of microbial opsins in neuroscience,” *Nature Neuroscience*, vol. 18, pp. 1213–1225, 2015. [Online]. Available: <https://api.semanticscholar.org/CorpusID:5678727>
- [15] C. A. Azevedo and A. Mammis, “Neuromodulation therapies for alcohol addiction: A literature review,” *Neuromodulation*, vol. 21, no. 2, pp. 144–148, 2018.
- [16] J. Fang and C. Tolleson, “The role of deep brain stimulation in parkinson’s disease: an overview and update on new developments,” *Neuropsychiatr Dis Treat*, vol. 13, pp. 723–732, 2017.
- [17] S. Mishra, “Electroceuticals in medicine - the brave new future,” *Indian Heart J.*, vol. 69, no. 5, pp. 685–686, 2017.
- [18] S. H. Yun and S. J. J. Kwok, “Light in diagnosis, therapy and surgery,” *Nat. Biomed. Eng.*, vol. 1, no. 1, 2017.
- [19] F. Pisanello, G. Mandelbaum, M. Pisanello, I. A. Oldenburg, L. Sileo, J. E. Markowitz, R. E. Peterson, A. Della Patria, T. M. Haynes, M. S. Emara, B. Spagnolo, S. R. Datta, M. De Vittorio, and B. L. Sabatini, “Dynamic illumination of spatially restricted or large brain volumes via a single tapered optical fiber,” *Nat. Neurosci.*, vol. 20, no. 8, pp. 1180–1188, 2017.
- [20] A. Canales, X. Jia, U. P. Froriep, R. A. Koppes, “Multifunctional fibers for simultaneous optical, electrical and chemical interrogation of neural circuits in vivo,” Oct. 2015, accessed: 2023-10-14.
- [21] Ofer Yizhar,¹ Lief E. Fenn,¹ Thomas J. Davidson,¹ Murtaza Mogri,¹ and Karl Deisseroth, “Optogenetics in neural systems,” [https://www.cell.com/neuron/pdf/S0896-6273\(11\)00504-6.pdf](https://www.cell.com/neuron/pdf/S0896-6273(11)00504-6.pdf), accessed: 2023-10-14.
- [22] A. M. Aravanis, L.-P. Wang, F. Zhang, L. A. Meltzer, M. Z. Mogri, M. B. Schneider, and K. Deisseroth, “An optical neural interface:*in vivo*control of rodent motor cortex with integrated fiberoptic and optogenetic technology,” *J. Neural Eng.*, vol. 4, no. 3, pp. S143–S156, 2007.
- [23] H. Tian, K. Xu, L. Zou, and Y. Fang, “Multimodal neural probes for combined optogenetics and electrophysiology,” *iScience*, vol. 25, no. 1, p. 103612, 2022.
- [24] P. Fan, Y. Song, S. Xu, Y. Dai, Y. Wang, B. Lu, J. Xie, H. Wang, and X. Cai, “In vivo optogenetic modulation with simultaneous neural detection using microelectrode array integrated with optical fiber,” *Sensors (Basel)*, vol. 20, no. 16, p. 4526, 2020.
- [25] A. N. Zorzos, J. Scholvin, E. S. Boyden, and C. G. Fonstad, “Three-dimensional multiwaveguide probe array for light delivery to distributed brain circuits,” *Opt. Lett.*, vol. 37, no. 23, p. 4841, 2012.
- [26] K. Y. Kwon, A. G. Gnade, A. D. Rush, and C. D. Patten, “Head-mounted LED for optogenetic experiments of freely-behaving animal,” in *Clinical and Translational Neurophotonics; Neural*

- Imaging and Sensing; and Optogenetics and Optical Manipulation*, S. J. Madsen, V. X. D. Yang, E. D. Jansen, Q. Luo, S. K. Mohanty, and N. V. Thakor, Eds., vol. 9690. SPIE, 2016, p. 96902O.
- [27] J. Hee Lee, S. Lee, D. Kim, and K. Jae Lee, “Implantable Micro-Light-Emitting diode (μ LED)-based optogenetic interfaces toward human applications,” *Adv. Drug Deliv. Rev.*, vol. 187, no. 114399, p. 114399, 2022.
- [28] R.-F. Xue, K.-W. Cheng, and M. Je, “High-efficiency wireless power transfer for biomedical implants by optimal resonant load transformation,” *IEEE Transactions on Circuits and Systems I: Regular Papers*, vol. 60, no. 4, pp. 867–874, 2013.
- [29] S. M. Won, L. Cai, P. Gutruf, and J. A. Rogers, “Wireless and battery-free technologies for neuroengineering,” *Nat. Biomed. Eng.*, vol. 7, no. 4, pp. 405–423, 2021.
- [30] L. Lu, P. Gutruf, L. Xia, D. L. Bhatti, X. Wang, A. Vazquez-Guardado, X. Ning, X. Shen, T. Sang, R. Ma, G. Pakeltis, G. Sobczak, H. Zhang, D.-O. Seo, M. Xue, L. Yin, D. Chanda, X. Sheng, M. R. Bruchas, and J. A. Rogers, “Wireless optoelectronic photometers for monitoring neuronal dynamics in the deep brain,” *Proc. Natl. Acad. Sci. U. S. A.*, vol. 115, no. 7, 2018.
- [31] D. Sharma, S. Kumar, N. Singh, B. K. Kanaujia, S. P. Singh, and A. Lay-Ekuakille, “Far-field wireless power transmission and measurement for a leadless transcatheter pacing system,” *IEEE Transactions on Instrumentation and Measurement*, vol. 72, pp. 1–12, 2023.
- [32] S. I. Park, D. S. Brenner, G. Shin, C. D. Morgan, B. A. Copits, H. U. Chung, M. Y. Pullen, K. N. Noh, S. Davidson, S. J. Oh, J. Yoon, K.-I. Jang, V. K. Samineni, M. Norman, J. G. Grajales-Reyes, S. K. Vogt, S. S. Sundaram, K. M. Wilson, J. S. Ha, R. Xu, T. Pan, T.-I. Kim, Y. Huang, M. C. Montana, J. P. Golden, M. R. Bruchas, R. W. Gereau, IV, and J. A. Rogers, “Soft, stretchable, fully implantable miniaturized optoelectronic systems for wireless optogenetics,” *Nat. Biotechnol.*, vol. 33, no. 12, pp. 1280–1286, 2015.
- [33] J. G. McCall, T.-I. Kim, G. Shin, X. Huang, Y. H. Jung, R. Al-Hasani, F. G. Omenetto, M. R. Bruchas, and J. A. Rogers, “Fabrication and application of flexible, multimodal light-emitting devices for wireless optogenetics,” *Nat. Protoc.*, vol. 8, no. 12, pp. 2413–2428, 2013.
- [34] T.-I. Kim, J. G. McCall, Y. H. Jung, X. Huang, E. R. Siuda, Y. Li, J. Song, Y. M. Song, H. A. Pao, R.-H. Kim, C. Lu, S. D. Lee, I.-S. Song, G. Shin, R. Al-Hasani, S. Kim, M. P. Tan, Y. Huang, F. G. Omenetto, J. A. Rogers, and M. R. Bruchas, “Injectable, cellular-scale optoelectronics with applications for wireless optogenetics,” *Science*, vol. 340, no. 6129, pp. 211–216, 2013.
- [35] S. I. Park, G. Shin, J. G. McCall, R. Al-Hasani, A. Norris, L. Xia, D. S. Brenner, K. N. Noh, S. Y. Bang, D. L. Bhatti, K.-I. Jang, S.-K. Kang, A. D. Mickle, G. Dussor, T. J. Price, R. W. Gereau, IV, M. R. Bruchas, and J. A. Rogers, “Stretchable multichannel antennas in soft wireless optoelectronic implants for optogenetics,” *Proc. Natl. Acad. Sci. U. S. A.*, vol. 113, no. 50, 2016.
- [36] S. A. A. Shah, A. Basir, Y.-H. Lim, and H. Yoo, “A novel efficient wirelessly powered biotelemetric endovascular aortic stent antenna system,” *IEEE Transactions on Antennas and Propagation*, vol. 71, no. 9, pp. 7132–7145, 2023.

- [37] D. K. Biswas, M. Sinclair, J. Hyde, and I. Mahbub, “An nfc (near-field communication) based wireless power transfer system design with miniaturized receiver coil for optogenetic implants,” in *2018 Texas Symposium on Wireless and Microwave Circuits and Systems (WMCS)*, 2018, pp. 1–5.
- [38] M. Zargham and P. G. Gulak, “Maximum achievable efficiency in near-field coupled power-transfer systems,” *IEEE Transactions on Biomedical Circuits and Systems*, vol. 6, no. 3, pp. 228–245, 2012.
- [39] C.-L. Yang, C.-K. Chang, S.-Y. Lee, S.-J. Chang, and L.-Y. Chiou, “Efficient four-coil wireless power transfer for deep brain stimulation,” *IEEE Transactions on Microwave Theory and Techniques*, vol. 65, no. 7, pp. 2496–2507, 2017.
- [40] C.-K. Chang and C.-L. Yang, “Inductive 3-coil wireless power transfer improved by t-type impedance matching for implanted biomedical ic,” in *2015 IEEE Wireless Power Transfer Conference (WPTC)*, 2015, pp. 1–4.
- [41] A. P. Sample, D. T. Meyer, and J. R. Smith, “Analysis, experimental results, and range adaptation of magnetically coupled resonators for wireless power transfer,” *IEEE Transactions on Industrial Electronics*, vol. 58, no. 2, pp. 544–554, 2011.
- [42] U.-M. Jow and M. Ghovanloo, “Modeling and optimization of printed spiral coils in air, saline, and muscle tissue environments,” *IEEE Transactions on Biomedical Circuits and Systems*, vol. 3, no. 5, pp. 339–347, 2009.
- [43] ———, “Design and optimization of printed spiral coils for efficient transcutaneous inductive power transmission,” *IEEE Transactions on Biomedical Circuits and Systems*, vol. 1, no. 3, pp. 193–202, 2007.
- [44] T. Delhaye, N. André, S. Gilet, C. Gimeno, L. A. Francis, and D. Flandre, “High-efficiency wireless power transfer for mm-size biomedical implants,” 10 2017, pp. 1–3.
- [45] B. H. Waters, B. J. Mahoney, G. Lee, and J. R. Smith, “Optimal coil size ratios for wireless power transfer applications,” in *2014 IEEE International Symposium on Circuits and Systems (ISCAS)*, 2014, pp. 2045–2048.
- [46] M. Kiani and M. Ghovanloo, “An rfid-based closed-loop wireless power transmission system for biomedical applications,” *IEEE Transactions on Circuits and Systems II: Express Briefs*, vol. 57, no. 4, pp. 260–264, 2010.
- [47] Q. Xu, H. Wang, Z. Gao, Z.-H. Mao, J. He, and M. Sun, “A novel mat-based system for position-varying wireless power transfer to biomedical implants,” *IEEE Transactions on Magnetics*, vol. 49, no. 8, pp. 4774–4779, 2013.
- [48] W. Tricity, “Highly resonant wireless power transfer;,” <http://large.stanford.edu/courses/2016/ph240/surakitbovorn1/docs/kesler.pdf>, accessed: 2023-10-24.
- [49] S. A. Mirbozorgi, H. Bahrami, M. Sawan, and B. Gosselin, “A smart multi-receiver power transmission system for long-term biological monitoring,” in *2014 IEEE Biomedical Circuits and Systems Conference (BioCAS) Proceedings*, 2014, pp. 412–415.

- [50] S. R. Khan, S. K. Pavuluri, G. Cummins, and M. P. Y. Desmulliez, “Miniaturized 3-d cross-type receiver for wirelessly powered capsule endoscopy,” *IEEE Transactions on Microwave Theory and Techniques*, vol. 67, no. 5, pp. 1985–1993, 2019.
- [51] Z. Zhang and B. Zhang, “Angular-misalignment insensitive omnidirectional wireless power transfer,” *IEEE Transactions on Industrial Electronics*, vol. 67, no. 4, pp. 2755–2764, 2020.
- [52] O. Jonah, S. V. Georgakopoulos, and M. M. Tentzeris, “Orientation insensitive power transfer by magnetic resonance for mobile devices,” in *2013 IEEE Wireless Power Transfer (WPT)*, 2013, pp. 5–8.
- [53] Y. Palagani, K. Mohanarangam, J. H. Shim, and J. R. Choi, “Wireless power transfer analysis of circular and spherical coils under misalignment conditions for biomedical implants,” *Biosens. Bioelectron.*, vol. 141, no. 111283, p. 111283, 2019.
- [54] P. Si, A. P. Hu, S. Malpas, and D. Budgett, “A frequency control method for regulating wireless power to implantable devices,” *IEEE Transactions on Biomedical Circuits and Systems*, vol. 2, no. 1, pp. 22–29, 2008.
- [55] K. L. Montgomery, A. J. Yeh, J. S. Ho, V. Tsao, S. Mohan Iyer, L. Grosenick, E. A. Ferenczi, Y. Tanabe, K. Deisseroth, S. L. Delp, and A. S. Y. Poon, “Wirelessly powered, fully internal optogenetics for brain, spinal and peripheral circuits in mice,” *Nat. Methods*, vol. 12, no. 10, pp. 969–974, 2015.
- [56] W. Ouyang, W. Lu, Y. Zhang, Y. Liu, J. U. Kim, H. Shen, Y. Wu, H. Luan, K. Kilner, S. P. Lee, Y. Lu, Y. Yang, J. Wang, Y. Yu, A. J. Wegener, J. A. Moreno, Z. Xie, Y. Wu, S. M. Won, K. Kwon, C. Wu, W. Bai, H. Guo, T.-L. Liu, H. Bai, G. Monti, J. Zhu, S. R. Madhvapathy, J. Trueb, M. Stanslaski, E. M. Higbee-Dempsey, I. Stepien, N. Ghoreishi-Haack, C. R. Haney, T.-I. Kim, Y. Huang, R. Ghaffari, A. R. Banks, T. C. Jhou, C. H. Good, and J. A. Rogers, “A wireless and battery-less implant for multimodal closed-loop neuromodulation in small animals,” *Nat. Biomed. Eng.*, pp. 1–18, 2023.
- [57] T. Sekitani and T. Someya, “Stretchable, large-area organic electronics,” *Adv. Mater.*, vol. 22, no. 20, pp. 2228–2246, 2010.
- [58] D.-H. Kim, J. Xiao, J. Song, Y. Huang, and J. A. Rogers, “Stretchable, curvilinear electronics based on inorganic materials,” *Adv. Mater.*, vol. 22, no. 19, pp. 2108–2124, 2010.
- [59] M. Kaltenbrunner, T. Sekitani, J. Reeder, T. Yokota, K. Kuribara, T. Tokuhara, M. Drack, R. Schwödiauer, I. Graz, S. Bauer-Gogonea, S. Bauer, and T. Someya, “An ultra-lightweight design for imperceptible plastic electronics,” *Nature*, vol. 499, no. 7459, pp. 458–463, 2013.
- [60] Y. Zhang, H. Fu, Y. Su, S. Xu, H. Cheng, J. A. Fan, K.-C. Hwang, J. A. Rogers, and Y. Huang, “Mechanics of ultra-stretchable self-similar serpentine interconnects,” *Acta Mater.*, vol. 61, no. 20, pp. 7816–7827, 2013.
- [61] C. Hassler, T. Boretius, and T. Stieglitz, “Polymers for neural implants: Polymers for neural implants,” *J. Polym. Sci. B Polym. Phys.*, vol. 49, no. 1, pp. 18–33, 2011.

- [62] G. Shin, A. M. Gomez, R. Al-Hasani, Y. R. Jeong, J. Kim, Z. Xie, A. Banks, S. M. Lee, S. Y. Han, C. J. Yoo, J.-L. Lee, S. H. Lee, J. Kurniawan, J. Tureb, Z. Guo, J. Yoon, S.-I. Park, S. Y. Bang, Y. Nam, M. C. Walicki, V. K. Samineni, A. D. Mickle, K. Lee, S. Y. Heo, J. G. McCall, T. Pan, L. Wang, X. Feng, T.-I. Kim, J. K. Kim, Y. Li, Y. Huang, R. W. Gereau, IV, J. S. Ha, M. R. Bruchas, and J. A. Rogers, “Flexible near-field wireless optoelectronics as subdermal implants for broad applications in optogenetics,” *Neuron*, vol. 93, no. 3, pp. 509–521.e3, 2017.
- [63] J. Zhang, D. Hoare, R. Das, M. Holsgrave, J. Czyzewski, N. Mirzai, J. Mercer, and H. Heidari, “Wireless impedance platform for autonomous vascular implantable devices,” in *2022 29th IEEE International Conference on Electronics, Circuits and Systems (ICECS)*, 2022, pp. 1–4.
- [64] F. Nassirinia, W. Straver, F. E. Hoebeek, and W. A. Serdijn, “Wireless power transfer and optogenetic stimulation of freely moving rodents,” in *2017 8th International IEEE/EMBS Conference on Neural Engineering (NER)*, 2017, pp. 456–460.
- [65] H. Gougheri and M. Kiani, “Optimal frequency for powering Millimeter-Sized biomedical implants inside an Inductively-Powered homecage,” <https://ieeexplore.ieee.org/stamp/stamp.jsp?arnumber=7591802>, accessed: 2023-10-25.
- [66] Z. Zhang, H. Pang, A. Georgiadis, and C. Cecati, “Wireless power transfer—an overview,” *IEEE Transactions on Industrial Electronics*, vol. 66, no. 2, pp. 1044–1058, 2019.
- [67] W. Zhang and C. Mi, “Compensation topologies of High-Power wireless power transfer systems,” https://www.researchgate.net/publication/282499385_Compensation_Topologies_of_High-Power_Wireless_Power_Transfer_Systems, Jan. 2015, accessed: 2023-10-15.
- [68] S. Jayalath, Member, A. Khan, and Senior Member, “Design, challenges, and trends of inductive power transfer couplers for electric vehicles: A review,” <https://sampathjayalath.com/wp-content/uploads/2022/12/FINAL-VERSION.pdf>, accessed: 2023-10-15.
- [69] K. N. Mude and K. Aditya, “Comprehensive review and analysis of two-element resonant compensation topologies for wireless inductive power transfer systems,” <https://ieeexplore.ieee.org/stamp/stamp.jsp?arnumber=8794849>, Jun. 2019, accessed: 2023-10-15.
- [70] H. Kim, C. Song, D.-H. Kim, D. H. Jung, I.-M. Kim, Y.-I. Kim, J. Kim, S. Ahn, and J. Kim, “Coil design and measurements of automotive magnetic resonant wireless charging system for high-efficiency and low magnetic field leakage,” *IEEE Transactions on Microwave Theory and Techniques*, vol. 64, no. 2, pp. 383–400, 2016.
- [71] S. Muhammad, J.-J. Tiang, S.-K. Wong, and A. H. Rambe, “Harvesting systems for RF energy: Trends, challenges, techniques, and tradeoffs,” https://www.researchgate.net/publication/359355440_Harvesting_Systems_for_RF_Energy_Trends_Challenges_Techniques_and_Tradeoffs, Mar. 2022, accessed: 2023-10-26.
- [72] A. Basir and H. Yoo, “Efficient wireless power transfer system with a miniaturized quad-band implantable antenna for deep-body multitasking implants,” *IEEE Transactions on Microwave Theory and Techniques*, vol. 68, no. 5, pp. 1943–1953, 2020.

- [73] P. In, "Guidelines for limiting exposure to electromagnetic fields (100 khz to 300 GHz)," *Health Phys.*, vol. 118, no. 5, pp. 483–524, 2020.
- [74] H. Lu, L. C. W. Lam, and Y. Ning, "Scalp-to-cortex distance of left primary motor cortex and its computational head model: Implications for personalized neuromodulation," *CNS Neurosci. Ther.*, vol. 25, no. 11, pp. 1270–1276, 2019.
- [75] "Pcb manufacturing & assembly capabilities," JLCPCB, no date. [Online]. Available: <https://jlcpcb.com/capabilities/pcb-assembly-capabilities>
- [76] "Pcb manufacturing & assembly capabilities," JLCPCB, no date. [Online]. Available: <https://jlcpcb.com/capabilities/pcb-capabilities>
- [77] "Pcb prototype & pcb fabrication manufacturer," JLCPCB, no date. [Online]. Available: <https://cart.jlcpcb.com/quote/>
- [78] <https://epc-co.com/epc/products/demo-boards/epc9083>, accessed: 2023-10-19.

Appendix A

Appendix

A.1 ICNIRP Documentation

Table 8. Reference levels for local exposure to electromagnetic fields from 100 kHz to 10 MHz (unperturbed rms values), for peak values.^a

Exposure scenario	Frequency range	Incident E-field strength; E_{inc} (V m ⁻¹)	Incident H-field strength; H_{inc} (A m ⁻¹)
Occupational	100 kHz – 10 MHz	170	80
General public	100 kHz – 10 MHz	83	21

^aNote:

1. Regardless of the far-field/near-field zone distinction, compliance is demonstrated if neither peak spatial E_{inc} or peak spatial H_{inc} , over the projected whole-body space, exceeds the above reference level values.

Figure A.1: Figure depicting ICNIRP magnetic field strength regulations

Table 2. Basic restrictions for electromagnetic field exposure from 100 kHz to 300 GHz, for averaging intervals ≥ 6 min.^a

Exposure scenario	Frequency range	Whole-body average SAR (W kg ⁻¹)	Local Head/Torso SAR (W kg ⁻¹)	Local Limb SAR (W kg ⁻¹)	Local S_{ab} (W m ⁻²)
Occupational	100 kHz to 6 GHz	0.4	10	20	NA
	>6 to 300 GHz	0.4	NA	NA	100
General public	100 kHz to 6 GHz	0.08	2	4	NA
	>6 to 300 GHz	0.08	NA	NA	20

^aNote:

1. "NA" signifies "not applicable" and does not need to be taken into account when determining compliance.
2. Whole-body average SAR is to be averaged over 30 min.
3. Local SAR and S_{ab} exposures are to be averaged over 6 min.
4. Local SAR is to be averaged over a 10-g cubic mass.
5. Local S_{ab} is to be averaged over a square 4-cm² surface area of the body. Above 30 GHz, an additional constraint is imposed, such that exposure averaged over a square 1-cm² surface area of the body is restricted to two times that of the 4-cm² restriction.

Figure A.2: Figure depicting ICNIRP SAR regulations

A.2 Benchmark Simulation

The following images offer a comparison of the commercial [RFID](#) transmitter used by Bansal et al. [11] and the transmitter modelled in [FEA](#) simulation.

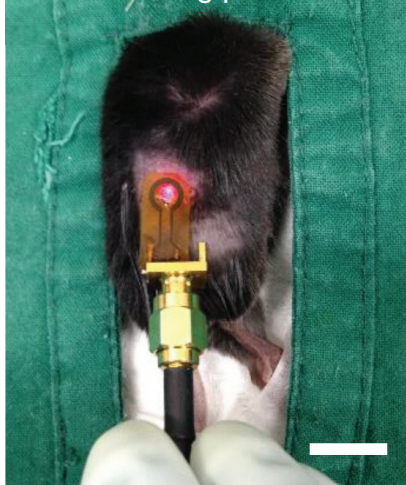


Figure A.3: Figure depicting the commercial [RFID](#) transmitter used in [11]

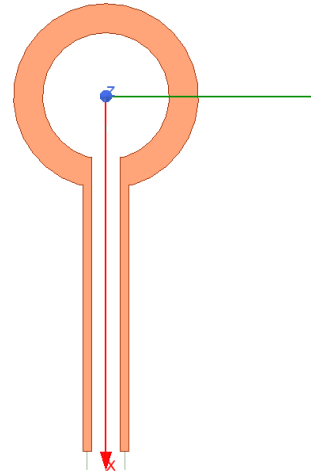


Figure A.4: Figure depicting the comparative [RFID](#) transmitter modelled in simulation

Figure A.5 gives insight into the magnetic field vectors generated by the benchmark coil system. As noted, the rotation of the receiver serves to enable the capture of both perpendicular and parallel flux.

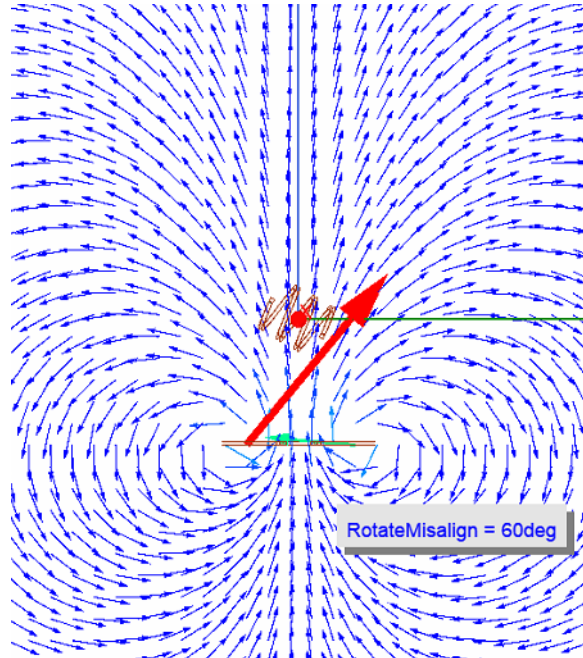


Figure A.5: Figure depicting the simulated magnetic field vectors for the 3mm benchmarking setup

A.3 Iterative Designs: Additional Simulation Results

The following sections provide the additional results obtained during simulation.

A.3.1 Design Iteration 1

Figure A.6 depicts the simulated model of design [1].

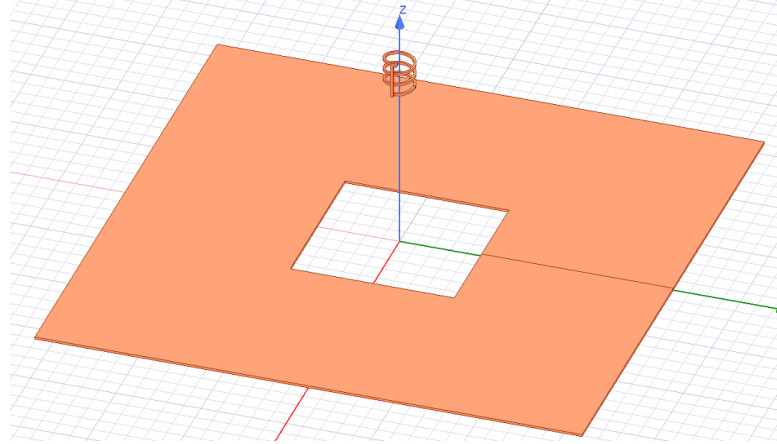


Figure A.6: Figure depicting an isometric view of the simulated setup with a wire-wound transmitter. Note that, although the transmitter in Figure A.6 may appear as a solid structure, the simulation was configured to mimic the behavior of wire-wound coil excitation rather than a solid sheet of copper.

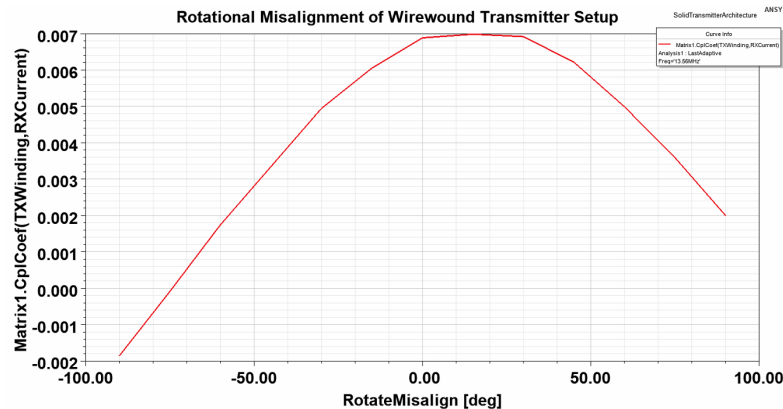


Figure A.7: Results obtained during the rotational misalignment sweep with a wire-wound transmitter



Figure A.8: Results obtained during the lateral misalignment test with a wire-wound transmitter

A.3.2 Design Iteration 2

The following figures depict the simulated model of design [2].

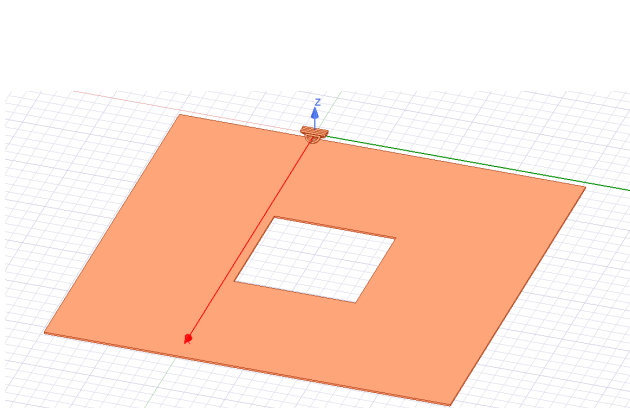


Figure A.9: Figure depicting simulated setup for the double helix coil

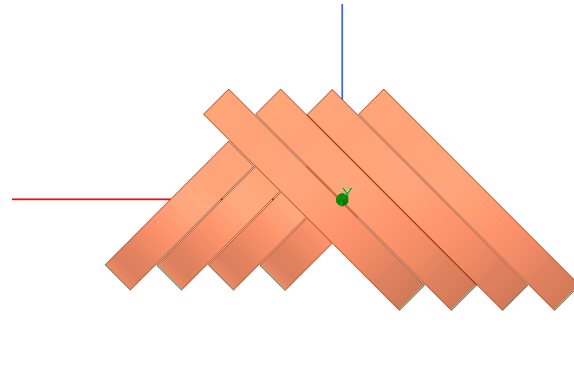


Figure A.10: Figure depicting a side view of the double helix coil

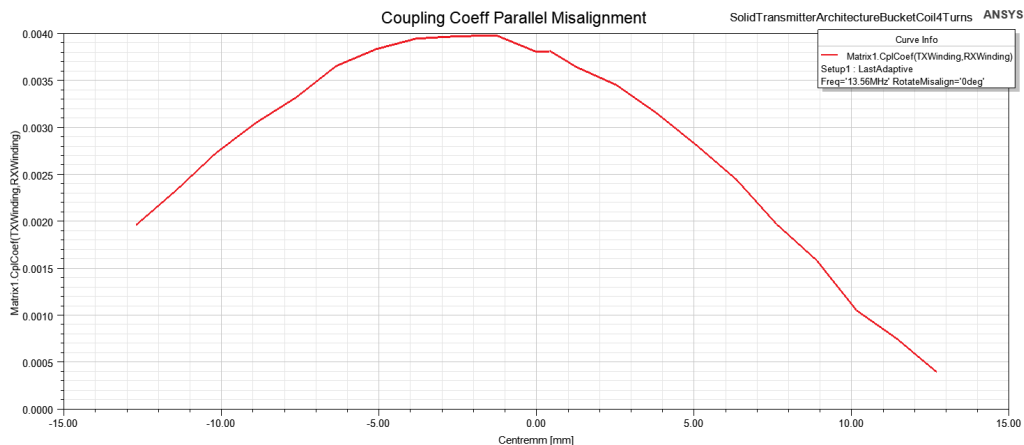


Figure A.11: Figure depicting the response of the double helix setup to parallel misalignments

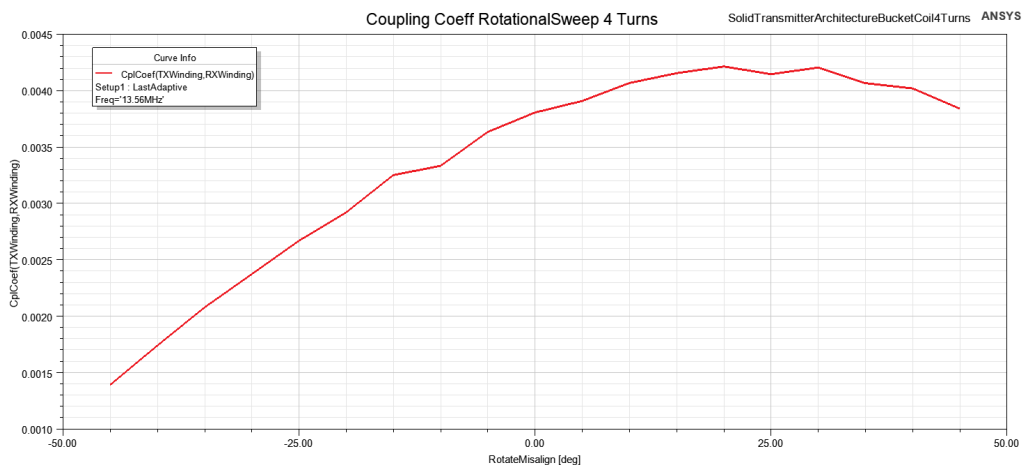


Figure A.12: Figure depicting the response of the double helix setup to rotational misalignments

A.3.3 Design Iteration 3

Figure A.13 depicts the simulated model of design [3].

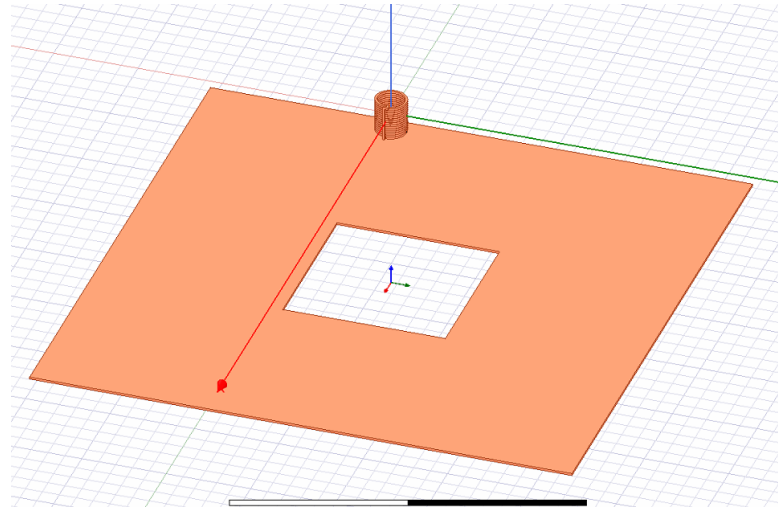


Figure A.13: Figure depicting an isometric view of the 15-turn solenoid setup

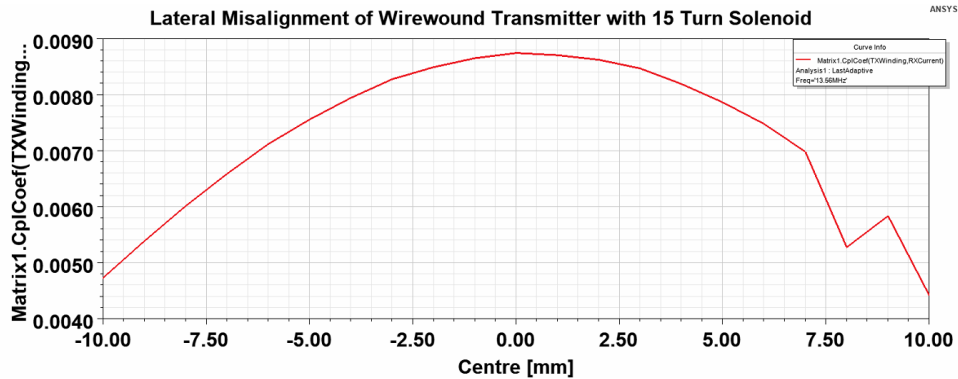


Figure A.14: Figure depicting the results of the 15-turn lateral misalignment sweep

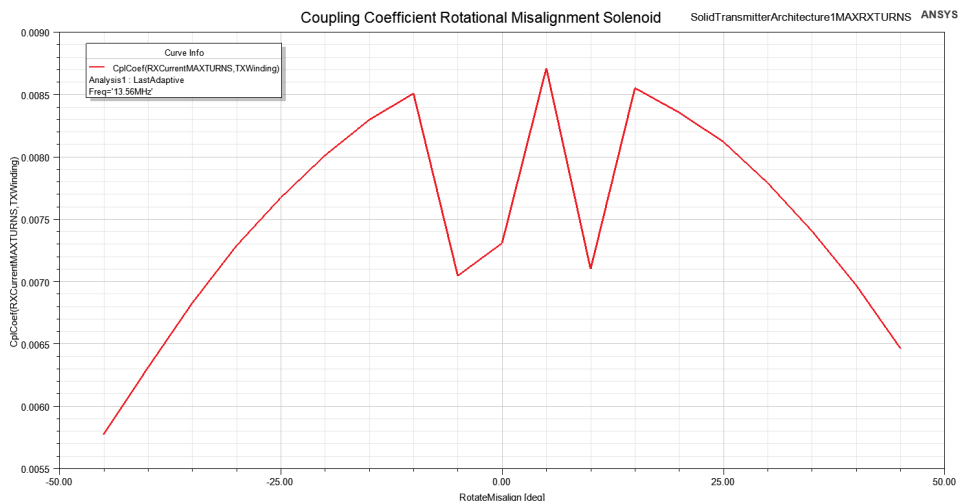


Figure A.15: Figure depicting the results of the 15-turn rotational misalignment sweep

A.4 Physical System Implementation



(a) Figure depicting transmitter jig base with angled point of entry and point of exit



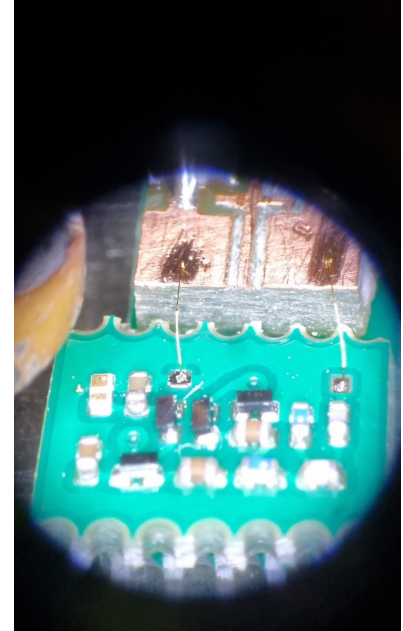
(b) Figure depicting wound transmitter coil in jig



(a) Figure depicting microscope setup used for hand soldering



(b) Figure depicting MP4522 Ball Bonding Machine



(c) Figure depicting ball bonds made to connect the [PCB](#) to receiver coil adapter

A.5 Practical Coil Coupling Results

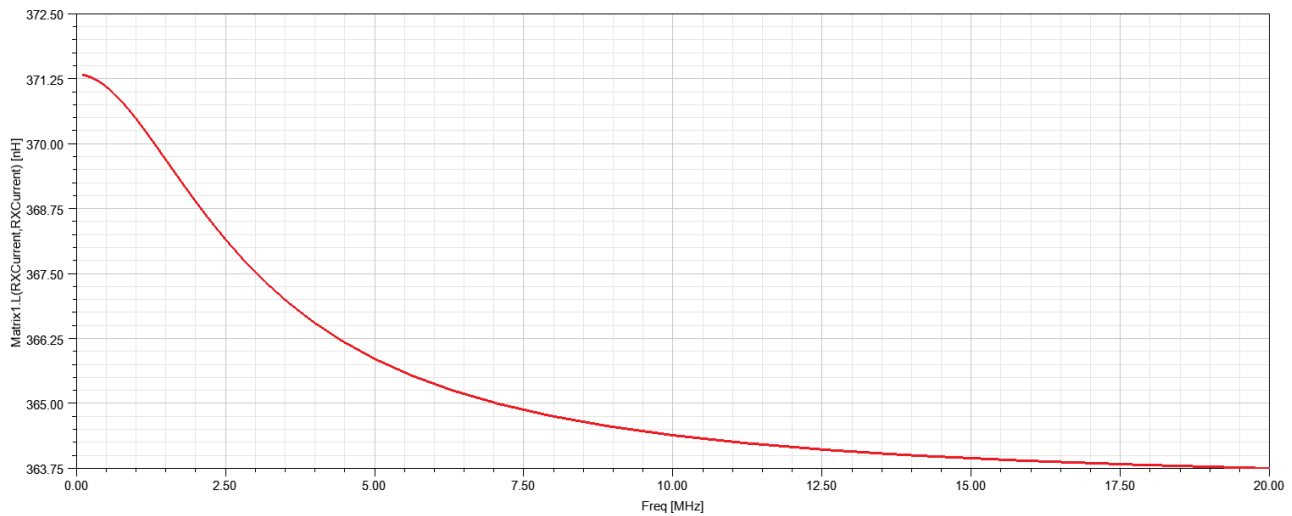


Figure A.18: Figure depicting the simulated receiver coil inductance vs frequency